UNIVERSITÀ DEGLI STUDI DI TRENTO

Andrea Pedrielli

Modeling and simulations of low dimensional and nanostructured systems at the nanoscale

2017 - Doctoral thesis

The properties of a broad range of materials are due to processes which occur at the nanoscale. Recently, an increasing interest was devoted to nanostructured materials, in which the basic components are nanoscopic, and low-dimensional nanomaterials such as nanoparticles, nanowires and layered materials, in which one or more dimensions are confined. This thesis deals with nanostructured materials, in particular based on graphene, such as Graphene Nanofoams and Pillared Graphene Frameworks, and low dimensional nanomaterials such as SiC/SiO_2 core/shell nanowires and graphene layers. The work is divided in four parts treating four different topics with the underlying theme of material modeling, the first two parts deal with mechanical properties and gas treatment applications, for which a description at the atomistic level is adequate, while the third and the forth focus on X-ray spectra and electron holography simulations for which electronic structure calculations are needed. The present thesis gives a general overview on various computational approaches that are useful in modeling novel low dimensional and nanostructured materials, using these approaches in dealing with specific systems.

Andrea Pedrielli He holds the Master's degree in Physics of Matter obtained at the University of Bologna. During the Master's thesis he focused on transfer ad characterization and technological integration of graphene. Then he moved to the University of Trento to complete his scientific formation with a PhD in Civil, Environmental and Mechanical Engineering in collaboration with Fondazione Bruno Kessler and European Center for Theoretical Physics and Related Areas. He carried on research activity form the computational side, focusing on mechanical and electronic properties of nanoscopic and nanostructured materials. The main outcomes of his research activity are represented by the study of novel graphene-based metamaterial and the development of realistic models graphene nanofoams. The current research activity is focused on mechanical and gas adsorption properties of porous materials and X-ray mediated cancer therapy.

Andrea Pedrielli

Modeling and simulations of low dimensional and nanostructured systems at the nanoscale

Supervisors
Nicola M. Pugno - University of Trento
Giovanni Garberoglio - FBK-ECT*

Contents

i

Abstract

The properties of a broad range of materials are due to processes which occur at the nanoscale. Recently, an increasing interest was devoted to nanostructured materials, in which the basic components are nanoscopic, and low-dimensional nanomaterials such as nanoparticles, nanowires and layered materials, in which one or more dimensions are confined. This work deals with nanostructured materials, in particular based on graphene, such as Graphene Nanofoams and Pillared Graphene Frameworks, and low dimensional nanomaterials such as SiC/SiO_2 core/shell nanowires and graphene layers. The thesis is divided in four parts treating four different topics with the underlying theme of material modeling, the first two parts deal with mechanical properties and gas treatment applications, for which a description at the atomistic level is adequate, while the third and the forth focus on X-ray spectra and electron holography simulations for which electronic structure calculations are needed.

In the first part we present the modeling of graphene nanofoams, in two different versions, regular and random, assessing their thermal and mechanical properties. A full atomistic approach is used, by means of Molecular Dynamics with Bond Order Reactive Potential. Regular nanofoams studied here are based on Face Centered Cubic geometry and built up tiling with graphene an octet-truss surface with spherical nodes. The effect of various geometrical parameters, namely strut and nodal diameter was explored. The mechanical properties of regular foams turn out to be almost isotropic under tension, presenting instead a strongly directional dependence under compression. In this last case peculiar elastic instabilities were found for specific loading directions. Regarding random nanofoams, a similar study is performed, investigating the mechanics of the deformation under

tension and compression. This kind of nanofoams are intrinsically less performant than regular ones at mechanical level due to the presence of regions that are not able to carry loads and hence are essentially elastically ineffective. However, under compression the elastically ineffective parts result to play a role due to their volume occupation.

The second part focus on the study of gas adsorption and dynamics in Pillared Graphene Frameworks, performed by means of Grand Canonical Monte Carlo method and Molecular Dynamics. These kind of structures are composed by graphene layers intercalated by organic moieties that act as spacers. The high surface-to-volume ratio of graphene layers can be exploited by tuning dimension of the spacers. This part of the thesis explores the influence on gas adsorption and dynamics of the pillar density and type for a narrow class of nitrogen-containing Pillared Graphene Frameworks. The gases tested for adsorption are CH_4, CO_2, H_2, N_2 and O_2, and separation is assessed for some mixture thereof. The results show an higher influence of the pillar density with respect to the pillar type, and good performances for gas separation, comparable to those of Metal Organic Frameworks. An evaluation of the difference in using two different force fields to describe the gas-frameworks interaction, Universal Force Field or DREIDING, is also presented.

The third part deals with the modeling of realistic SiC/SiO_2 core/shell nanowires and the computation of XANES spectra, aimed at interpreting experimental data on these systems. This kind of structures are promising for cancer treatment and the understanding of the mechanisms that underlie the X-ray absorption are fundamental to optimize their usefulness. Indeed, the coupling of SiC/SiO_2 core/shell nanowires and porphyrin enables the production of oxygen singlets that attack the tumoral cells. Oxygen singlets are produced by means of X-ray stimulation of the structure and the subsequent energy transfer from the nanowire to the porphyrin. The modeling these nanowires takes advantage of Molecular Dynamics simulations and Density Functional Tight Binding method. The XANES spectra are computed, using Density Functional Theory, for various target atoms: oxygen, carbon and silicon. The model proposed here is capable of reproduce the main features of the experimental spectra and can be used to develop a complete model of the porphyrin-nanowire system.

The fourth part of the thesis presents the modeling of graphene folded edges and GW calculations performed in the context of simulation of graphene Electron Holography. The interpretation of Electron Holography is not straightforward and only a few studies were done, mainly for bulk materials. The case of 2D materials such as graphene is still largely unexplored. The work presented in this part aims to give a frameworks in which to perform Electron Holography simulations for graphene based structures, from single layer to folded bilayer edges. The framework is that of Density Functional Theory that enables to accurately compute the main contribution on the electrons phase shift experimentally measured, namely the Coulomb potential. A presentation of some GW calculation results, that indicate the small contribution to the electrons phase shift of the terms different from the Coulomb potential, concludes this part.

In conclusion, the present thesis gives a general overview on various computational approaches that are useful in modeling novel low dimensional and nanostructured materials, using these approaches in dealing with specific systems.

Introduction

Nanoscale phenomena play a fundamental role in a broad range of systems, from biological systems to nanoporous materials, as well as low-dimensional systems such as nanoparticles and nanowires. Biological systems show many emergent properties in the complex interplay of their components. Many effects such as quantum confinement emerge at the nanoscale and novel material properties can be designed exploiting the increased surface area provided by nanostructured materials. At the nanoscale, some material properties such as fluorescence, melting point, electrical conductivity, and chemical reactivity become functions of the typical size of the system. Quantum tunneling is another example of nanoscale effect that emerges when nanosystems are considered. The reactivity of nanosystems is strongly enchanced by the large surface area with respect to the volume and the mass. The large surface area and the enhanced reactivity can be exploited in the development of fuel cells, batteries and catalysts.

The ever-increasing kinds of novel materials based on nanoscopic components that can be designed make challenging to identify the most promising for pratical applications. Expensive experimental setups, the intrinsic difficult in the study of nanoscopic systems and phenomena that happen at short distances and short intervals of time drive a increasing involvement of computational methods in the design of novel materials and in the assessment of their properties. The work reported in this thesis is inserted in this context, in which physical properties of novel material are studied from a computational point of view, in some case de-

signing materials that have not yet been produced at experimental level, in other cases giving insights on specific mechanisms in nanoscopic systems, for which only partial informations can be extracted from experiments.

The present thesis is divided in four parts treating four different topics with the underlying theme of material modeling: the first two topics are at atomic level, while the third and the fourth focus on electronic structure calculations. The four topics are:

- Mechanical and thermal properties of Graphene Nanofoams

- Gas adsorption and dynamics in Pillared Graphene Frameworks

- Modeling and X-ray spectra calculations of SiC/SiO_2 core/shell nanowire

- Modeling of electron holography in folded graphene sheets

Although the study of these stystems is mainly devoted to the investigation of specific properties, a large part of the work reported in this thesis is constituted by the modeling of the systems under investigation, that is a fundamental part of the research work when we deal with complex low dimensional or nanostructured materials.

We briefly describe here the four problems, for their detailed introduction we refer to the chapter 1, 2, 3 and 4, respectively.

In **chapter 1** we present a work on modeling of graphene nanofoams, in two different versions, regular and random, and assess their thermal and mechanical properties. The interest in these kinds of structures is driven by two main factors, on one hand by the growing possiblity of produce high-quality graphene nanofoams at experimental level that makes their potential large-scale application likely to be obtained in the near future, on the other hand the novel properties of these structures push towards the development of a theoretical framework in which they can be rationalized. When experiments are expensive or difficult and the theoretical framework incomplete, a computational approach can be used to get some insights into material properties. Here, we used this computational approach in assessing the mechanical and thermal properties of regular and random graphene nanofoams.

The first part of the chapter deals with regular foams is largely based on a published research paper [Pedrielli et al., 2017a], some details and comments were added with respect to the paper. In assessing the mechanical properties of graphene foams a full atomistic approach is used, by means of Molecular Dynamics with Bond Order Reactive Potential. Regular nanofoams studied here, also named Nanotruss Networks, are based on Face Centered Cubic geometry and built up covering with graphene an octet-truss surface with spherical nodes. The use of this procedure instead of joining primitive components such as fullerenes and nanotubes overcomed the limitations of the previous models found in literature [Wu et al., 2013]. Various geometrical parameters, namely strut and nodal diameter were explored. The mechanical propertiesof these structures turn out to be almost isotropic under tension, presenting instead a strongly directional dependence under compression. In this last case peculiar elastic instabilities were found for specific directions.

Although regular foams, such as those studied in the first part of the chapter, are in general very performant at mechanical level, in some cases, random foams, that are intrinsically less performant, could be anyway suitable for mechanical applications. The literature on this kind of foam is still composed by only a few studies. In the second part of this chapter we give some new insight on random foams investigating the mechanics of the deformation under tension and compression. Furthermore, the thermal conductivity was computed by means of Green-Kubo formalism. This kind of nanofoams are intrinsically less performant than regular ones at mechanical level due to the presence of material that is not able to carry loads and is essentially elastically ineffective. However, under compression also the elastically ineffective parts result to play a role due to their volume occupation.

In **chapter 2** we focus on a study, published as research paper [Pedrielli et al., 2017b], of gas adsorption and dynamics in Pillared Graphene Frameworks, performed by means of Grand Canonical Monte Carlo method and Molecular Dynamics. These structures are composed by graphene layers intercalated by organic molecules that act as spacers allowing to exploit the high surface-to-volume ratio of graphene layers. Furthermore, using different pillar types and pillar densities, gas adsorption and separation can be tuned. This chapter of the thesis explores the influence on gas adsorption and dynamics of the pillar density and type for

a narrow class of nitrogen-containing Pillared Graphene Frameworks. The gases tested for adsorption are CH_4, CO_2, H_2, N_2 and O_2, and separation is assessed for some mixture thereof.

The results show an higher influence of the pillar density with respect to the pillar type, and good performances for gas separation, comparable to those of Metal Organic Frameworks. An evaluation of the difference in using two different force fields to describe the gas-frameworks interaction, Universal Force Field or DREIDING, is also presented.

In **chapter 3** we deal with the modeling of realistic Si/SiO_x core/shell nanowires and the computation of XANES spectra, aimed to comparison with experimental data and their interpretation. This kind of structures are promising for cancer treatment and the understanding of the mechanisms that underlie the X-ray absorption is fundamental to optimize the experimental systems. In Ref. [Tatti et al., 2017] is proposed a method for cancer treatment in which hybrid nanosystems comprised of X-ray absorbing nanostructures (Si/SiO_x core/shell nanowire) and light-sensitive material (porphyrin) are used for the singlet oxygen production. The models presented in this chapter represents the first step toward the modeling and the optimization of this method. The modeling takes advantage of Molecular Dynamics simulations and Densiy Functional Tight Binding method, while XANES spectra are computed for different target atoms: oxygen, carbon and silicon. The model proposed in this chapter, allows to reproduce the main features of the experimental spectra, capturing the main physics of the system under study, and paves the way towards the modeling and the optimization of the full porphyrin-based method for cancer treatment.

In **chapter 4** is presented the modeling of graphene folded edges and GW calculations performed in the context of simulation of graphene Electron Holography. The interpretation of Electron Holography results is not straightforward, indeed informations on the electrostatic potential felt by the electrons impinging on the sample are needed to correctly evaluate the experimental response. Only a few works that investigate the Electron Holography response were performed, mainly for bulk materials. The case of 2D materials such as graphene is still largely unexplored. The work presented in this part aims to give a frameworks in which to perform Electron Holography simulations for graphene-based structures, from single

layer to folded bilayer edges. The framework is that of Density Functional Theory calculations that enables to accurately compute the main contribution on the electrons phase shift experimentally measured, namely the Coulomb potential. We used an hybrid approach in the modeling of graphene folded edges, taking advantage of Molecular Dynamics in the cases in which a full Density Functional Theory treatment was too demanding.

The classical approach in Elecron Holography simulations is the neglecting of non-classical part of the interaction between the electrons and the sample. A more general framework in which the non-classical corrections is included, is that used for Low Energy Electron Diffraction simulations, in which the interaction is treated at GW level, including, in addition to the Coulomb and the exchange and correlation terms coming from Density functional Theory, the self-energy. A presentation of some GW calculation results, that indicate the small contribution to the electrons phase shift of the terms different from the Coulomb potential, concludes this part.

Due to the broad range of computational methods used in the investigation of the systems presented in this thesis, a brief introduction to the topic, computational details, results and discussion sections are inserted in each chapter. Some final remarks conclude the thesis, summarizing the main results presented here.

Chapter 1

Mechanical and Thermal Properties of Graphene Nanofoams

1.1 Introduction to Graphene Regular Foams

Recent advances in single and multi-layered graphene growth techniques [Avouris and Dimitrakopoulos, 2012, Tatti et al., 2016] have renewed the interest in synthesising carbon-based porous nanomaterials. These materials are promising for a broad range of applications, ranging from energy storage in amorphous structures [Alonso, 2012] to tunable hierarchical nanotube scaffolds for regenerative medicine [Coluci and Pugno, 2010], and lightweight foams for oil absorption [Wang et al., 2014].

Furthermore, pristine graphene shows exceptional mechanical properties, such as high ultimate strength and the ability to retain its initial size after strain [Frank et al., 2007]. However, transferring these unique properties to macroscale still represents a challenge for materials scientists. For reliable structural applications it is essential to build macroscopic 3D architectures preserving the intrinsic properties

of the material. This can be achieved through a proper tuning of the porosity and cell geometry which are the parameters that mainly affect the mechanical properties of porous materials [Fleck et al., 2010].

Carbon nanomaterials with random porosity distribution were initially proposed as possible means to transfer graphene's unique mechanical properties, such as Young modulus, tensile strength and toughness from nano- to macroscale. Unfortunately, it turned out that random-pore structures actually exhibit poor scaling of these mechanical properties with decreasing density [Hodge et al., 2005]. Recently, this poor scaling has been investigated for graphene assembly [Qin et al., 2017]. Furthermore, random-pore structures are limited in number of achievable architectures, due to the uncontrollable porous distribution.

At variance, in periodic architectures one can expect all nanoscopic components to work in synergy, and thus deliver optimal mechanical properties at larger length scales. In particular, ordered 3D nano-architectures can be designed to realize specific functional properties such as negative [Baughman and Galvao, 1993, Hall et al., 2008] or flipping Poisson ratio [Wu et al., 2013] or to obtain a significant increase in gas and energy storage [Ding et al., 2007, Tylianakis et al., 2011, Garberoglio et al., 2015, Haberer et al., 2010].

Nevertheless, the realization of these periodic graphene 3D nanostructures has been achieved for only few geometries due to the complexity of the synthesis processes. In this regard, one of the architectures of carbon-based materials that can be most easily manufactured is based on the face-centered cubic (FCC) geometry (Fig. 1.1a). Graphene nanostructures with this geometry have been indeed synthesised, for example, by growing graphene on a FCC assembly of silica nanoparticles [Yoon et al., 2013]. Following this approach, a FCC network of hollow graphene spheres in contact each other was obtained. FCC carbon-based structures can also be realized by covering micrometric 3D trusses with graphene using lithography [Xiao et al., 2012].

On the other hand, computer simulations can be used to perform a detailed screening of different architectures and to help our understanding of their specific properties. To achieve this goal, it is of course necessary to model realistic structures and not only those ideally built from regular blocks of fullerenes and nanotubes.

| (a) FCC unit cell | (b) Octet-truss | (c) FCC unit cell + octet-truss |
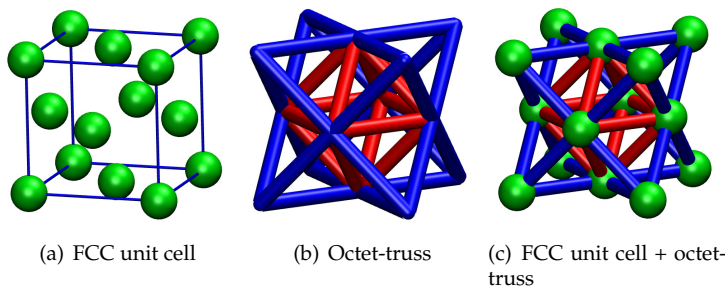
Figure 1.1: *a) Unit cell with face-centered spheres. b) FCC points connected by sticks to give an octet-truss geometry. (c) Structure obtained by merging a) and b). Subsequently this last geometry was tiled by a graphene net.*

Several 3D carbon-based triply-periodic structures were proposed in the past decades [Lenosky et al., 1992, Townsend et al., 1992], e.g schwarzites or Mackay crystals [Terrones and Mackay, 1993, Terrones et al., 1995] obtained by tiling minimal surfaces having negative Gaussian curvature. Several computational models of these structures were developed using a Monte Carlo approach [Townsend et al., 1992] or the Weierstrass representation [Terrones and Mackay, 1993]. Furthermore, recently, the electronic properties of cubic schwarzites [Park et al., 2010, Tagami et al., 2014] were investigated from ab-initio simulations.

Here, we present computer simulations of novel graphene nanotruss architectures with FCC crystal structure (Fig. 1.2) investigating their mechanical properties with atomistic resolution. Firstly, we compute the stiffness matrix. Subsequently, we perform simulations in tensile and compressive regimes, studying the stress-strain curves as a function of different geometries, with particular consideration to assessing local instabilities and mechanical hysteresis. Furthermore, observables characterising these FCC structures, such as Poisson ratio and scaling relations between the Young modulus and the density, are determined and compared to the performance of standard materials, such as graphite. Finally, since graphene nanotrusses could be potentially suitable for impact energy absorption and capable of propagating nanoscopic size effects to macroscopic scales, we investigate their energy absorption efficiency.

In designing a three-dimensional graphene-based nanomaterial, we combined

ideas coming from both nanotruss network desing and open-cell foams [Ashby, 2006]. The former are micrometric structures built joining struts in a regular fashion (see Fig. 1.1b), whereas the latter are porous materials in which pores are connected to each other. The periodicity of microtruss networks, particularly in their octet configuration (see Fig. 1.1b), enables a good scaling of their mechanical properties. In general, microtruss networks can be made by hollow or solid struts, the former showing – in general – better elastic properties. However, these materials are fragile and tend to break or deform irreversibly under compression, the principal point of failure being the connection between the struts.

Here, we explore the possibility of enhancing the properties of truss networks by a modification of the way in which the struts are connected. Taking inspiration from the structure of foams, we envisage a nanostructured material in which hollow carbon nanotubes are connected to spheres placed in FCC configurations. Similar materials have already been investigated in the case of body-centered cubic geometry, with emphasis on the mechanical properties under tension [Wu et al., 2013]. To underlie the growing interest in this kind of design, we note that a similar strategy to enhance the mechanical properties of octet-truss hollow structures has been subsequently proposed by Bonatti et al. [Bonatti and Mohr, 2017] in that case of macroscopic structures. The authors demonstrated by means of both, calculation and experiments, that hybrid truss sphere assembly (the geometry presented in this section) exhibited the highest strength and energy absorption potential at 20% relative density with respect to solid octet-truss, hollow sphere assembly, hollow octet-truss for stainless steel millimetric structures.

1.2   Modeling nanotruss geometries

To generate nanotruss networks, we imagine to cover with graphene a surface made by FCC spheres (see Fig. 1.1a) joined by struts in octet-truss geometry [Deshpande et al., 2001] (see Fig. 1.1b). The resulting surface is depicted in Fig. 1.1c.

Although nanotruss geometry is similar to schwarzite's, the latter is characterized by the presence of two separate, while contiguous, subspaces with the same spatial extension. In our case, we do not impose this limitation and, further, we let these two subspaces to have different spatial extension. Indeed, when graphene
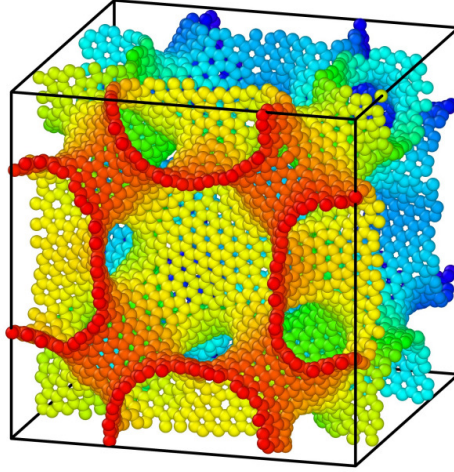
Figure 1.2: *FCC cell of the nanotruss. The faces of the cubic box are perpendicular to the [100], [010], [001] directions. In this figure, the nanotube diameter is 1.1 nm, the sphere diameter is 3.4 nm and the cube edge is 5.5 nm. Colors have been used for visualization purposes only and have no physical meaning.*

is grown on stacked nanoparticles, the resulting model is unlikely to represent a structure of minimal surface.

Once the nanotruss structure is defined, we have to perform a surface tessellation to create the actual carbon nanotruss. We achieve that by tiling the surface with regular triangles, and then using the Voronoi partitioning to dualize it [Jung et al., 2015, Taioli et al., 2016]. The triangulation is associated with a dense uniform packing, having a fixed lattice spacing, chosen to be almost double the carbon-carbon distance of graphene. This procedure follows closely that one reported in Ref. [Taioli et al., 2016], differing in the way the initial triangulation of the surface is achieved. This triangulation was performed using the molecular-dynamics package LAMMPS [Plimpton, 1995].

A number of points, enough to cover the entire surface, are distributed initially on a regular space-grid (Fig. 1.3c) and interact each other via a pair-wise Lennard-Jones (LJ) 12-6 potential, with potential parameters ($\sigma = 3.2$ Å, $\epsilon = 2 \times 10^{-4}$ eV) and a cutoff of 3.2 Å, such that they behave almost like soft spheres. The pa-

(a) Starting configuration   (b) Relaxation of the points   (c) Deletion of the points in excess
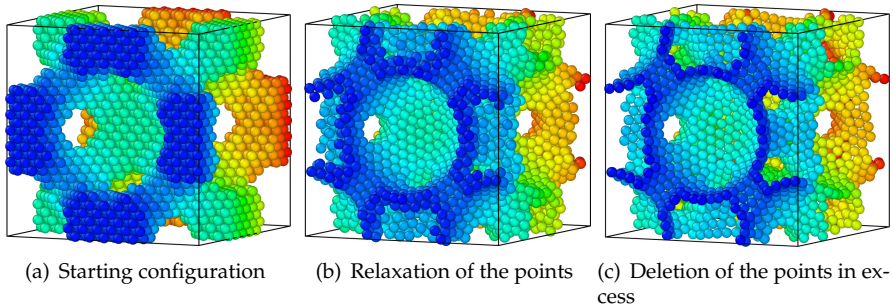
Figure 1.3: *The three step sequence for triangulating the surface. Panel a) shows the initial condition in which points are arranged in a regular grid. Subsequently, the position of the points is relaxed and they are attracted towards the surface by means of a molecular dynamics run (panel b). Finally, the points that do not belong to the first layer are deleted to avoid multilayer structures (c). The LJ net is ready for the Voronoi dualization, where it acquires a graphene-like net (see Fig. 1.2). Colors have been used for visualization purposes only and have no physical meaning.*
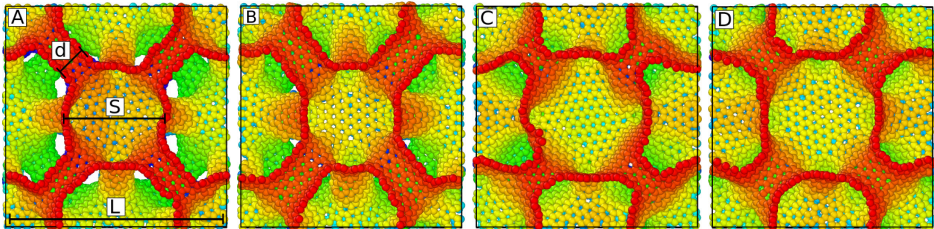
Figure 1.4: *Side views of the FCC cells. The cube faces are perpendicular to the [100], [010] and [001] directions. The diameter of the nanotubes is 0.8 nm for unit cells A and C, 1.1 nm for B and D. The sphere diameter is 2.7 nm for unit cells A and B and is 3.4 nm for unit cells C and D. The box edge is 5.5 nm for all four unit cells. Colors have been used for visualization purposes only and have no physical meaning.*

rameter's choice is such that the points in the final dualized configuration are distributed on the surface at a distance close to the carbon-carbon bond length $a_{CC} = 1.42$ Å. The particles were attracted to the surface using a LJ 9-3 potential ($\sigma = 2.0$ Å, $\epsilon = 1.0$ eV) with a cutoff of 10.0 Å between the points and the surface itself. After relaxation by means of a NVE integration with a viscous damping force (Fig. 1.3b), the particles distant more than 0.3 Å from the surface were deleted to realize a single layer structure (Fig. 1.3c). During the whole procedure

we imposed periodic boundary conditions, as detailed below.

A number of defects, distributed all over the structure, appear after the LJ triangulation. Here, for defects we mean LJ points having five or seven nearest neighbors. To generate nanotrusses that provide models for sp^2-bonded carbon atoms in graphene, one needs to apply a topological dualization (Voronoi partitioning) to the LJ optimized lattice. We initially computed the adjacency matrix of each particle, where a neighbour was defined as a particle closer than $\sqrt{3} \times a_{CC}$. Distances were evaluated in 3D space and not on the surface. As a final step, we took the Voronoi dual of the points triangulating the surface, using a refining procedure [Taioli et al., 2016] to obtain a configuration of carbon atoms containing only pentagonal, hexagonal and heptagonal rings. These configurations were further annealed by MD with AIREBO-type potentials to obtain the optimized carbon nanotruss networks.

It is worthwhile to note that in evaluating the distances in 3D space the Voronoi dualization automatically smooths possible steps at the intersection between different parts of the surface (e.g. tube-sphere in our case). Heptagonal and pentagonal rings appear in these structures as can be seen in Fig. 1.2, where we show a unit cell of a model nanotruss obtained using this procedure. In the following, we will refer to pentagonal or heptagonal rings as topological defects.

The number of defects should be independent from the dimension of the unit cell, indeed it is manily related to the local curvature. This means that foams with small unit cells tend to be less performant with respect to their mass due to the higher ratio between the number of defect and the total number of atoms. To compare these kind of foams with experimental one is anyway difficult because to increase the pore dimension of the foams generally it necessary to increase the number of graphene layers, changing the nature of the foams walls.

Nanotruss networks are uniquely defined by fixing the edge length of the cubic box L, the diameter of the nanotubes d and the diameter of the spheres S. Four different structures presenting high connectivity at the nodes (12 in our case) and shown in Fig. 1.4, have been obtained by modifying these parameters, as reported in Tab. 1.1. Using these carbon-based structures, we investigate the dependence of mechanical properties on sphere's and nanotube's diameters, and on cell orientation.

13

Unit cell	Sphere diameter S (nm)	Nanotube diameter d (nm)	Box side length L (nm)
A	2.7	0.8	5.5
B	2.7	1.1	5.5
C	3.4	0.8	5.5
D	3.4	1.1	5.5

Table 1.1: *Parameters used to build the four nanotruss unit cells reported in Fig.1.4.*

In order to study the mechanical properties of these structures as a function of cell orientation, the calculation supercells were obtained by periodically replicating along the the [100] direction the unit cell of each structure, by rotating and finally truncating the supercell to obtain configurations with faces perpendicular to the [110] and [111] directions. All considered samples are composed of more than one unit cell to limit the influence of the boundary conditions on the possible reciprocal sliding of spheres' planes. In this regard, starting from four unit cells, we built four structures for each direction of sampling. The samples obtained using the A, B, C and D unit cells will be numbered from 1 to 4 onwards and are reported in Tab. 1.1. The number of atoms in our samples, i.e. in each computational supercell, obtained by periodically repeating unitary cell along the x, y, and z directions, is dependent on the direction in which they will be loaded. This value is approximately equal to 4×10^4 for the [100] direction, 2×10^4 for the [110] and 3×10^4 for the [111], respectively. Thus, for example, we used a sample composed by $2 \times 2 \times 2$ unit cells to test the nanotrusses in the [100] direction. This is 8 times larger than the unit cell, having approximately 5000 atoms; thus, the number of atoms can be considered of the order of 4×10^4. The dualization procedure was performed on the unit cells to reduce the computational cost, due to its unfavourable scaling with the number of atoms involved. The basic building blocks so obtained were eventually replicated and the supercells subjected to annealing before calculating mechanical properties, in order to decrease the noise relative to the measured quantities.

1.3 Computational methods

Molecular dynamics simulations were carried out using LAMMPS [Plimpton, 1995]. The carbon-carbon atomic interaction was modeled through the AIREBO potential [Stuart et al., 2000]. Atomic configurations were visualized by using the OVITO package [Stukowski, 2010] or VMD [Humphrey et al., 1996]. The samples were annealed to randomize the presence of defects within the calculation supercell. Samples were first heated at 3500 K and then equilibrated at this temperature for 100 ps. Finally, they were cooled down to 700 K in 100 ps using a viscous damping force. The annealing was performed using the standard value for the cutoff parameter for the REBO part of the potential and performed within the microcanonical ensemble (NVE). We began the mechanical characterization of the samples computing the stiffness matrix. For anisotropic materials the stress and strain tensors are related by a fourth rank tensor, having 21 independent elements, as follows:

$$\sigma_{ij} = C_{ijkl}\varepsilon_{kl} \tag{1.1}$$

where C is named *stiffness tensor*. In the particular case of cubic symmetry the stiffness tensor has only three terms and the linear system of equations can be written explicitly, as follows:

$$\begin{pmatrix} \sigma_{xx} \\ \sigma_{yy} \\ \sigma_{zz} \\ \sigma_{yz} \\ \sigma_{zx} \\ \sigma_{xy} \end{pmatrix} = \begin{pmatrix} C_{11} & C_{12} & C_{12} & 0 & 0 & 0 \\ C_{12} & C_{11} & C_{12} & 0 & 0 & 0 \\ C_{12} & C_{12} & C_{11} & 0 & 0 & 0 \\ 0 & 0 & 0 & C_{44} & 0 & 0 \\ 0 & 0 & 0 & 0 & C_{44} & 0 \\ 0 & 0 & 0 & 0 & 0 & C_{44} \end{pmatrix} \begin{pmatrix} \varepsilon_{xx} \\ \varepsilon_{yy} \\ \varepsilon_{zz} \\ 2\varepsilon_{yz} \\ 2\varepsilon_{zx} \\ 2\varepsilon_{xy} \end{pmatrix} \tag{1.2}$$

where the matrix is named *stiffness matrix*.

With regard to the simulations in compressive and tensile regime, all samples were equilibrated at zero pressure and at the temperature of 1 K with Nosé–Hoover barostat and thermostat. The adaptive cutoff parameter of the potential has been set to 2.0 Å to better describe the near-fracture regime [Shenderova et al., 2000].

The equations of motion were solved with the velocity-Verlet integration method using a time step of 1 fs. Mechanical properties were assessed in the isobaric-isothermal ensemble (NPT), adding a drag term to smooth out the pressure oscillations. The uni-axial tensile strain was applied up to the sample fracture in each case.

The engineering strain parallel to the direction of deformation is defined as

$$\varepsilon = \frac{L - L_0}{L} = \frac{\Delta L}{L} \tag{1.3}$$

where L_0 and L are the starting and current length of the sample in the direction of loading. To determine the stress, the pressure stress tensor components in response to the external deformation are computed as [Thompson et al., 2009]

$$P_{ij} = \frac{\sum_k^N m_k v_{k_i} v_{k_j}}{V} + \frac{\sum_k^N r_{k_i} f_{k_j}}{V} \tag{1.4}$$

where i and j label the coordinates x, y, z; k runs over the atoms; m_k and v_k are the mass and velocity of k-th atom; r_{k_i} is the position of k-th atom; f_{k_j} is the j-th component of the total force on the k-th atom due to the other atoms; and, finally, V is the volume of the simulation box. The pressure in Eq. 1.4 includes both kinetic energy (temperature) and virial term. Notice that the force appearing in Eq. 1.4 is the sum of the pairwise, angle, dihedral, improper and long-range contributions. The computed stress is the *true stress* because the pressure is measured with respect to the instantaneous section area of the samples. The uni-axial compressive strain was applied up to reaching 25 % and 50 % total strain. The applied strain rate is chosen equal to $0.001\ \mathrm{ps}^{-1}$, such to converge the Young modulus and tensile strength, as shown in Fig. 1.5. Stress and strain were saved every 1000 time steps.

The stress-strain curve was computed at 1 K, since molecular dynamics is usually computationally faster than using a minimization procedure. The same approach has been previously adopted by other groups dealing with similar problems (see e.g. [Wu et al., 2013]). This introduces a small kinetic contribution, which is approximately 2% of the total stress, almost uniformly distributed along the
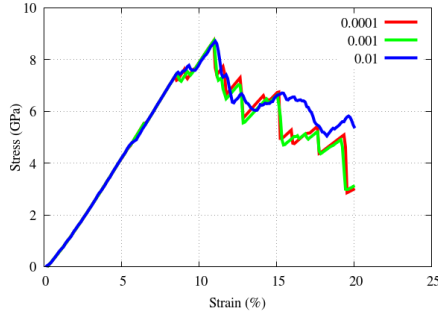
Figure 1.5: *Stress-strain curve dependence on strain rate in ps^{-1} for the [100] unit cell 4.*

stress-strain curve. Local maxima of the kinetic contribution up to 4% of the total stress can be found at the points where the structures collapse, due to the small temperature increase. The influence of the kinetic term is clearly small enough to have negligible effect on our simulations.

The observables that we calculate to characterize the mechanical properties of the nanotrusses are, in addition to the stiffness tensor, the Young modulus, fracture stress and fracture strain. The toughness is also evaluated as the area under the stress-strain curve up to the fracture stress. Indeed, the samples have no plastic deformation but several sequential fractures. Stress-strain curves of carbon nanotrusses present a not fully linear behaviour (Fig. 1.5). Thus, the definition of one only slope does not guarantee an accurate fit of this curve and we are forced to introduce two different values of the Young modulus to characterize the mechanical behaviour. In particular, the first value of the Young modulus is obtained as the tangent at zero strain, while the second one from a linear fit between 5% to 8% strain.

We also performed the calculation of the Poisson ratio ν, defined as the negative ratio between the transverse deformation ε_T and the longitudinal one ε_L:

$$\nu = -\frac{\varepsilon_T}{\varepsilon_L} \tag{1.5}$$

Here we extend the concept of Poisson ratio to deformations beyond the linear

17

regime, and use it to quantify the lateral deformation of the material. A similar extension is done for the Young modulus.

1.4 Results and discussion

1.4.1 Stiffness matrix

The elastic properties of the nanotrusses were first assessed by computing the stiffness matrix. The kinetic energy is not present in the calculation of the stiffness matrix, as this computation was performed using molecular mechanics simulations without a temperature term. The outcome of this computation will be useful also to check if the choice of the structures represents a realistic model of these materials. Indeed, the stiffness matrix of realistic systems can be used to measure the degree of anisotropy by comparison with a perfect FCC cubic cell. The computed stiffness matrix for the sample 3, with faces perpendicular to [100], [010] and [001] directions, is:

$$
\begin{pmatrix}
63.0 & 12.3 & 13.2 & -0.43 & 0.19 & -0.92 \\
 & 58.9 & 12.4 & -0.28 & 0.28 & -1.14 \\
 & & 58.5 & 0.59 & 0.97 & 0.32 \\
 & & & 14.0 & 0.11 & 0.71 \\
 & Sym & & & 14.6 & -0.40 \\
 & & & & & 13.9
\end{pmatrix}
$$

where the values are reported in GPa.

The matching with the cubic material stiffness matrix in Eq. 2 is not perfect, as small non-zero terms appear in the upper right part of the matrix. Additionally, terms that must be in principle equal show some discrepancies. The reason of this anisotropy is principally due to the choice of the cell dimension used for the Voronoi tessellation of the surface. Applying the dualization to a single unit cell, the graphene net has to be periodic over a distance of the box edge L and the room available to accommodate the defects is quite small.

1.4.2 Tension

The mechanical properties of nanotruss networks, such as Young modulus, fracture strain and tensile stress, were further investigated via the assessment of their stress-strain curves. In Fig. 1.6, we report the stress-strain curve for the four samples along the direction [100] and in Fig. 1.7 three snapshots of the sample 4 under tension.

The stress-strain curves show a typical elastic behavior for small deformations up to the tensile strength (snapshots of the respective configurations are shown in panels a and b in Fig. 1.7), followed by a descending part that corresponds to the fracture of the samples (as evidenced in the snapshot reported in panel c of Fig. 1.7). The absence of a plastic plateau and instead the presence of a sharp maximum in the stress means that nanotruss networks display the brittle nature of the parent material, i.e. graphene. In this study we do not attempt to extract informations from the part of the stress-strain curves beyond the fracture strain. Indeed, at variance with the Young modulus or specific toughness, the crack propagation can be strongly influenced by the size of the simulation box and periodic boundary conditions.

All the curves present a fracture strain of about 10% so that the tensile strength is roughly proportional to the Young modulus. The network with the largest nanotube and sphere diameters (4) has larger Young modulus and tensile strength than the number 1, which present the smallest values (Fig. 1.6). The other two cases give comparable results. A similar response is found for the [110], and [111] directions.

The values of Young modulus, tensile strength and fracture strain are reported in Tab. 1.2. We also report the values for graphene as calculated using the AIREBO potential (cutoff set to $2.0\,\text{Å}$) in Ref. [Zhao et al., 2009]. We see an increase of Young modulus and tensile strength for evidently more optimized structures, passing from sample 1 to sample 4. The shape and dimension of the nodes play an important role in the deformation of hollow truss networks, as recently shown for microtruss networks [Schaedler et al., 2011, Valdevit et al., 2013].

The stiffening behavior (i.e. parabolic shape of stress-strain curve in elastic regime) is due to the realignment and bending of the struts at smaller strain, and the stretching-dominated deformation of the realigned struts at larger strain, as
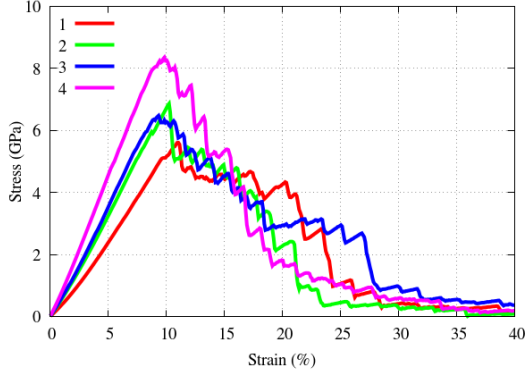
Figure 1.6: *Stress-strain curves of the four nanotruss networks under uni-axial tension along the [100] direction. The four curves present a Young modulus roughly proportional to the tensile strength and a fracture strain of about* 10%. *Because the crack propagation can be strongly influenced by the size of the simulation box and by the periodic boundary conditions, the part of the curves beyond the maximum of stress should not be taken into account for a physical interpretation without the study of possibly box-size-dependent behavior.*

noted in Ref. [Wu et al., 2013] for similar structures. In this regard we can study the stiffening using the ratio between Young modulus 2 and 1, which takes the highest value for the sample 1 (1.61). Samples 2 a 3 give comparable results (1.37, 1.33). For the last sample (4) we find the lowest value (1.19). We underline the similarity between the behavior of the samples 2 and 3 in tension in contrast to what it will turn out in the compressive case. In fact, they have different geometries but almost the same mass density.

In Tab. 1.3 we report the specific modulus and the specific strength, which define the values per mass density. Furthermore, in the same table is reported the specific toughness, calculated as the total area under the stress-strain curves up to fracture strain, per mass density. By comparing Tabs. 1.2 and 1.3, we note that even though the Young modulus and tensile strength for the nanotrusses are respectively two and one order of magnitude smaller than those reported for graphene, we obtain a different scenario when considering the specific strength and the specific modulus. The density of these nanotruss networks is about one

(a) 0% strain   (b) 10% strain   (c) 20% strain
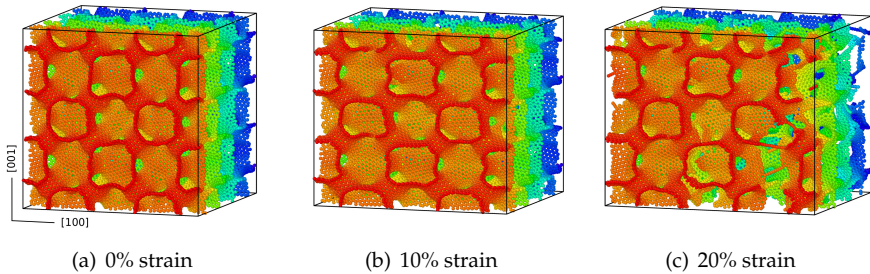
Figure 1.7: *Images of sample 4 under traction in the [100] direction. The sample is built by replicating the unit cell D in the space building up a $2 \times 2 \times 2$ unit cell (a). The deformation is applied in the [100] direction. At 10% strain the sample is near to the maximum stress and failure strain where cracks start to grow (b). In image (c), at 20% strain, cracks are larger and there is not only one fracture but cracks formed in many positions. Colors have been used for visualization purposes only and have no physical meaning.*

Sample	Young modulus 1 (GPa)	Young modulus 2 (GPa)	Tensile strength (GPa)	Fracture strain (%)
1	36	58	5.6	11.1
2	54	74	6.8	10.2
3	58	77	6.5	9.3
4	79	92	8.3	9.8
Graphene	10^3	10^3	98.5	16.5

Table 1.2: *Young modulus, ultimate strength, and fracture strain of the systems studied under tension along the [100] direction. These values are compared with the average of those reported for armchair and zigzag graphene using AIREBO potential [Zhao et al., 2009].*

third of that of graphite, thus enhancing the specific mechanical properties of these materials with respect to graphite.

Considering Fig. 1.7, we note that cracks propagate from defective sites as, for example, a pair of heptagons. The presence of defective sites is responsible for the small value of the fracture strain, compared to graphene. Furthermore, for defected carbon nanotrusses, as those studied in this work, crack propagation is diffuse, differently from ideal materials. Indeed, for ideal nanotube-fullerene net-

Sample	Density kg m^{-3}	Specific modulus 1 (MNm kg^{-1})	Specific modulus 2 (MNm kg^{-1})	Specific strength (MNm kg^{-1})	Specific toughness (MJ kg^{-1})
1	634	57	91	8.8	0.5
2	707	76	105	9.6	0.5
3	705	82	109	9.2	0.4
4	692	114	133	12.0	0.6
Graphite	2250	444.4	444.4	43.8	-

Table 1.3: *Density, specific modulus and specific strength of the four samples studied under tensile strain along the [100] direction. Specific toughness is calculated as the area under the stress-strain curve up to fracture strain per mass density.*

works cracks preferably are localized at the nanotubes-fullerenes junctions [Wu et al., 2013].

In the next section we will focus on the compressive regime in which a geometry-dependent behavior emerges more strongly than in the tensile one.

1.4.3 Compression

In this section we present the results obtained for the samples under compressive load. At variance with the tension case, the compressive response is strongly related to the nanotruss geometry as well as to the direction of compression. In Fig. 1.8 we report the stress-strain curve in compression along the [111] direction, which presents the most interesting features. The deformation reaches 50% strain for the largest compression, for which the main features of the compressive response are shown.

Indeed, observing Fig. 1.8, the stress-strain curves are basically characterized by three regimes, typically found in foams and energy absorbing materials. At small strain we are in elastic regime, and the material is characterized by a full recovery to the original shape when the load is removed. Subsequently we observe a plateau, representative of the sample collapse at a nearly constant stress, by buckling or fracture of the building blocks (nanotubes and graphene spheres). Finally, one finds a steep ramp in the stress-strain curve, representing full collapse or a densification regime of the structures.
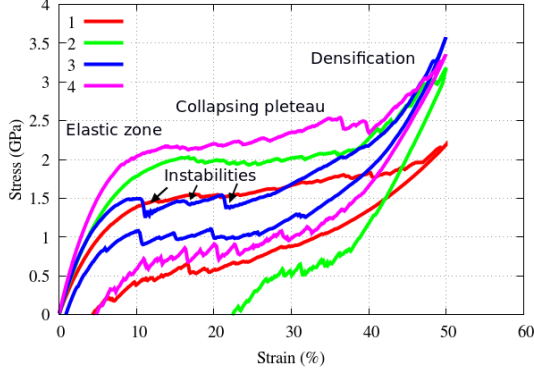
Figure 1.8: *Stress-strain curves of the four nanotruss networks under uni-axial compression along the [111] direction up to 50% strain. At higher stress one finds the compressive part of the curve, while the unloading part is at lower stress.*

Sample	Young modulus (GPa)	Plateau stress between 10-40% strain (GPa)	Residual deformation 25% (%)	Residual deformation 50% (%)
1	27	1.6	0.6	4
2	33	2.0	1.5	22
3	36	1.6	0.2	1
4	42	2.3	0.4	5

Table 1.4: *Young modulus, plateau stress, and residual deformation of the four samples under uni-axial compression in the [111] direction.*

The four samples reported in Fig. 1.8 behave similarly in the elastic regime. However, samples 2 and 3 present an inverted response with respect to traction, and the stress for sample 2 in compression is higher than that for sample 3. In the plateau, a geometry-related response occurs. Sample 1 shows a nearly flat plateau that does not approach the densification regime up to 50% strain. Samples 2 and 4 present a collapsing plateau before approaching the densification regime at high strain. For samples 1, 2 and 4 one can see from the unloading part of the stress-strain curve that the deformation is partially plastic, without full recovery of the original shape at zero stress. This is a clear signature of mechanical hysteresis in these systems.

23

(a) Strain 0%   (b) Strain 20%
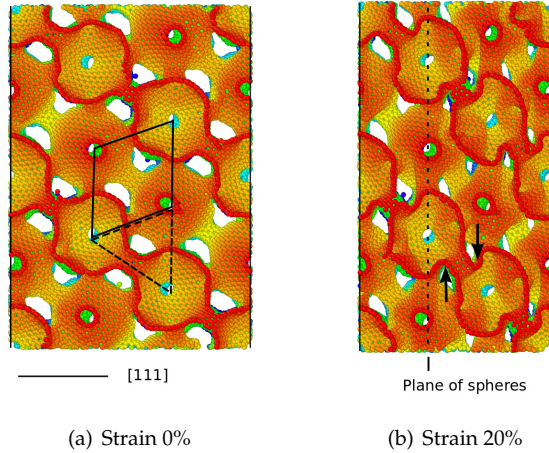
Figure 1.9: *Nanotruss network number 3 under uni-axial compression along the [111] direction. The first image is the undeformed sample; the second is a snapshot at 20% strain. The centers of the graphene spheres divide the space in two volumes of different shape: an octahedron (rendered in red in Fig. 1.1b) and a tetrahedron (rendered in blue in Fig. 1.1b). These two volumes are reported in image a). It is clear from image b) that the tetrahedrons are loaded from one vertex towards the center of their base so that the nanotubes are forced to rotate during the compression. Notice the collapse of the planes of spheres in the second image. In particular, for each plane collapsed there is a peak in the stress-strain curve as reported in Fig. 1.8. Colors have been used for visualization purposes only and have no physical meaning.*

.

Sample 3 presents a response that is very different from the other samples, showing a number of peaks in the plateau of the stress-strain curve (Fig. 1.8). Each peak is related to the collapse of a plane, as shown in Fig. 1.9. This type of response, peculiar to sample 3, has been found only along the [111] direction. It is worthwhile noting that this response depends on the ratio between the nanotube's and the sphere's diameters. The collapse of the planes is essentially elastic, indeed the sample presents only a small residual deformation at zero stress.

Finally, we note that the partial insertion inside the sphere of the nanotubes that carry the compressive load is caused by a global instability of the sphere's planes: all the nanotubes that are loaded in compression are influenced in the same manner.
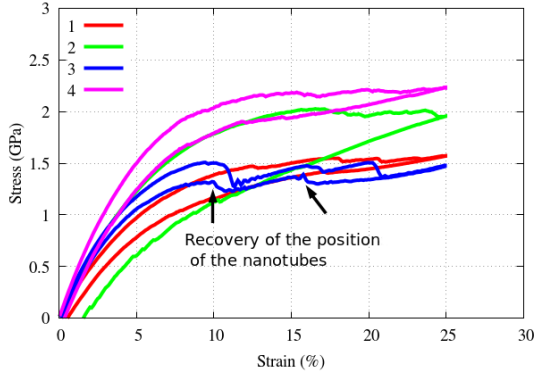
Figure 1.10: *Stress-strain curves of the four nanotruss networks under uni-axial compression along the [111] direction up to 25% strain. The compressive part of the curve is that at higher stress, the unloading part at lower stress. Sample 3 presents a stress-strain curve qualitatively different from the other samples. It presents three peaks in the loading part of the curve and two peaks in the unloading part. These peaks are due to the global instability of the planes of spheres, as shown in Fig. 1.9.*

The centers of the graphene spheres divide the space in two volumes of different shape: an octahedron (rendered in red in Fig. 1.1b) and a tetrahedron (rendered in blue in Fig. 1.1b). These two volumes are reported in panel a) in Fig. 1.9. The tetrahedrons are loaded from one vertex towards the center of their base, forcing the nanotubes to rotate during the compression. The load acts in the direction of stabilizing the structure as, remarkably, the samples do not present reciprocal sliding of spheres' planes. This means that further simulations in this load direction could be performed on a single unit cell without loss of generality. Indeed, for samples in which is present a transverse sliding of the planes the boundary conditions as well as the parity of the number of planes in the simulation cell play a critical role. In the simplest case of a unit cell with only a plane, for example, the sliding is completely prevented.

In Fig. 1.10 the compressive stress-strain curves up to 25% strain are reported. The unloading part of the curve for sample 3 presents some stress peaks due to the repositioning of nanotubes into their original positions. The number of oscil-

lations is related to the number of planes in the sample; therefore, in the limiting case of a bulk material, we expect that the number of oscillations will increase reaching a flat plateau.

Full recovery after compressive deformation similar to that found for sample 3 has been reported, for example, in carbon nanotube bundles [Cao, 2005] and in ultralight boron nitride foams [Yin et al., 2013]; in these systems, the deformation in absence of plastic strain is allowed by rotation of the internal components.

In Tab. 1.4 we report the Young modulus, plateau stress and residual deformation of the four samples, under uni-axial compression in the [111] direction.

In Fig. 1.11 we report the stress-strain curve in compression along the [100] direction up to 25% and 50% strain. Along this direction the overall behavior of the samples 1 is very different from that of the samples 2, 3 and 4. Indeed, it presents a smooth trend of the stress strain curve under compression and a stress value lower than the other three samples. The samples 2, 3 and 4, present a very similar stress value up to 25% strain. Differently from the compression along the [111] direction, here we found nearly no residual deformation at zero stress for 25% strain while for 50% strain the residual deformations at zero stress lie in the range $30 - 40\%$ for all the samples. Interestingly, there is a sort of hysteresys loop in the range $10 - 20\%$ strain for the sample 4 as reported in the upper panel for 25% strain.

In Fig. 1.12 are reported two snapshots of the sample 4 under 8 and 20% compressive strain corresponding to the instabilities found in the stress strain curves presented in Fig. 1.11. As noted in the case of the deformation along the [111] direction the number collapses is proportional to the number of unit cell in the sample. In this case we found only two collapses due to the fact that the considered supercell is $2 \times 2 \times 2$ unit cells. We expect, also in this case, that the number of oscillations will increase with the increasing of the number of cells, reaching a smooth curve for a bulk material.

In the next section we will focus on a quantitative evaluation of the Poisson ratio for the samples 3 and 4 in the [110] direction, for which an auxetic response emerges. For this direction the stress strain curves do not show particular features. Indeed, as we will show in the following, differently from the previous cases along the [100] and the [111] directions, the nanotubes that are involved in the instability
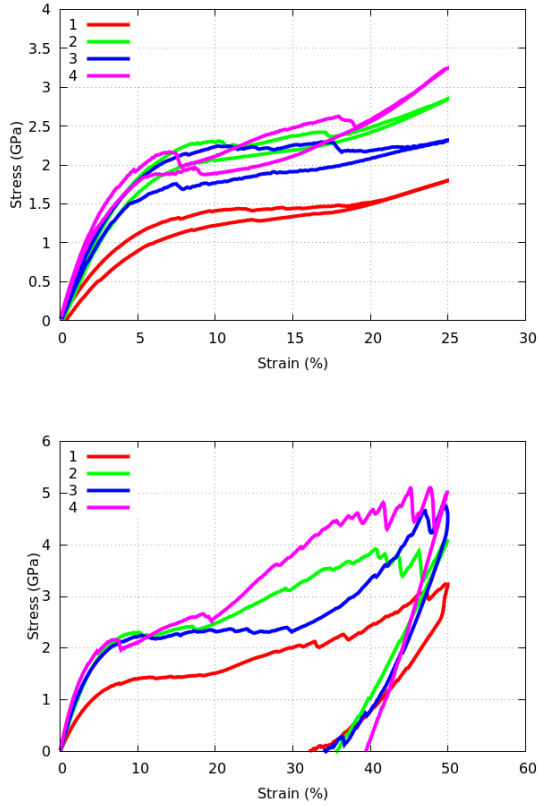
Figure 1.11: *Stress-strain curves of the four nanotruss networks under uni-axial compression along the [100] direction. In the upper panel the deformation is up to 25% strain while in the lower one up to 50% strain.*

carry only partially the total load.

(a) Strain 8%   (b) Strain 20%
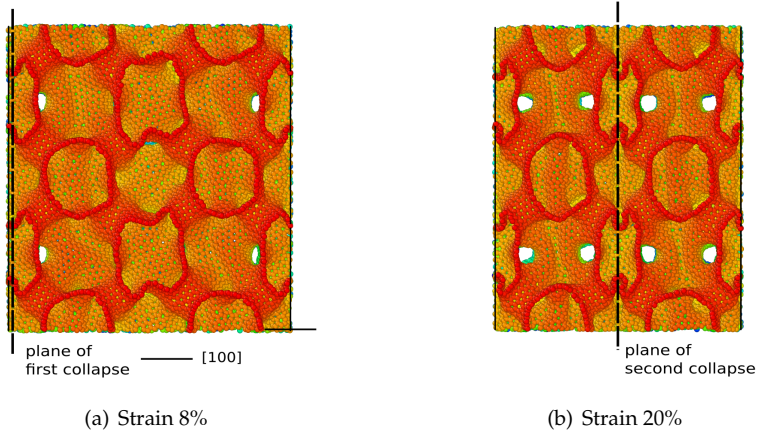
Figure 1.12: *Nanotruss network number 4 under uni-axial compression along the [100] direction. The first image is a snapshot at 8% strain, after the first collapse. The second snapshot shows the sample at 20% strain, after the second collapse. Colors have been used for visualization purposes only and have no physical meaning.*

.

1.4.4 Negative Poisson ratio

The quantity characterizing the materials' response in the direction orthogonal to compression is the Poisson ratio ν, defined as the ratio between the negative transverse and longitudinal strain. Commonly, materials have a positive Poisson ratio, meaning that they expand in the direction orthogonal to the external compressive load (e.g. steel, $\nu = 0.3$). Under compression in [110] direction we found negative Poisson ratio for samples 3 and 4.

This negative Poisson ratio is strictly connected to an interesting feature, not present in the compression along the other directions, that can be found in the [110] direction. This characteristic, sketched in Fig. 1.13 for sample 3, is the longitudinal insertion of the nanotubes inside the spheres. Nevertheless, the stress-strain curve in the [110] direction does not show particular engaging features, as the load is carried by the other nanotubes. This local instability, related to a single nanotube and not to a whole plane of spheres, has been also found in sample 4 along the [110] direction.

(a) Strain 0%	(b) Strain 20%	(c) Strain 30%
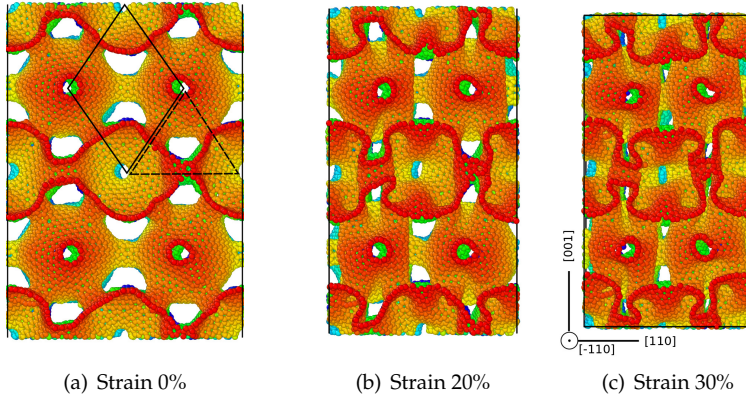
Figure 1.13: *Three snapshots of sample 3 under uni-axial compression in the [110] direction at 0 %, 20 % and 30 % strain. In image a) are shown the positions of an octahedron and a tetrahedron. In this case the load is aligned with an edge of each tetrahedrons. Due to the nanotubes insertion there is a contraction in the transverse direction [001] direction. The Poisson ratio with respect to this direction has negative values for strain higher than 10 %. With respect to the [-110] direction (out of the page) the Poisson ratio is initially positive and then tends to zero as strain increases to 30 %. The images are to scale.*

Our simulations also show that the nanotube insertion presents three stable configurations. In two of these configurations, only the bottom part of the nanotube enters one of the adjacent spheres, while in the third one both top and bottom sides of the nanotubes are inserted. We note that this behavior introduces a new degree of freedom under compression for each nanotube aligned with the [110] direction.

In Fig. 1.14 we report two snapshots of a single sphere of the sample 3 under compression. The insertion increases the local curvature of the surface, and, as for the [111] direction, this could be useful to enhance the adsorption or desorption of gases. Due to the symmetry of the structure, the nanotubes in the horizontal plane perpendicular to the [110] direction are free of moving under a second load applied in the direction [-110]. For longer nanotubes, the inserted extremities could interact each other giving collective patterns in the horizontal plane, in particular under bi-axial compression (in directions equivalently to the [110] and [-110] directions).

(a) Strain 0%   (b) Strain 20%
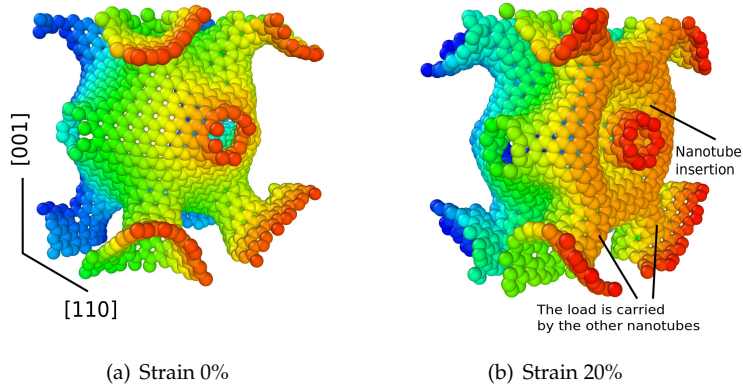
Figure 1.14: *The two snapshots show a single sphere of sample 3 under uni-axial compression in the [110] direction at 0 % and 20 % strain. Panel a) shows the undeformed sphere. Panel b) reports the sphere during the deformation.*
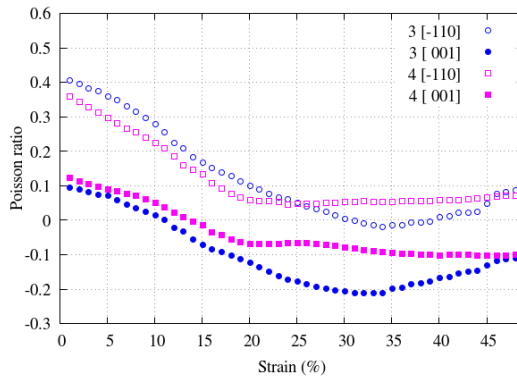
Figure 1.15: *Poisson ratio of samples 3 and 4 under compression in the [110] direction. The Poisson ratios are between the [110] direction (of load) and the other two directions, [-110] and [001] as indicated by the labels. See Fig. 1.13 for graphical representation of the axes. These two samples present an auxetic response (negative Poisson ratio) for large deformations.*

In Fig. 1.15 we report the Poisson ratio for samples 3 and 4 under uni-axial compression in the [110] direction. The Poisson ratio is monotonically decreasing

in both the samples. Indeed, these two structures are characterized by positive values of ν for small strain in the [-110] and [001] directions. At higher strain, the Poisson ratio of the sample 3 along the [-110] and [001] directions presents a minimum at around 35 % strain. A similar trend is found for the sample 4 with the presence of a plateau starting from 20 % strain. Furthermore, we note that Poisson ratios along the z direction become negative. A negative Poisson ratio means that, if a compressive load is applied in the [110] direction, the material tends to increase its density under the applied load. This feature of carbon foams could be useful for delivering effective high-impact energy absorption. Finally, we note that in this case the compressive load tends to stabilize the structure only for small strain, whereas, for high strain, a sliding of the spheres' plane is found.

1.4.5 Density scaling relation

The Young modulus E of microstructures obeys a semi-empirical power-scaling law with relative density as follows [Ashby, 2006]:

$$\frac{E}{\tilde{E}} = \alpha \left(\frac{\rho}{\tilde{\rho}} \right)^{\beta} \tag{1.6}$$

where $\tilde{E}$ and $\tilde{\rho}$ are the Young modulus and the density of the bulk material respectively, α is a proportionality coefficient and β depends from the micro-architecture of the material. In our case $\tilde{E}$ is the Young modulus of graphene, which composes the nanotrusses. FCC nanotrusses, where each node is connected to 12 first neighbours with similar struts, present stretching-dominated response [Deshpande et al., 2001]. Indeed, the octet-truss satisfies Maxwell's criterion for static determinacy. This criterion in three dimensions is given by

$$b - 3j + 6 \geq 0 \tag{1.7}$$

where b and j are the number of struts and nodes, respectively, in the unit cell. For this type of octet-truss lattice material [Deshpande et al., 2001] $\alpha = 0.3$ and β is equal to 1. Differently, for bending-dominated structures such as foams, the scaling relation Eq. 1.6 is satisfied with $\alpha = 1$ and $\beta = 2$.

Sample	Relative density (%)	Young modulus linear relation (GPa)	Young modulus parabolic relation (GPa)
1	28.2	319.4	340.1
2	31.4	350.1	334.2
3	31.3	383.0	366.7
4	30.8	455.2	444.0

Table 1.5: *Relative density with respect to graphene, Young modulus of graphene that constitutes the nanotruss networks calculated by means of the relation in Eq. (1.6) with $\alpha = 0.3$ and $\beta = 1$ (linear relation) or $\alpha = 1$ and $\beta = 2$ (parabolic relation).*

Due to the number of parameters that influence the scaling relations, one should test different geometries, unit cell dimensions and numbers of layers. This analysis would be interesting, however it would require much more extensive simulations than we car currently afford.

We plan to use the scaling relation Eq. 1.6 to estimate the average Young modulus $\tilde{E}$ of the graphene sheets that compose the nanotruss networks, using as coefficients and exponents those valid in the limiting cases of linear and parabolic scaling laws. Furthermore, we use the bulk density $\tilde{\rho}$ of graphite ($\tilde{\rho} = 2250$ kg m^{-3}). Due to the presence of defects in the nanotrusses one can expect a reduction of the Young modulus of our structures with respect to graphene ($\tilde{E} = 1.0$ TPa [Zhao et al., 2009]) to values typically found in nanometric graphene sheets (in the range $100 - 500$ GPa [Becton et al., 2015]).

In Tab. 1.5 we report the computed Young modulus of graphene in the case of linear and parabolic density scaling law. We note that the estimated Young modulus is indeed lower than pristine graphene and is in the range $100 - 500$ GPa.

While we use a linear and a parabolic scaling law to estimate the intrinsic Young modulus of graphene, for tannin-derived carbon-based foams the exponent appearing in Eq. (1.6) was found close to 3 [Celzard et al., 2010]. A similar value, was also found for silica aerogels by Gross and Fricke [Gross and Fricke, 1995]. To reach this value, higher than what can be obtained by simple scaling of the foam, a number of dangling struts were introduced by the authors. Since our nanotruss networks do not present "elastically ineffective" parts, we consider 2.0 a reasonable upper bound for the exponent of Eq. (6). Interestingly, a Young

modulus of 16 MPa for a density of 0.055 relative to the bulk can be achieved with tannin-derived carbon-based foams [Celzard et al., 2010]. However, since we do not know the exact scaling density relation for our nanotruss networks, a comparison between the mechanical properties of these two types of structures is not presently conceivable.

1.4.6 Energy absorption

Due to the possible application of nanotruss networks to impact absorption, it is important to study the mechanical behavior of nanotruss and compare that behavior with standard materials for energy absorption.

The compressive stress-strain curves can be used to assess the performance of a material with regard to its energy absorption properties. Owing to the similarity of the stress-strain curves of our samples to those typical of absorber materials, we evaluated the most relevant quantities used to describe this property, such as: the *crush force efficiency*

$$\eta(\varepsilon) = \frac{F_{\mathrm{av}}(\varepsilon)}{F_{\mathrm{max}}(\varepsilon)} \tag{1.8}$$

where $F_{\mathrm{av}}(\varepsilon)$ is the average of the stress between 0 and ε strain and $F_{\mathrm{max}}(\varepsilon)$ is the maximum stress up to strain ε. For the ideal energy absorber $\eta = 1$.
The *stroke efficiency*

$$S_E = \varepsilon_{\mathrm{dens}} \tag{1.9}$$

that represents the strain on the edge of densification and gives an estimation of the ratio between the useful length to absorption and the total length.
The *specific energy absorption* is the energy absorbed per unit of mass

$$SEA = \frac{E_{\mathrm{t}}}{m} \tag{1.10}$$

where m is the mass and the *total energy* absorbed

$$E_t(\varepsilon) = V \int_0^\varepsilon \sigma(\varepsilon') \, \mathrm{d}\varepsilon' \tag{1.11}$$

is the area under the stress-strain curve up to strain ε times the sample's volume

Sample	Crush force efficiency η	Stroke efficiency S_E	Specific energy absorption compression 50% (MJ kg^{-1})	Specific energy loading-unloading 50% (MJ kg^{-1})
1	0.7	47	1.2	0.5
2	0.6	43	1.4	1.0
3	0.5	42	1.2	0.3
4	0.7	40	1.6	0.8

Table 1.6: *Crush force efficiency, stroke efficiency, and specific energy absorption calculated up to 50% strain for the four samples under uni-axial compression in the [111] direction.*

V.

All previous quantities, except the stroke efficiency, are functions of the strain and in order to compare different materials they are usually evaluated at the densification strain $\varepsilon_{\mathrm{dens}}$. The densification strain is evaluated so to maximize the *energy absorption efficiency* [Li, 2006, Avalle et al., 2001]

$$\eta_t(\varepsilon) = \frac{1}{\sigma(\varepsilon)} \int_0^\varepsilon \sigma(\varepsilon')\,\mathrm{d}\varepsilon' \tag{1.12}$$

These quantities are reported in Tab. 1.6 for the four samples compressed in the [111] direction. The amount of absorbed energy is reported at 50% strain that is a standard strain for the evaluation of the performance of energy absorption materials. This value is higher than $\varepsilon_{\mathrm{dens}}$ for some samples, however for comparative purposes is preferable to choose a common value for strain. The best performances are obtained for sample 4.

We compare these values to those of typical absorbers, such as aluminum foams, high strength steel or bulk aluminum. The order of magnitude of the specific energy absorption in aluminum foams, high strength steel and bulk aluminum is of about 10^{-2} MJ kg^{-1}, thus much lower than that of the carbon nanotruss networks we studied in this work.

1.5 Conclusions

The mechanical properties of carbon nanotruss networks in both tensile and compressive regimes were investigated from atomistic simulations by using a reactive potential. Our simulations were performed by stretching various nanotruss configurations along the symmetric orientations [100], [110], [111].

First of all we discussed a method suitable for obtaining realistic structures taking into account the presence of defects. We used the stiffness matrix as a tool to analyze the anisotropy of the samples, finding a small anisotropy due to the nano-structure of our material and the limited box length of the unit cell used during the Voronoi dualization.

Mechanical properties of nanotruss networks are strongly influenced by the presence of defects because these are the points at which cracks nucleate. Nanotruss networks have a brittle nature inherited from the parent material, that is graphene. Furthermore, we found a parabolic trend of the stress-strain curves under tensile load with the tensile strength roughly proportional to the Young modulus. The Young modulus is comparable to that of bulk metals like aluminum.

Our results show the emergence of different responses in compression as a function of orientation and truss geometry. In particular, we have found that the non linear response related to the partial insertion of the nanotubes inside the spheres is screened in the [111] direction. In this case, a suitable choice of the lattice parameters (as done in sample 3) allows a plateau to be obtained in elastic regime. This elastic response is amenable to develop materials that allow the absorption of energy without plastic deformation. Mechanical instabilities were found also along the [100] direction. In this case the mechanical instability has been mainly found for sample 4 showing a strong hysteresis. However, the number of considered cells should strongly influences the number of collapses that occur up to given strain.

A local unstable insertion of the nanotubes in the spheres was found in the [110] direction for a proper choice of the truss geometry. The first type instability influences the mechanical properties, whereas the main effect of the second instability is to deliver a negative Poisson ratio, as found in particular configuration of nanotrusses (samples 3 and 4). Density scaling relations for nanotruss networks

were analyzed assuming a linear or a parabolic relation between relative density and relative Young modulus to estimate the Young modulus of defective graphene that constitutes the nanotruss networks. A range of possible values in accordance with the literature was found.

Finally, energy absorption properties of these carbon nanotrusses have been studied. We found that nanotruss networks could indeed outperform typical materials used as means of energy absorption, such as aluminum foams, high strength steel or bulk aluminum due to an increased specific energy absorption.

Based on the results of this study, nanotruss networks may represent candidates for porous, flexible, and high strength materials. Finally, the novel properties found in carbon nanotruss networks can greatly advance engineering fields, such as impact energy absorption as well as structural mechanics.

1.6   Introduction to Graphene Random Foams

In the first part of this chapter we focused on the design of regular graphene nanofoams. These structures have very good mechanical properties and are promising for high-performance mechanical applications. However, some characteristics such as the anisotropy negative Poisson ratio and the presence of mechanical instabilities, could be not necessary for general pourpose mechanical applications. Graphene random foams (Fig. 1.16 and Fig. 1.17), although less performant that regular ones, can be profitably used for mechanical applications in which the isotropy and a smooth compressive behavior, without instabilities is needed.

In the recent years, an increasing interest was devoted to nanoporous materials. The porosity, indeed, can strongly increase the surface-to-volume ratio as well as mechanical properties such as specific modulus and strength with respect to the bulk material. The surface-to-volume ratio is fundamental for application such as gas adsorption and separation, while the enhanced specific mechanical properties are of interest for lightweight structural components.

Indeed, efforts in synthesizing graphene-based nanofoams have been met with increasing success. Various computational models and simulation techniques were used to investigate their electronic, thermal or mechanical properties [Alonso, 2012, Wu et al., 2013, Pedrielli et al., 2017a]. Graphene foams can inherit the typical
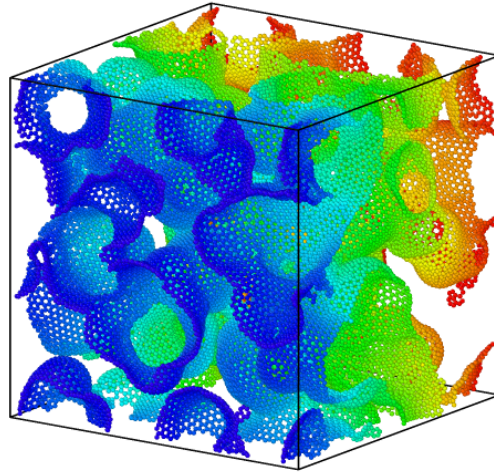
Figure 1.16: *View of a model of a graphene random foam. The cell side is approximately 12 nm. The random foam surface is continuous and divides the space in two separate, while contiguous, subspaces.*

properties of graphene such as mechanical and thermal stability as well as high electronic and thermal conductivity.

Although, for porous materials with pore size of the order of micron the mechanical properties can be effectively described by the classical Ashby-Gibson theory [Ashby, 2006], this approach is not sufficient at the nanoscale where atomic interactions start to play a crucial role.

Furthermore, the intrinsic bidimensionality of graphene produces mechanisms of deformation that are different from those typical at the mesoscale. Indeed, carbon nanoporous materials with random porosity distribution turned out to exhibit a poor scaling of mechanical properties with decreasing density even lower than that of metal and polymeric foams [Qin et al., 2017].

However, at high density graphene foams easily outperform polymeric foams being competitive with high performance materials such as metal foams. Thus, the interest in these random structures remains high.

Here, we contribute to elucidate the mechanical properties of random graphene nanofoams. We present and discuss the results of a series of molecular dynamics (MD) simulations, under tension and compression, performed with a reactive po-
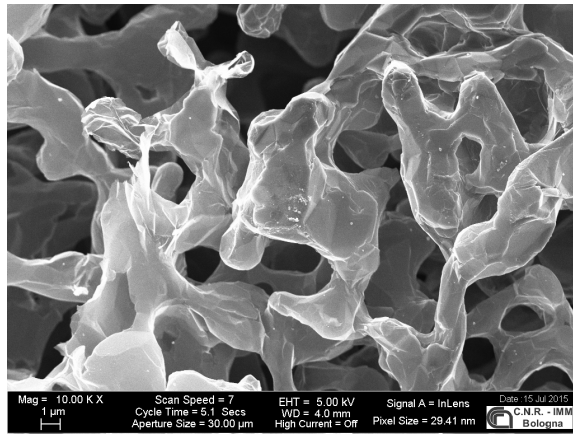
Figure 1.17: *Scanning electron microscopy image of a graphene random foam. Although the pore size is much higher of those of our samples (of the order of some micrometers), the foam topology is very similar. (Courtesy of CNR-IMM Bologna, Italy.)*

tential.

In order to explore the mechanical properties of these kind of random structures we prepared a series of different computational samples with various porosity distribution, with a replicable method. For each group of geometrical parameter we prepared various similar samples, to obtain a small statistical distribution. We prepared 5 samples for each foam family, and we tested them along the three orthogonal directions.

The mechanical properties were assessed by computing stress strain curves under tension and compression as well as Young modulus, Poisson ratio and specific toughness for each family of random foams.

## 1.7   Modeling graphene random foams

To generate families of graphene foams, we use an approach basically composed by two steps [Taioli et al., 2016, Pedrielli et al., 2017a]: first, we entirely tessellate by triangles the surface to be decorated with graphene; second, we apply a Voronoi partitioning (dualization) of the triangulation points.

More in details, we start by filling a given unit cell with a random ensemble
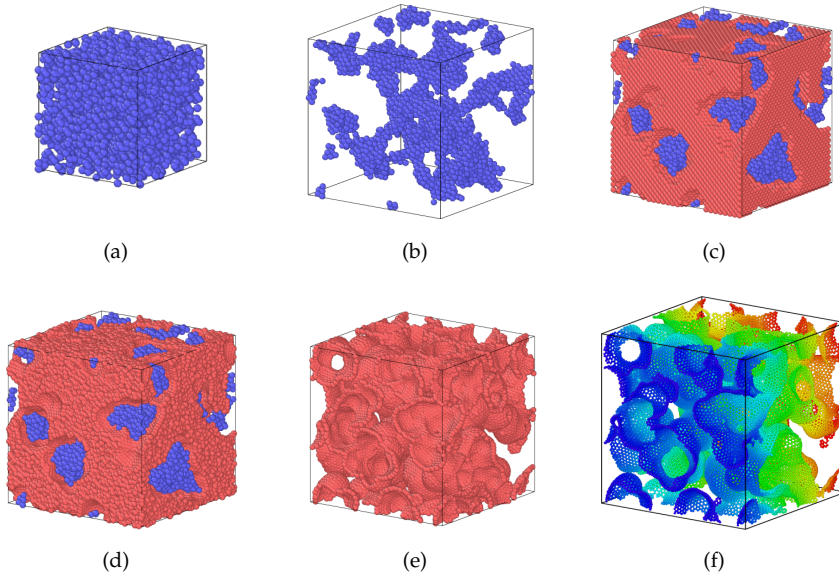
Figure 1.18: *The step sequence for triangulating the foam surface. Panel a) shows the initial condition in which supporting points (S) are randomly arranged in a regular grid. Subsequently, the box is slowly expanded while the supporting particles relaxed (panel b). Triangulating particles (F) are created on a regular grid and deleted if excessively close to the supporting ones (panel c). The position of the points is relaxed and they are attracted towards the supporting particles by means of a molecular dynamics run (panel d). Finally, the triangulating points that do not belong to the first layer are deleted to avoid multilayer structures (e). The LJ net is ready for the Voronoi dualization, where it acquires a graphene-like net (panel f). Colors have been used for visualization purposes only and have no physical meaning.*

of particles (S) interacting via a pair-wise Lennard-Jones (LJ) potential (Fig. 1.18a). As a second step, the unit cell is slowly expanded, imposing a viscous damping force and a NVE integration, to obtain random aggregation of particles (Fig. 1.18b). In the third step we fill the simulation cell with a second type (F) of particles arranged into a regular grid and characterized by different LJ parameters with respect to the previous ones (Fig. 1.18c). The first type of particles acts as a framework to support the particles used in the triangulation (foam particles). The latter are deleted if they are too close (below 0.8 nm) to the support particles in order
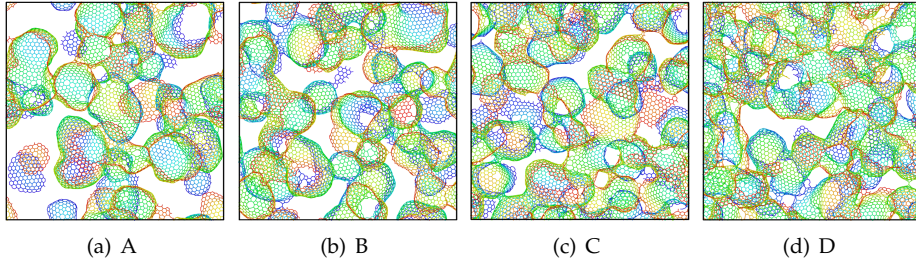
Figure 1.19: *A slice of* 3.0 *nm of a unit cell taken from the four groups of foams with various porosity.*

to avoid convergence issues during molecular dynamics simulations. The fourth step consists in the optimization of the foam particles clamping down the framework degrees of freedom by means of a NVE integration with a viscous damping force Fig. 1.18d. The particles found at a distance from the support particles larger than 0.32 nm were deleted to obtain a smooth mono-layer structure (Fig. 1.18e).

As a last step, the Voronoi partition of the triangles tessellating the surface was performed to obtain pentagonal, hexagonal and heptagonal carbon rings (Fig. 1.18f) (for further details on this procedure see [Taioli et al., 2016]). These configurations were finally annealed by MD using reactive potential to optimize the carbon foams. Four families of carbon foams were produced (A,B,C, and D, see Fig. 1.18a), each characterized by a different initial number of randomly-positioned support particles. Within each family, the only change brought is the initial random distribution of the support points (Fig. 1.18a). During the whole procedure we imposed periodic boundary conditions.

The LJ parameters used for the support (S) and foam (F) particles, respectively, are the following: $\epsilon_{SS} = 100.0$ eV, $\sigma_{SS} = 0.3$ nm, cutoff$_{SS} = 0.5$ nm, $\epsilon_{FF} = 0.1$ eV, $\sigma_{FF} = 0.32$ nm, cutoff$_{FF} = 0.23$ nm, $\epsilon_{SF} = 10.0$ eV, $\sigma_{SFF} = 1.0$ nm. The starting cell side length was 6.0 nm and the expansion up to a cell side length 12.5 nm.

These parameters were chosen in such a way that the typical distance between the support particles was smaller than the equilibrium length between foam and support particles. In this way, the support particle surface is smooth being built by the contribute of several atoms lying nearby.

The topology of the nanofoams studied here is inspired by the graphene foams

Foam type	Average density (g/cm^3)	Atoms with coordination 3 (%)
A	0.55	97.3
B	0.68	95.9
C	0.78	93.0
D	0.83	93.1

**Table 1.7:** *Features that characterize the different foam families.*

grown on nickel scaffolding (Fig. 1.17), which are substantially different from those presented in reference [Qin et al., 2017]. However, we note that the pore size in the experimentally synthesized samples is larger than in our computational models.

1.8   Characterization of graphene foams

Five different samples for each of the four families were prepared by varying the initial distribution of the support particles. In Fig. 1.19 we report representative models (3.0 nm slices) for each of these foam families. From A to D the foams present a decreasing average pore size, and an increasing mass density.

The geometrical analysis of the graphene porous foams and of their voids was carried out using the simulation code Zeo++ [Willems et al., 2012]. In particular, we characterize our prepared structures using first the Pore Size Distribution (PSD) function, which can be experimentally obtained by adsorption/desorption measurements. PSD analysis delivers a quantitative description of the range of pore sizes present in a given sample. We also perform a coordination analysis to find possible signature of under- or over-coordination of the carbon atoms usually forming a network of sp^2 hybrid bonds. The computed quantities are reported in Tab 1.7.

The averaged PSDs for all our graphene foam families are reported in Fig. 1.20 (continuous lines), showing the standard deviation within each group as a colored shaded area. By comparing these PSDs with those obtained in the case of regular pore foams presented in the first part of the chapter, reported in Fig. 1.21, we
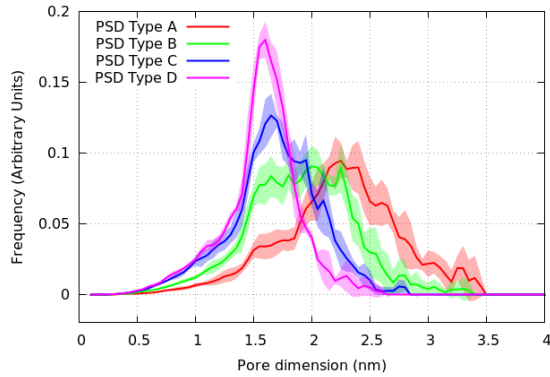
Figure 1.20: *Pore Size Distribution of the four families of random nanofoams. The average pore size of the considered foam families is a decreasing function of mass density.*
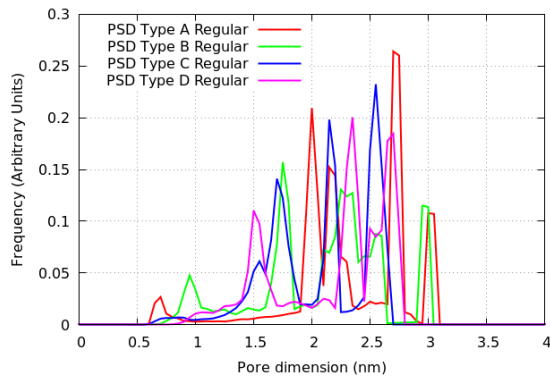
Figure 1.21: *Pore Size Distribution of the four types of regular nanofoams, such as those presented in the first part of this chapter. The average pore size is 2 nm, comparable with the random foam studied here, in particular with foams type B and C reported in Fig. 1.20.*

notice that the random foams present similar average pore dimension and similar mass density. Indeed, the random foam PSDs are characterized by a maximum, representing the most likely pore size in each case, decreasing from 2.3 nm to 1.7 nm from A to D foam type. These values compare reasonably well with those reported for regular foams, where PSD peaks at about 2 nm (see Fig. 1.21). Finally,

while regular foams present mass densities in the range $0.6 - 0.7$ g cm^{-3}, our families of random foams have mass densities in the range $0.5 - 0.8$ g cm^{-3} (see Tab. 1.7).

1.9   Computational methods

The mechanical tests performed in this part of the chapter were essentially the same we performed in the case of regular nanofoams. For details on the procedure and definition of quantities such as deformation, stress and Poisson ratio we refer the reader to those given for regular nanofoams. Here we focus on computational details of thermal conductivity calculation. As in the first part of this chapter, molecular dynamics simulations were carried out using LAMMPS [Plimpton, 1995]. Atomic configurations were visualized by using the OVITO package [Stukowski, 2010] or VMD [Humphrey et al., 1996].

Phonon thermal conductivity was assessed using the equilibrium Green-Kubo approach [Green, 1954, Kubo, 1957] that is less sensitive to the simulation box dimension than non-equilibrium molecular dynamics methods [Sellan et al., 2010]. To this aim, first the atomic positions were relaxed and equilibrated at 300 K using the Berendsen thermostat method (NVT ensemble).

Then, in the NVE ensemble, the equilibrium thermal conductivity k according to the Green-Kubo formalism, can be calculated as follows:

$$k = \frac{V}{3K_{\mathrm{B}}T^2} \int_0^\infty \langle \vec{J}(0) \cdot \vec{J}(t) \rangle dt \tag{1.13}$$

where V is the volume of the simulation cell, t is the correlation time, K_{B} is the Boltzmann constant, $\vec{r}$ identifies the particle positions. The heat current $\vec{J}$, appearing in Eq. 1.13, is defined by:

$$\vec{J} = \frac{1}{V} \left(\sum_i E_i \vec{v}_i + \frac{1}{2} \sum_{i<j} (\vec{F}_{ij} \cdot (\vec{v}_i + \vec{v}_j) \vec{r}_{ij}) \right) \tag{1.14}$$

where $\vec{v}$ is the velocity of a particle, $\vec{r}_{ij}$ and $\vec{F}_{ij}$ are the distance and force between the particles i and j, and E_i is the total energy per atom. The first term in the right hand side corresponds to convection, while the second term to conduc-

tion. The integrand in the expression for thermal conductivity is the heat current auto-correlation function (HCACF). To get a proper sampling of the phase space multiple runs are required with different initial conditions. Simulations to obtain MD trajectories to perform accurate ensemble averages were performed over a time span of 500 ps, using a step of 0.5 fs. HCACF has been computed by dividing the total time of computation into 250 fs beads and by performing the integral in Eq. 1.13 by sampling every 5 fs. Finally, we average over all the beads.

The thermal conductivity was calculated by using a version of the Tersoff potential [Lindsay and Broido, 2010] optimized to reproduce accurately the experimental phonon dispersion curves and the thermal properties of carbon structures, such as graphene and graphite.

1.10 Results and discussion

1.10.1 Tension

The mechanical properties of graphene foams, such as Young modulus, fracture strain and tensile stress, were investigated by computing the stress-strain curves. In Fig. 1.22, we report these curves for the four foam families investigated in this work, while in Fig. 1.23 the stress-strain curves are normalized with respect to the mass density.

The stress-strain curves show a typical elastic behavior for small deformations up to the tensile strength, followed by a decreasing tail corresponding to the sample fracture. We notice that the stress-strain characteristics of graphene foams do not present a region that can be associated to a plastic deformation. Indeed, these 3D graphene structures are essentially brittle, presenting a comparable fracture strain with a stress depends on the foam family.

It is notable that the mass density weighted stress strain curves present the same order and almost the same ratio between tensile strength values than those reported in Fig. 1.22. This due to the fact that the difference in mass density does not justify the difference in mechanical performances for the various foam families but we have to take into account as main cause other foam features such as pore size distribution or connectivity.
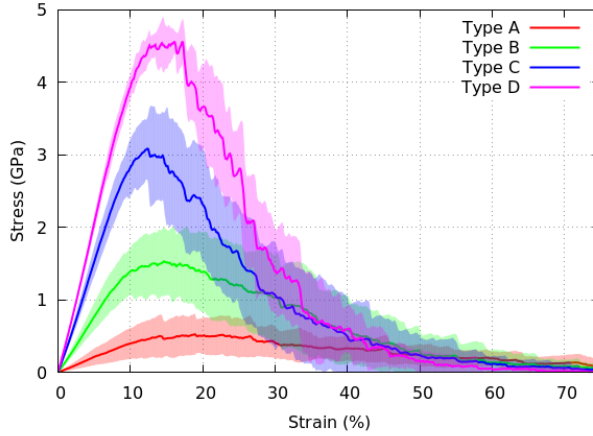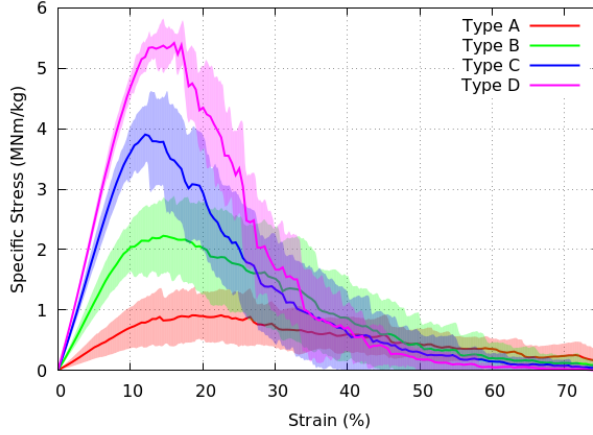
Figure 1.22: *Stress-strain curves of the four graphene foam families under uni-axial tension as well as the standard deviation of each family, reproduced by a colored stripe on the top of the relevant curve.*

In Tab. 1.8 we report the Young modulus and the tensile strength for the four foam families. In Tab. 1.9 are instead reported the specific modulus and the specific strength, which define the values per mass density. Furthermore, in the same table is reported the specific toughness, calculated as the total area under the stress-strain curves up to fracture strain, per mass density.

We compare the values of specific Young modulus and tensile strength with those computed for specific regular carbon nanofoams, also named nanotrusses studied in the first part of this chapter. In that case the values of the stress strain slopes between 5% and 8% strain were in the range $90 - 130$ MNm kg^{-1}. It is clear that the performances regular foams are higher than those of random foams here presented, indeed the specific modulus values reported in Tab. 1.9 are in the range $3.9 - 36.6$ MNm kg^{-1}.

Graphene random foams can be also compared to 3D graphene assemblies reported in reference [Qin et al., 2017]. Graphene assembly present, for 0.366 g/cm^3 mass density, a Young modulus of 2.8 GPa, giving a value for specific Young modulus of 7.65 MNm kg^{-1}, comparable to that of the lower mass density foam family

Figure 1.23: *Stress-strain curves weighted with the sample density of the various families of foam under uni-axial tension as well as the standard deviation within each family.*

| Foam type	Young modulus (GPa)	Tensile strength (GPa)	Fracture strain (%)
A	3.9	0.5	19
B	14.0	1.5	15
C	27.3	3.1	12
D	36.6	4.6	13

Table 1.8: *Young modulus, ultimate strength, and fracture strain of the systems studied under tension.*

studied here (Tab. 1.9). Specific strength $7.4\,\mathrm{MNm\,kg^{-1}}$, given by $2.7\,\mathrm{GPa}$ divided by mass density, of the same graphene assembly is instead higher than that of random foams studied here due to the higher connectivity of the graphene sheets that compose graphene assemblies. However, should be noted that mechanical tests reported in [Qin et al., 2017] were performed at $300\,\mathrm{K}$ temperature whereas the ours at $1\,\mathrm{K}$.

Foam type	Specific modulus ($MNm\,kg^{-1}$)	Specific strength ($MNm\,kg^{-1}$)	Specific toughness ($MJ\,kg^{-1}$)
A	8.3	0.9	0.1
B	25.4	2.2	0.2
C	34.8	3.9	0.3
D	44.0	5.4	0.4

Table 1.9: *Density, specific modulus and specific strength of the four foam families studied under tensile strain. Specific toughness is calculated as the area under the stress-strain curve up to fracture strain per mass density.*

1.10.2 Compression
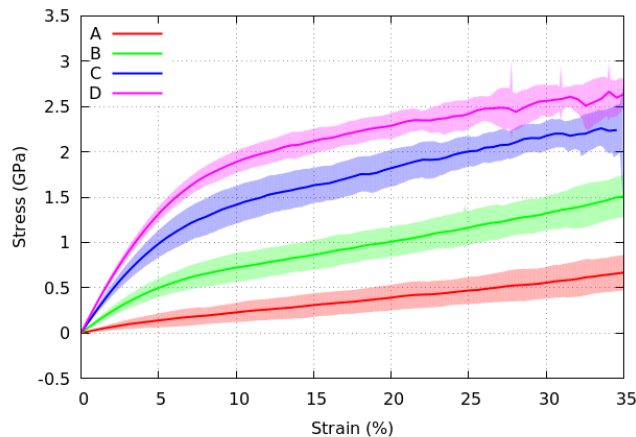
Figure 1.24: *Stress-strain curves of the four random foam types under uni-axial compression up to 35% strain.*

In this section we present the results obtained for the samples under compressive load. In Fig. 1.24 we report the stress-strain curve in compression for the various foam families. The deformation reaches 35% strain for the largest compression. Observing Fig. 1.24, the stress-strain curves at small strain we are in elastic regime, and the material is characterized by a full recovery to the original shape when the load is removed. Subsequently we observe a plateau with a simi-

lar slope for all the foam families, representative of the sample collapse at a nearly constant stress, by buckling or fracture of the building blocks (graphene sheets).

(a) A (b) D
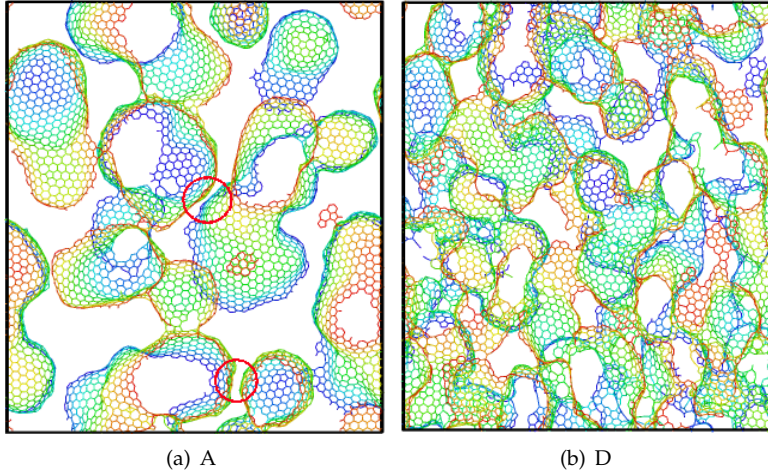
Figure 1.25: *A slice of* 2.0 *nm of a sample taken from the foam families A and D under 12% compressive strain (horizontal direction in the images). As shown in Fig. 1.24 at this strain the foams present the transition between the elastic zone and the collapsing plateau. This transition for higher porosity foams such as those belonging to type A is related to the closure of the interstitial space and the touching of foam graphene sheets, indicated with red circles.*

Finally at higher strain, and not shown, one finds a steep ramp in the stress-strain curve, representing full collapse of the structures. Lower density random foam family, A, presents this ramp at 70% compressive strain, however, higher density foams are not stable under compression up to their final ramp, presenting instead a transition from graphene layers to amorphous carbon, with a strong decreasing of the stress and a subsequent increasing. For this reason, we plotted the compressive stress strain curves only up to 35 %, in this range all the studied sampled are stable.

The main features of the stress strain curves presented in Fig. 1.24 is that with increasing foam density and decreasing pore size average dimension, the slope of the first part of the curves present increases, after $5 - 10\%$ strain the slope of the curves become very similar. This kind of behavior indicates a change in the main
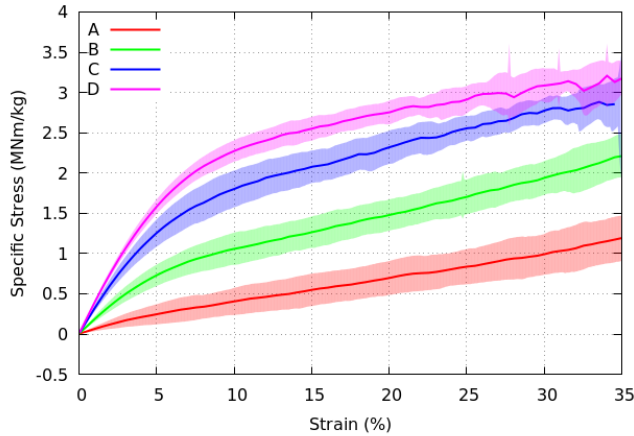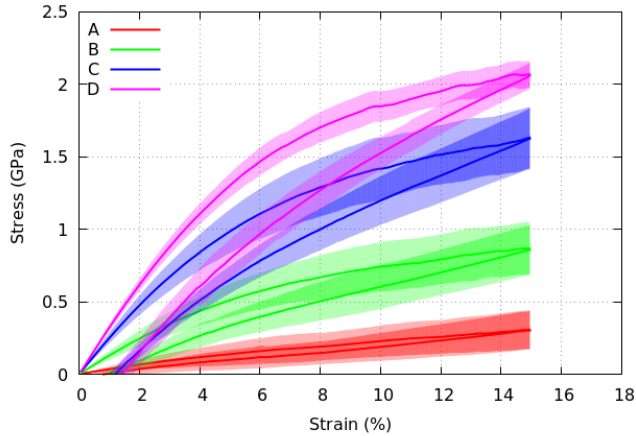
Figure 1.26: *Stress-strain curves of the four random foam types under uni-axial compression up to 35% strain.*

compression mechanism, the small strain slope is due to the structural stability (mainly connectivity between graphene sheets), after $5-10\%$ strain, the structures start to collapse with a relatively small increasing in stress, due to the buckling of the graphene sheets inside the foams.

For foam family with lower mass density the stress strain curves is almost linear, indeed the collapse is dominated by buckling since small strain, for higher density foams the change in slope is evident, showing that the buckling of graphene sheets starts only at higher strain. The similarity of the slope of the stress strain curves between 10% and 30% strain is due to a similar mechanism for collapse.

To elucidate this similar mechanism for collapse in Fig. 1.25 is reported a slice of 2.0 nm of a sample taken from the foam families A and D under 12% compressive strain (horizontal direction in the images). As shown in Fig. 1.24 at this strain the foams present the transition between the elastic zone and the collapsing plateau. This transition for higher porosity foams such as those belonging to type A is related to the closure of the interstitial space and the touching of foam graphene sheets, indicated with red circles.

In Fig. 1.27 are reported the stress-strain curves under compression of the ran-

Figure 1.27: *Stress-strain curves of the four random foam types under uni-axial compression up to* 15% *strain.*

dom four families of random foams. The strain was applied up to 15% loading and unloading the samples. Differently from regular foams that can sustain high deformations (up to 25%) and then fully recover their initial shape when unloaded [Pedrielli et al., 2017a], the higher density of defects in random foams and the local concentration o stress produces a non fully elastic behavior also for relatively small 15% strain.

In Fig. 1.26 are reported the same curves reported in Fig. 1.24 but divided by the nanofoams mass density. Similarly to the tensile case, dividing by the mass density does not significantly change the order or the reciprocal distance between the curves. This makes evident that the difference in performances is more related to the connectivity and topology of the foams than to the mass density.

Furthermore, under compression the behavior of the random foam families with higher density C and D, is very similar to that of regular nanofoams presented in reference [Pedrielli et al., 2017a] with comparable plateau specific stress. Lower density random foams instead, present a more linear behavior under compression that differs from that of regular nanofoams. Young modulus and plateau slope for the four random foam families, studied under compression, are reported

| | Young | Plateau |
| | modulus | slope |
Foam type	(GPa)	(GPa)
A	3.5	1.6
B	12.3	3.0
C	24.4	3.7
D	31.8	3.1

Table 1.10: *Young modulus and plateau stress of the four foam families studied under compression.*
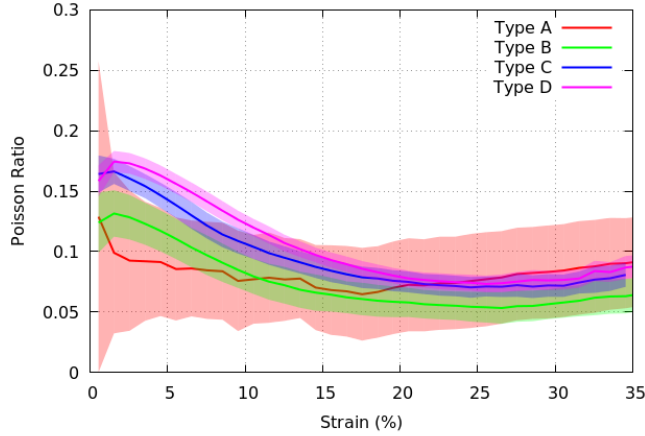
in Tab. 1.10.

1.10.3 Poisson Ratio
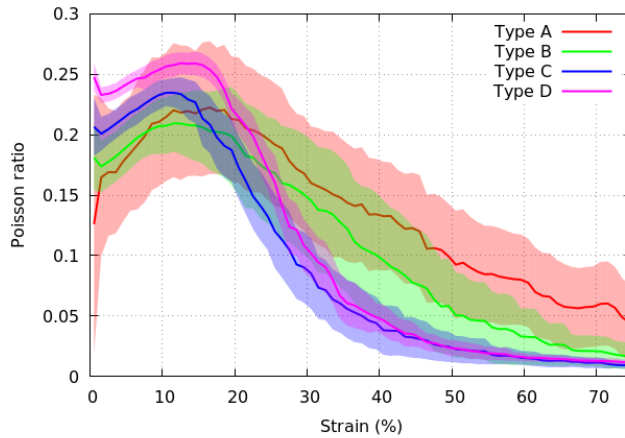
Figure 1.28: *Poisson ratio under tension as function of tension strain of the four random foam types. The shown error area is half standard deviation, for clarity.*

We computed the average Poisson ratio for the four random foam families. We report the results for the extension at high deformation of the Poisson ratio under tension (Fig. 1.28) and compression (Fig. 1.29), with the Poisson ratio for each sample computed as the average in the two direction transverse to the loading. The

51

Figure 1.29: *Poisson ratio under compression as function of compression strain of the four random foam types. The shown error area is half standard deviation, for clarity.*

main features of the graphs in Fig. 1.28 and 1.29 is that Poisson ratio is positive over the whole range of deformations for all random foam families.

Under tension, for near zero strain, the values of Poisson ratio are in the range $0.1 - 0.25$ with values increasing with mass density and foam connectivity. Up to in 15% strain there is a small increment ($0.02 - 0.05$) in the Poisson ratio for all the foams families. For higher strain the values go towards zero due to the fracture of the samples, that decreases the contraction of the samples under tension.

Under compression instead, the decreasing of the Poisson ratio is due to the internal rearrangement of the graphene layers. For higher values of strain considered here, near to 30 % Poisson ratio values become stable in the range ($0.05 - 0.1$).

It can be worth note that the standard deviation for low-density random foam families is significantly higher than that with high-density.

1.10.4 Thermal conductivity

Thermal conductivity was assessed for all the samples averaging within each foam family. We found a as generals trend that the HCACF goes to zero within the first 100 ps and subsequently oscillates. In Fig. 1.30 we reported the values of
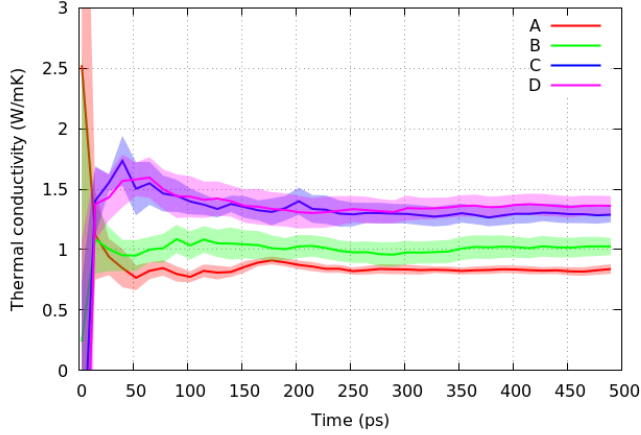
Figure 1.30: *The average integrals of the HCACF of the four random foam types, the values at which they converge for long time is the thermal conductivity. The shown error area is half standard deviation, for clarity.*

Foam type	Thermal conductivity (W/mK)	Standard deviation (W/mK)
A	0.83	0.13
B	1.02	0.20
C	1.29	0.20
D	1.36	0.22

Table 1.11: *Thermal conductivity of the four foam families as computed with Green-Kubo method and optimized Tersoff potential.*

the integrals of the HCACF that are well converged. We report in Tab. 1.11 the values of thermal conductivity obtained for the four foam families, averaging the values in the range $400 - 500$ ps.

The two factors that enter in thermal conductivity are the foam connectivity and the presence of defects. In the foam families studied here these two factors balance each other. Indeed, for lower density foams, the low connectivity is compensated by the higher ratio of triply coordinate atoms, while the opposite happens for higher density foams. The values of thermal conductivity are similar to

those of glass (1 W/mK) for lower density foams, with an small increase of thermal conductivity up to 1.5 W/mK for higher density foams.

1.11 Conclusions

We explored the mechanical properties of graphene random foams with the typical topology of graphene foams grown on stacked nickel nanoparticles, although at a lower scale. In particular, we performed mechanical tests under tension and compression by means of MD simulations with a reactive potential. The computational samples were prepared to present mass density and pore size distribution comparable to those of regular graphene nanofoams presented in the first part of this chapter.

We prepared various samples belonging to four different foam families characterized by different mass density and average pore size, using a consolidated method based on Voronoi partitioning of a triangulated surface. Mechanical properties under tension are characterized by an overall decreasing of Young modulus with respect to regular nanofoams, while a tensile strength of the same order of that of regular foams was found for higher density random foams.

Under compression we found a first elastic deformation with a compressive Young modulus significantly increasing with average pore size dimension decreasing, however a common behavior for all the studied random foam families were found for compressive strain in the buckling plateau zone, with a positive slope of the stress strain curve similar for all the four foam families. For lower density random foam family the stress strain curve is almost linear.

Finally we presented the results for Poisson ratio, used also at high strain as means to explore the transverse response of the deformed materials. Under tension, the Poisson ratio is positive for all the random foam families, indicating a transverse contraction under tensile load. The values of the Poisson ratio under compression is again positive for all the considered strain and tend to stabilize as the strain increases.

Along side the assessing of mechanical properties, we computed the thermal conductivity of random foams, by means of Green-Kubo method and using the optimized Tersoff potential. The thermal conductivity is comparable to that of

glass, and the random foams are not good thermal conductors, these can be related to the low connectivity for high porosity foams and to presence of defects in the low porosity foams.

1.12 Open research lines on regular and random foams

We have seen in this chapter two kinds of graphene nanofoams, regular and random ones. The design of regular graphene nanofoams started from a modification of the hollow octet-truss geometry enhancing it with spherical joints, while random foams were built up with similar average pore distribution of regular ones to compare their mechanical properties. Furthermore, the shape and topology of random foams studied here resembles and the geometry of experimental graphene foams grown by means of chemical vapor deposition on nickel nanoparticle assembly. As one could expect, we found an overall decrease of mechanical performance passing from regular to random carbon nanofoams, as is in general true for porous materials. However, it should be noted that the study of the mechanical properties of graphene foams and their optimization is still at the initial stage. Indeed, a larger number of parameters influence the mechanical properties of graphene foams than standard porous materials such as nanoporous metals. For example, considering graphene foams in which the walls are multi-layer of graphene, we have yet unexplored mechanism of deformation, strongly different from those present in nanoporous gold. For both regular and random nanofoams computer simulations are a promising instrument of screening and design. We indicate here three possible research lines to expand this works. The first could be the evaluation of the mechanical properties of a large number of different nanofoams, charachterizing them by means of various descriptors for example PSD, connectivity, average curvature. To evaluate how much these descriptors are related to the mechanical properties could be very useful. The second research line could be the extrapolation of scaling relations such as the variation of the Young modulus or tensile strength with the mass density. This is not so simple, again due to the fact that graphene foams are in general composed by multilayers graphene sheets. In this regard, it is important *how* the mass density is changed. The third research line could be the study of the origin of the instabilities found

for regular nanofoams under dynamic loads.

Chapter 2

# Gas Adsorption and Dynamics in Pillared Graphene Frameworks

2.1 Introduction

In this chapter we focus on the assessment of gas adsorption properties of graphene-based 3D structures that fully exploit the high surface-to-volume ratio of graphene. The assessment of these properties can be performed with accuracy in the framework of MD and Grand Canonical Monte Carlo (GCMC) simulations.

In order to exploit graphene for gas adsorption and mechanical applications, many different kinds of 3D carbon-based structures were proposed in the past years, such as carbon nanotube networks [Ding et al., 2007], carbon nanoscrolls [Mpourmpakis et al., 2007, Coluci et al., 2007] and graphene foams [Alonso, 2012, Pedrielli et al., 2017a]. At the same time, a growing interest was devoted to materials in which graphene is enhanced by chemical functionalization or the addition of external components such as organic molecules [Tang et al., 2013]. In this last category, Pillared Graphene Frameworks (PGF) are a novel class of materials,
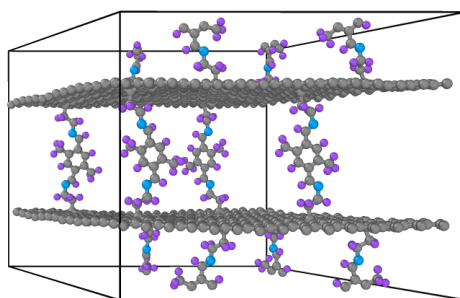
Figure 2.1: *Prospective view of an hexagonal unit cell of a Pillared Graphene Framework. The pillars are constituted by organic molecules covalently bonded to graphene layers. Carbon atoms are rendered in grey, hydrogen in violet and nitrogen in blue.*
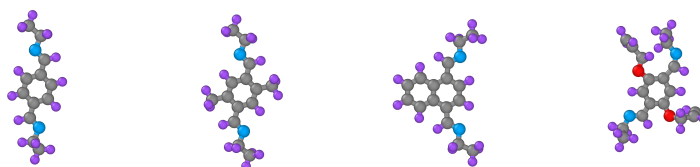
(a) Pillar type 1 (b) Pillar type 2 (c) Pillar type 3 (d) Pillar type 4

Figure 2.2: *The four nitrogen-containing organic pillars considered in this work. Carbon atoms are rendered in grey, hydrogen in violet, nitrogen in blue and oxygen in red.*

composed by stacked graphene layers separated by organic moieties.

Analogously to Pillared Graphene-Oxide Frameworks (PGOF) [Srinivas et al., 2011, Kumar et al., 2014], the properties of PGFs can be varied by changing the kind and the density of organic spacers hence obtaining a fine tuning of gas absorption and gas separation performances. Similarly to other materials for gas adsorption such as Metal Organic Frameworks (MOFs) [Duren et al., 2004, Babarao et al., 2007, Duren et al., 2009, Colon and Snurr, 2014], Zeolitic Imidazolate Frameworks (ZIFs) [Battisti et al., 2011, Zhang et al., 2013] and PGOFs [Burress et al., 2010, Garberoglio et al., 2015], the gas adsorption and separation performances of PGFs can be fruitfully studied by means of computer simulations [Wang et al., 2014].

However, gas adsorption and separation in PGFs are still largely unexplored. In this work, we investigate these properties for a class of structures in which the spacers are nitrogen-containing organic molecules using Grand Canonical Monte Carlo (GCMC) and Molecular Dynamics (MD) simulations. The principal goal of this chapter is to investigate the role of pillar type and pillar density in determining the performance of PGFs for gas adsorption. In particular, we will investigate whether the quantity of gas adsorbed or the selectivity can be optimized by varying the type and the density of pillars. In fact, one could expect adsorption to increase with the number of pillars at small pillar density (due to the presence of more adsorption sites), whereas adsorption at high pillar density could be prevented by progressive lack of available volume. Consequently, there might be a specific pillar density optimizing gas uptake.

Furthermore, the influence of pillar density and type on gas separation performances will be assessed. The gas separation performance for a gas mixture depends in general on two main factors: first the preferential adsorption of a gas with respect to another, namely the gas selectivity, second the difference in the diffusion coefficient of the two species. To estimate the gas separation performances of PGFs we will compute the gas selectivity for different mixtures as well as the diffusion coefficients for single component gases.

In computing the diffusion coefficients and assessing the dynamical properties of the adsorbed gases the flexibility of the adsorbent can strongly influence the simulation results, as shown for other materials [Battisti et al., 2011, Zhang et al., 2014]. Due to the high mobility of the structures considered in this work, we took into account structural flexibility in all dynamical simulations.

2.2   Computer model

Pillared Graphene Frameworks are composed by stacked graphene layers separated by organic spacers. Here we investigate a narrow class of these structures with four types of nitrogen-containing organic spacers. For each type of organic spacer we generated several computational samples with various pillar density, between 0.09 and 1.71 pillars nm^{-2}. We report in Fig. 2.1 a sketch of an entire sample. In Fig. 2.2, the four types of organic pillars considered in this work are

shown.

Although these structures have not yet been synthesized, they are likely to be realized in the nearest future. Furthermore, the four types of pillar chosen here are representative of different shape, symmetry, rigidity and steric volume. Additionally, they present the same length so that the contribution to adsorption given by the graphene layers' distance does not change, allowing a better comparison of the pillar performance.

Pillar Type	Pillar Density (nm^{-2})	Free Volume (%)	Mass Density (g cm^{-3})
1	0.09	77.1	0.443
	0.68	67.9	0.555
	1.37	57.1	0.687
2	0.09	76.5	0.450
	0.68	65.8	0.569
	1.37	52.7	0.721
3	0.09	74.5	0.490
	0.68	65.5	0.585
	1.37	51.0	0.755
4	0.09	71.0	0.560
	0.68	55.5	0.731
	1.37	38.9	0.942

Table 2.1: *Free volume and mass density for the samples with pillar type 1 to 4 and with representative pillar density. The free volume is defined in Eq. (2.1).*

In generating computational supercells, we prepared a hexagonal unit cell with periodic boundary conditions containing two graphene layers with base vectors $a = b = 3.684$ nm intercalated by the organic molecules, in such a way that the pillars were alternated in their anchorage to successive graphene planes (see Fig. 2.1). The length of the third base vector c, perpendicular to the graphene planes, was set to accommodate the pillars, approximately 3 nm for all the pillar types. Free volume and mass density for the samples with pillar type 1 to 4 and with representative pillar density are reported in Tab. 2.1.

To conclude the preparation of the samples, we equilibrated them using the LAMMPS program [Plimpton, 1995] by means of 50 ps isothermal-isobaric Molec-
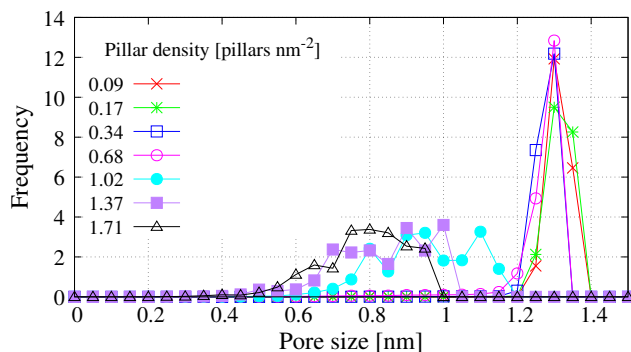
Figure 2.3: *Pore Distribution Function for pillar type 1 and various pillar densities.*

ular Dynamics simulations at room conditions, using the ReaxFF potential [van Duin et al., 2001, Chenoweth et al., 2008] with parameters suitable for organic molecules and carbon-based materials [Mattsson et al., 2010]. For each sample, we saved one equilibrated configuration of atomic coordinates to be used in the subsequent studies. Furthermore, we saved the point charges that were self-consistently calculated during the ReaxFF simulation (QEq method [Nakano, 1997, Rappé and Goddard, 1991]), and we used these point charges in all the simulations in which Coulomb interaction had to be taken into account. The thermal stability of these structures was tested by means of molecular dynamics simulations with ReaxFF potential. The structures considered in this work are stable 300 K. Some preliminary tests at higher temperature (higher than 700 K) have shown that the thermal stability of PGFs is strongly dependent form the pillar density.

After samples' relaxation, we computed two descriptors that are useful to characterize porous materials: Pore Size Distribution (PSD) and Accessible Surface Area (ASA). The computations were performed by means of the code Zeo++ [Willems et al., 2012] using the default values for atomic radii and 0.1 nm radius for the sampling sphere. The pore size distribution (PSD) is the statistical distribution of the radius of the largest sphere that can be fitted in points uniformly sampled within the pores of the material.

As an example, we report in Fig. 2.3 the PSD for pillar type 1. In this plot, the PSD curves are shown for various pillar densities. The radius of the most probable
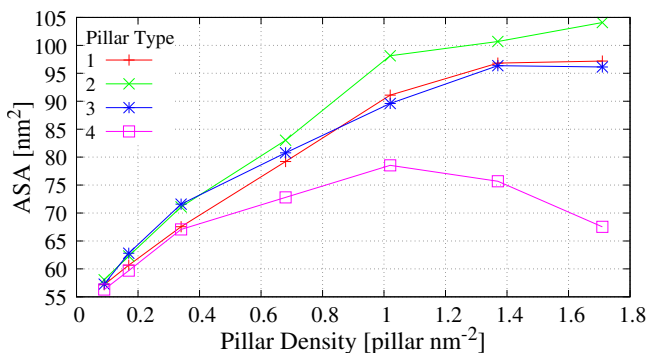
Figure 2.4: *Accessible Surface Area (ASA) as function of pillar density for various pillar types.*

pore decreases for increasing pillar density. At lower densities the main peak is around $1.2 - 1.4$ nm ($0.8 - 1.2$ nm for pillar type 4), whereas for higher densities the peak is less intense and shifted towards 0.8 nm (0.6 nm for pillar type 4). In the limit of low pressure, smaller pores can in general store more fluid than bigger ones, due to the favorable interaction of the fluid with the pore wall.

In Fig. 2.4 we report the ASA as function of the pillar density, for various pillar types. The ASA is an increasing function of the pillar density, with the exception of pillar type 4. In this case, the ASA presents a maximum for intermediate pillar density and a decrease for higher pillar densities. Visual inspection of the atomic configurations shows that in this last case the pillars are tightly packed, with relative distances of the order of the size of the atoms.

To investigate gas adsorption and separation in these materials we used the Grand Canonical Monte Carlo Method. For a detailed description of the method see Ref. [Battisti et al., 2011]. In GCMC, as well as in Molecular Dynamics simulations, it is necessary to choose a model for both the gas-gas and the gas-adsorbent interaction. Here we described the molecules as either spherical particles or rigid linear rotors interacting via Lennard-Jones sites and point charges. In particular, we used the EPM2 potential for CO_2 [Harris and Yung, 1995], and the potential validated by Murthy for N_2 [Murthy et al., 1980] and by Zhang [Zhang and Siepmann, 2006] for O_2. In the case of CH_4 and H_2 we used a single-site Lennard-

Jones potential, with the parameters validated by Buch [Buch, 1994] and Goodbody [Goodbody et al., 1991], respectively. The pure-fluid phase diagram is well described by these models.

The commonly used DREIDING [Mayo et al., 1990] force field, augmented with the ReaxFF framework charges, was used to describe the gas-adsorbent interaction. Another popular choice is the UFF force field [Rappe et al., 1992], which we considered for some cases. Analogously to other studies appeared in the literature, we also found that UFF generally results in higher adsorption quantities than DREIDING [Garberoglio et al., 2005, Sumida et al., 2012, Getman et al., 2012]. The cutoff of the long range van der Waals and Coulomb gas-adsorbent interactions was set to 1.6 nm.

Framework flexibility is known to have strong effects on molecular transport in materials with small window sizes or soft components whereas in rigid structures with large pores it has minor effects [Amirjalayer et al., 2007, Haldoupis et al., 2010, Hertag et al., 2011, Pantatosaki et al., 2012]. For the materials considered in this work the pore size as well as the structural rigidity is dependent on the pillar density so that the mobility of the adsorbent during the gas diffusion simulations has to be taken into account. Hence, we used the bonded part of the UFF force field to describe framework flexibility, keeping the DREIDING parameters to describe long-range dispersive interactions. Recent calculations have shown that UFF is very efficient yet capable to describe a broad range of microporous materials with reasonable accuracy [Garberoglio and Taioli, 2012]. Indeed, in some preliminary tests, we found that if the framework is kept rigid the underestimation of the diffusion coefficient can be up to 40% lower, when high pillar density structures are considered. In both GCMC and MD simulations the Lorentz–Berthelot mixing rules were used to calculate the long range van der Waals interaction between unlike atoms.

For all the simulations presented in this chapter, the length of production run was such that the number of successful insertions were at least five times the average number of adsorbed molecules. This condition is generally deemed sufficient to assert the reliability of GCMC simulations.

2.3 Results and Discussion

2.3.1 Pure-fluid isotherms

Pure fluid isotherms were computed for H_2, CH_4, CO_2, N_2 and O_2 gases. The van der Waals equation of state was used to relate the chemical potential to the pressure of the reservoir gas using parameters set to reproduce the position of the adsorbate critical point [Hirschfelder and Curtiss, 1954]. For each external pressure we performed 5×10^5 equilibration steps (one step being an insertion, a deletion, or a translation/rotation of an already adsorbed molecule, all performed with equal probabilities), followed by 1 million production steps.
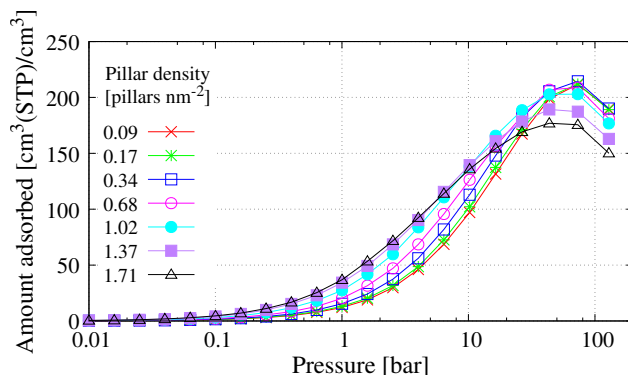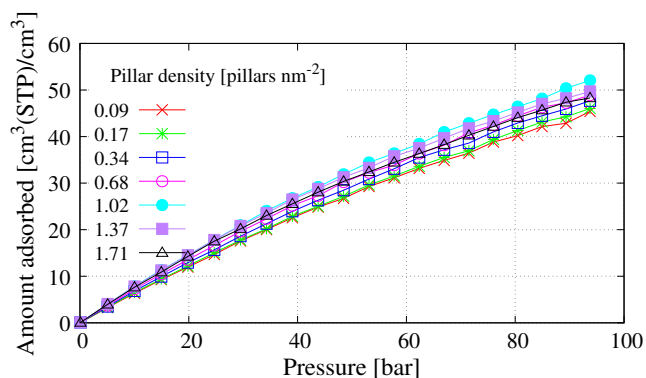

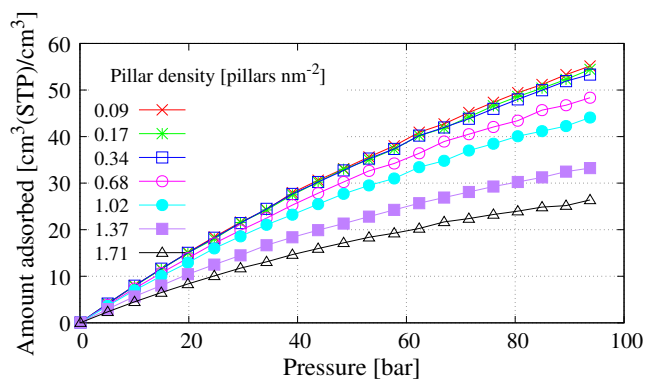**Figure 2.5:** *Volumetric adsorption isotherms of CH_4 at T= 298 K for pillar type* 1.

In particular, we computed the excess amount, N_{ex}, that can be obtained by estimating the number density $\rho(T, P)$ of the adsorbate at the given thermodynamic condition (calculated using the van der Waals equation of state) and the available free volume for the adsorption V_{free} [Hirschfelder and Curtiss, 1954]. The free volume is conventionally defined as the volume of the region where the solid-gas interaction between the framework and a helium atom divided by the Boltzmann constant k_B is less than 10^4 K. The excess number of adsorbed molecules is then defined as

$$N_{ex} = N - \rho(T, P) \, V_{free}, \tag{2.1}$$

where N is the total number of gas molecules.

Figure 2.6: *Volumetric adsorption isotherms of H_2 at T= 298 K for pillar type 1. The best uptake is obtained for an intermediate pillar density of 1.02 pillars nm $^{-2}$.*
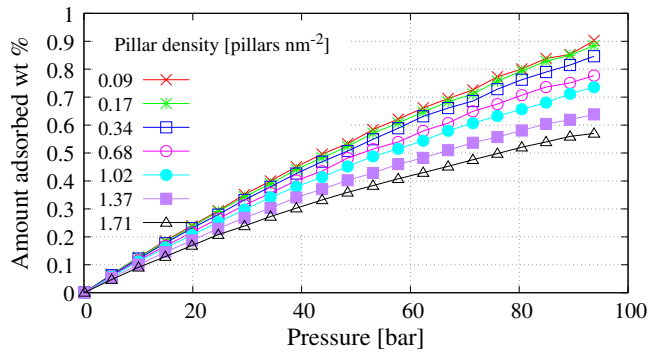

Figure 2.7: *Volumetric adsorption isotherms of H_2 at T= 298 K for pillar type 4. As the pillar density decreases the adsorption uptake increases.*

It is in general useful to define two kinds of isotherm curves. The first one is the volumetric isotherm which is given by the ratio between the volume occupied by the adsorbed gas at standard pressure and temperature, and the geometric cell volume. This measure of adsorption indicates how much the presence of the adsorbent can concentrate within the adsorbate with respect to room conditions. The second kind is the gravimetric isotherm and is given by the percent ratio between the weight of the adsorbed gas and the sum of the weights of the framework and
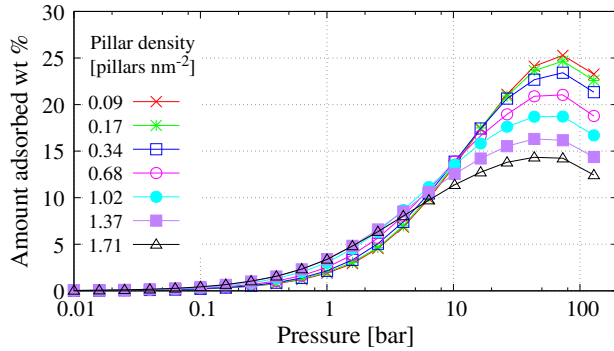
Figure 2.8: *Gravimetric adsorption isotherms of CH_4 at T= 298 K for pillar type* 1*. At high pressure, near the saturation limit, we found a clear performance decrease as pillar density increases, the contrary happens at low pressure.*

Figure 2.9: *Gravimetric adsorption isotherms of H_2 at T= 298 K for pillar type* 1*. As the pillar density decreases the adsorption uptake increases. The saturation is not reached within* 100 *bar.*

the adsorbed gas. This quantity is of practical interest for fuel storage, especially for automotive applications where the weight of the system is of particular concern.

For all the gases (H_2, CH_4, CO_2, N_2, and O_2), adsorption isotherms were computed at 298 K. In the case of H_2 we also considered $T = 77$ K. In what follows, we

will focus mainly on isotherms for the pillar type 1, because we generally found minor differences as a function of the pillar type.

Some features of these isotherms are common to almost all the cases investigated in this chapter. Referring to the volumetric adsorption isotherm of CH_4 at 298 K reported in Fig. 2.5, one notices that at low pressures (roughly below 10 bar) the quantity of gas adsorbed increases up to two times with increasing pillar density. Indeed, visual inspection of the GCMC configurations shows that in this regime gas is mostly adsorbed close to the framework atoms and a larger number of pillars provides more adsorption sites. This trend was found for all gases execpt H_2 at 298 K, independently of the pillar type.

Conversely, for larger pressures, the amount of gas adsorbed is a decreasing function of the density of pillars. In this regime, the gas is also adsorbed in the volume between the pillars, but the volume available for adsorption decreases with increasing pillar density due to steric hindrance. Because the maximum volumetric uptake was found for the samples with lower pillar density, the maximum uptake is in general independent of pillar type. In fact, for high pressure, the maximum uptake is essentially limited by the total free volume, that decreases as the pillar density increases. A similar trend was observed for H_2 at 77 K in an experimental investigation of a closely related material, which used graphene-oxide instead of pure graphene [Kumar et al., 2014].

The volumetric adsorption isotherms of H_2, reported in Fig. 2.6, do not follow this general picture. First of all, even at the highest pressure investigated here (100 bar) there is no sign of reaching saturation.

However, despite being in the "low-pressure regime", the dependence of the amount adsorbed with respect to the pillar density does not follow the trend observed in the case of the other gases, for one sees that there is an optimal pillar density (around 1 nm^{-2}) that optimizes adsorption, although volumetric uptake is similar (within 20%) for all the considered pillar density. The same optimal pillar density was found for PGFs with pillar type 2 and 3. In the case of samples with pillar type 4, reported in Fig. 2.7, this optimal pillar density is not present and we found the uptake being a decreasing function of pillar density. This kind of behavior is related to the high pillar volume of the pillar of type 4, resulting in the lack of free volume also for low pillar density samples.

Gravimetric gas adsorption isotherms at $T = 298$ K for the various structures containing pillars of type 1 and different pillar density are shown in Fig. 2.8 and 2.9 in the case of CH_4 and H_2, respectively. In the case of CH_4 the isotherms display the same qualitative behavior observed in the volumetric case: adsorption increases with pillar density for low pressures, and decreases at higher ones. However, in this case the normalization with the total mass of the system enhances the difference in adsorption at high pressures, while diminishing it in the low-pressure regime.

For H_2 gravimetric isotherms, reported in Fig. 2.9 at 298 K we found, as usual, a linear trend up to 100 bar, so that saturation is not reached. Analogously to methane, when the adsorption per unit mass is considered, higher-density adsorbents are penalized, and in this case the best performance is observed in the lighter structure, independently from the pillar type.

Among the gases considered in this work CH_4, CO_2 and H_2 are those of major technological interest. We summarize in Tab. 2.2 and 2.3 the maximum values of gravimetric and volumetric uptake found for these gases at 1, 10 and 35 bar, indicating at which pillar type and pillar density corresponds the maximum uptake.

In the case of CH_4 we found a maximum volumetric uptake at 35 bar of 195 cm^3(STP)/cm^3, with similar performances for different pillar types. This value is comparable with what is observed in MOFs, where methane uptake at the same pressure range is ≈ 230 cm^3(STP)/cm^3 for the best performer [Mason et al., 2014]. The performance of the well-known MOF-5 (IRMOF-1) at the same conditions is ≈ 150 cm^3(STP)/cm^3.

The amount of CO_2 adsorbed in PGFs is also comparable to what is found in other microporous materials, such as MOFs where gravimetric adsorptions in the range 30–74.2% are reported at room temperature and pressures up to 50 bar [Sumida et al., 2012]. The maximum uptake of CO_2 the PGFs examined is reported in Tab. 2.3 and can be up to 58.9% at 35 bar in the case of pillar type 3 at the lowest pillar density.

With regards to H_2 we found a maximum value of ≈ 25 cm^3(STP)/cm^3 for volumetric uptake at 35 bar (Tab. 2.2) comparable with that of small pore structures such as ZIF-9 and MOF-5 [Garberoglio et al., 2005, Battisti et al., 2011]. The value for gravimetric maximum uptake of 0.4% at 35 bar, reported in Tab. 2.3 is slightly

higher than that of MOF-5 and very similar to that of IRMOF-14 [Garberoglio et al., 2005].

2.3.2 Comparison between DREIDING and UFF force fields

As already mentioned, the two force fields that are mostly used to estimate dispersion interactions between adsorbed gases and microporous organic materials are DREIDING and UFF, the latter generally resulting in a higher uptake. In order to compare the results obtained by these two force fields in PGFs, we computed

$$R(P) = \frac{N_{\text{ex(UFF)}}(P) - N_{\text{ex(DREIDING)}}(P)}{N_{\text{ex(DREIDING)}}(P)}, \qquad (2.2)$$

where $N_{\text{ex(UFF)}}$ and $N_{\text{ex(DREIDING)}}$ are the excess number of adsorbed molecules at pressure P obtained using UFF force field and DREIDING, respectively. This quantity measures how much adsorption depends on the choice between these two force fields, and is expected to be positive on the basis of the evidence published in literature [Garberoglio et al., 2005, Getman et al., 2012, Sumida et al., 2012].

The values of $R(P)$ in the case of adsorption of CH_4 at 298 K temperature for all the pillar types and three different pillar density are reported in Fig. 2.10, where one can immediately see that also in the case of PGFs UFF predicts a larger amount of gas adsorbed than DREIDING. The various curves present some clear trends. In particular, $R(P)$ is a decreasing function of the external pressure, reaching values less than 20% at saturation, and an increasing function of pillar density. This is particularly evident at low pressures ($\lesssim 10$ bar), where UFF predicts up to twice as much adsorbed amount than DREIDING. In fact, in the low-pressure regime adsorption is mainly determined by the gas-framework interaction, so that the differences between the force fields are emphasized. Conversely, the interaction between gas molecules plays a greater role under saturation conditions (high pressures) and hence the difference due to the two force fields become less important. A similar behavior is observed for CO_2 at 298 K and H_2 at 77 K.

In the case of H_2 at 298 K instead (Fig. 2.11), $R(P)$ is essentially constant over the whole pressure range, maintaining the dependence on the pillar type and the

	1 bar			10 bar			35 bar		
	uptake (cm^3(STP)/cm^3)	T	D (nm^{-2})	uptake (cm^3(STP)/cm^3)	T	D (nm^{-2})	uptake (cm^3(STP)/cm^3)	T	D (nm^{-2})
CH_4	43.6	2	1.71	147	4	0.34	195	1	1.02
CO_2	114	2	1.71	341	4	0.09	360	3	0.09
H_2	0.81	2	0.09	8.03	2	0.09	24.6	2	0.09

Table 2.2: *Maximum values of volumetric uptake (cm^3(STP)/cm^3) found for CH_4, CO_2 and H_2 at 1, 10 and 35 bar. For each pressure in the last two columns are indicated the pillar type (T) and pillar density (D) producing the maximum uptake.*

70

|	1 bar			10 bar			35 bar		
	uptake (wt%)	T	D (nm^{-2})	uptake (wt%)	T	D (nm^{-2})	uptake (wt%)	T	D (nm^{-2})
CH$_4$	3.76	2	1.37	15.2	4	0.09	22.3	3	0.09
CO$_2$	22.3	3	1.37	53.5	3	0.09	58.9	3	0.09
H$_2$	0.013	3	0.09	0.13	3	0.09	0.40	1	0.09

Table 2.3: *Maximum values of gravimetric uptake found for CH$_4$, CO$_2$ and H$_2$ at 1, 10 and 35 bar. For each pressure in the last two columns are indicated the pillar type (T) and pillar density (D) producing the maximum uptake.*
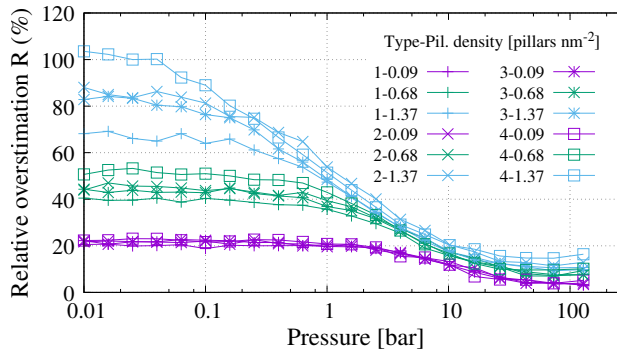

Figure 2.10: *Relative overestimation R of CH$_4$ adsorption at 298 K using UFF force field in place of DREIDING force field.*

pillar density found for the previous cases. This can be explained by the fact that the saturation regime is not reached for H$_2$ at 298 K, hence the decrease of $R(P)$ at high pressure that is observed in the other gases does not appear in this case.

To investigate in more detail the origin of the observed differences between these two force fields, we computed zero-coverage isosteric heat $Q_{st}^{(0)}$ in both cases. The results for CH$_4$, CO$_2$, and H$_2$ are reported in Fig. 2.12 for the PGF with pillar 4. The difference between the values obtained for the two force fields, of the order of 10%, does not justify the magnitude of the relative overestimation $R(P)$ in zero-pressure limit, which can be up to 100%, as reported in Fig. 2.10. This discrepancy can be explained by the fact that the isosteric heat is not the only quantity contributing to adsorption. In fact, the uptake is also proportional to the amount

71
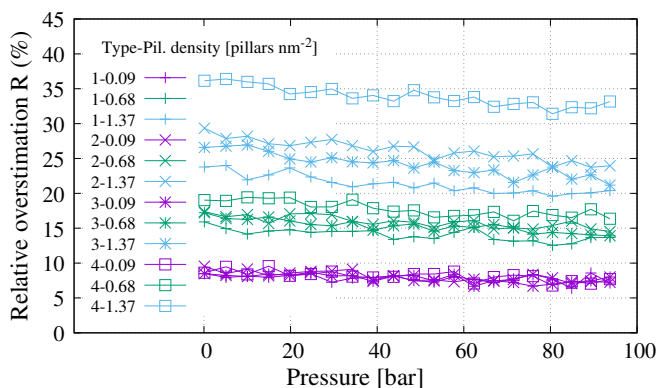
Figure 2.11: *Relative overestimation R of H$_2$ adsorption at 298 K using UFF force field in place of DREIDING force field.*
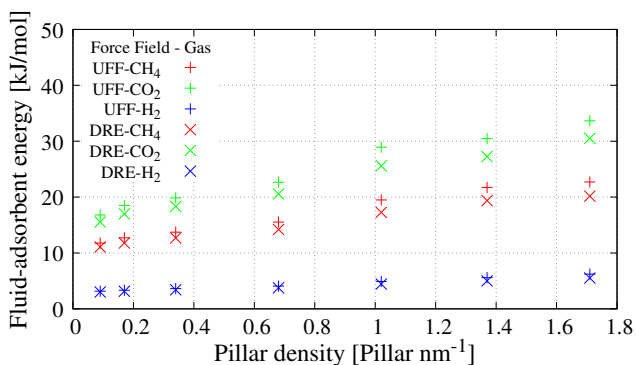
Figure 2.12: *Zero-coverage isosteric heat $Q_{st}^{(0)}$ for the two different force fields. The results are reported for CH$_4$, CO$_2$, and H$_2$ for the PGF with pillar 4.*

of volume in the cell where the solid-fluid interaction is favorable. This can be quantified by computing the Volume Density of States (VDOS), $D(E)$, which is defined so that $D(E)dE$ is the volume of space available to an adsorbate molecule at adsorption energies between E and $E + dE$. The VDOS can be computed as the probability that random points have energy less than E times the volume of the cell.

In Fig. 2.13 we report the VDOS of CH$_4$ for the PGF with pillar 4 at the high-
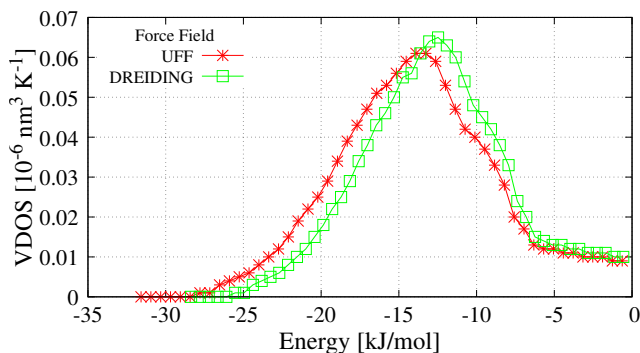
Figure 2.13: *VDOS for the PGF with pillar 4 and the highest pillar density, for CH4.*
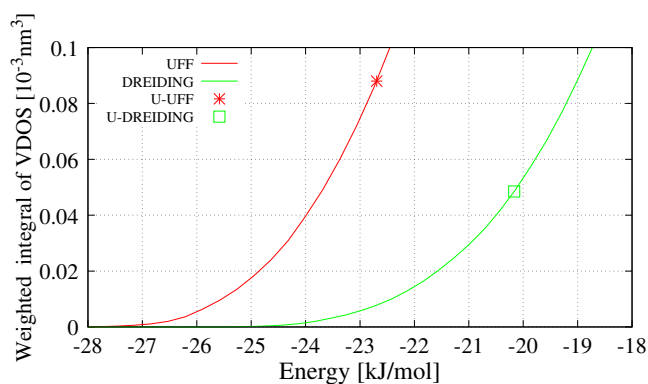
Figure 2.14: *Boltzmann weighted integral of VDOS at 300K for CH_4 with UFF and DREIDING force field for PGF with pillar type 4 and highest pillar density.*

est pillar density. The integral of the VDOS weighted with the Boltzmann factor up to the observed value of $Q_{\text{st}}^{(0)}$ is proportional to the amount of gas adsorbed at low pressures. We report this integral in Fig. 2.14 where we evidence the value obtained using $Q_{\text{st}}^{(0)}$ as the upper limit. In the case of the UFF force field, this quantity turns out to be almost twice as that obtained using DREIDING. In summary, both $Q_{\text{st}}^{(0)}$ and the VDOS have to be taken into account to explain the difference in the adsorption between different force fields.

The question of which force field is more suitable to describe adsorption in

PGFs can be answered experimentally by performing gas adsorption measurements in the low-pressure regime where the differences between UFF and DREIDING are more pronounced.

2.3.3 Mixture adsorption and selectivity

Type	1			4		
Density (nm^{-2})	0.09	0.68	1.37	0.09	0.68	1.37
CO_2/H_2	26.2	51.4	117.6	35.8	90.2	340.0
CH_4/H_2	9.6	16.2	31.7	12.7	24.6	66.6
CO_2/CH_4	2.7	3.2	3.7	2.8	3.7	5.1
CO_2/N_2	6.3	9.1	14.0	7.1	12.3	27.1
N_2/O_2	1.00	1.02	1.04	1.01	1.02	1.01

Table 2.4: *Zero-pressure adsorption selectivity in the Pillared Graphene Frameworks with pillar types 1 and 4 for different pillar density.*

We investigated the adsorption selectivity of the structures with pillar types 1 and 4 in the case of the following binary mixtures: CH_4/H_2, CO_2/H_2, CO_2/CH_4, N_2/O_2, CO_2/N_2. We chose to focus on pillar types 1 and 4 that represent the two extrema as pillar complexity and pillar volume: type-1 pillar is linear and not charged, whereas type-4 pillar has protruding charged moieties (see Fig. 2.2).

The selectivity of an adsorbent for a mixture of gases is defined by the ratio

$$S(b/a) = \frac{x_b/x_a}{y_b/y_a},\qquad (2.3)$$

where x_a, x_b denote the molar fractions of the adsorbed species a and b while y_a and y_b denote the molar fractions of the reservoir bulk mixture. In the low-pressure limit the selectivity is independent of the molar composition of the bulk gas. In this case, it can be computed as the ratio of the single-particle partition function of the two species in the adsorbed phase, divided by the ratio of the free-particle partition function of the same two species [Tan and Gubbins, 1992, Challa et al., 2002, Battisti et al., 2011]. We denote with S_0 the low-pressure limit of the selectivity.

Values of S_0 are report in Tab. 2.4 for the pillar densities of 0.09, 0.68 and 1.37 pillars nm^{-2}, corresponding to the smallest, the intermediate and the higher values investigated in this work. S_0 is in general dependent on the considered mixture, the pillar density and the pillar type. Our results show that the variation in pillar density has the greatest influence, changing the selectivity up to a factor of almost ten. Conversely, changing the pillar type results usually in a more modest variation of the selectivity, in the range of 50%.

The zero-pressure selectivity increases with the pillar density for all mixtures, except N_2/O_2 for which it is almost constant. The values of the selectivities for these mixtures are generally comparable to the values reported for other microporous materials, such as MOFs [Garberoglio et al., 2005, Sumida et al., 2012] or ZIFs [Banerjee et al., 2009, Battisti et al., 2011, Prakash et al., 2013].

In general, adsorption selectivities in excess of 100 are considered fairly high. In the case of the strucures investigated here, this is observed for the CO_2/H_2 mixture, especially at high pillar densities where we have $S_0(CO_2/H_2) \sim 340$. This value is higher than the one found in ZIFs (~ 275 [Battisti et al., 2011]) and also in MOFs, where it reaches the value ~ 100 in CuBTC and ~ 12 in MOF-5 [Yang and Zhong, 2006].

The selectivity is in general a function of many factors, such as, for example, bulk composition of the mixture and the external pressure. In the following, we will focus on the dependence of the selectivity with respect to external pressure. In order to minimize the statistical error in the computed selectivities, the amount of molecules of both species within the simulation box should be of the same order. To this end, the bulk mole fraction of specie b in a bulk mixture (b, a) was fixed to the value $1/(1 + S_0)$ where where S_0 is the zero-pressure limit of the selectivity $S(b/a)$ [Battisti et al., 2011]. We note that although the selectivity does depend on the value of the mole fraction, it does not generally vary dramatically [Bae et al., 2008], hence we expect our results to be valid in a wide range of conditions.

We report in Fig. 2.15 and 2.16 the pressure dependence of $S(b/a)/S_0$ for the samples with pillar type 1 and 4, respectively, with a density of 0.68 pillars nm^{-2}. As shown in Fig. 2.15 and 2.16 all the mixture selectivities are essentially constant up to 1 bar keeping their low-pressure value. Beyond a few bars we find different trends depending on the mixture: the selectivity can either increase, remain

almost constant, or decrease at large pressures with a variation of roughly a factor of two.

The origin of this behavior, which has also been observed in ZIFs [Battisti et al., 2011] can be rationalized using energetic and entropic arguments. For molecules of the same type – e.g. both single Lennard-Jones centers such as CH_4/H_2 or linear rigid rotors such as CO_2/N_2, or N_2/O_2 – the variation in the selectivity is related to the energetic gain upon adsorption at finite pressure. In general, CO_2 is the molecule whose single-particle energy increases the most when the adsorbed density increases. This in turn enhances the probability of another carbon dioxide molecule being adsorbed with respect to its competing species, resulting in an increasing value of the CO_2 selectivity. This is what happens for the CO_2/N_2 and CO_2/CH_4 mixtures: in both cases the energy gain upon adsorption of a carbon dioxide molecule at the highest pressure is ~ 200 K larger than for the adsorption of the other one. This argument applies also in the case of N_2/O_2, where adsorption of an oxygen molecule results in roughly a 25 K gain in energy with respect to the adsorption of a nitrogen one. As a consequence, the selectivity decreses at higher pressures.

However, this picture seems to be in contrast with what is observed in the case of the CO_2/H_2 mixture, whose selectivity shows only a modest increase at the highest pressure despite the fact that CO_2 adsorption is favored by ~ 100 K gain in energy. In this case one should also take into account the fact that upon adsorption, especially in packed geometries, a carbon dioxide molecule can become rotationally hindered. This loss of entropy balances the gain of energy, resulting in a modest 20% gain in selectivity at high pressures. To check this we performed calculations at the lowest and highest pillar densities: in the former case the CO_2/H_2 selectivity increases by up to 50%, in the latter it remains constant (within the uncertainties of the calculation).

2.3.4 Dynamics of adsorbed molecules and permeation selectivity

The simulation of gas dynamics was performed using MD simulations within LAMMPS code [Plimpton, 1995]. The framework topologies to be used in LAMMPS
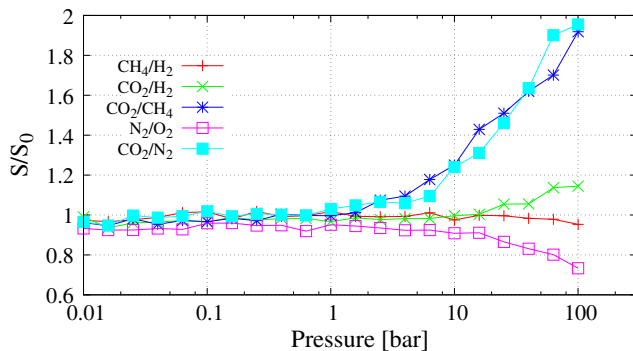
Figure 2.15: *Selectivity for gas mixtures at T= 298 K, normalized with respect to the zero-pressure limit value of selectivity (S_0), for the sample with pillar type 1 and pillar density* 0.68 *pillars nm* $^{-2}$.
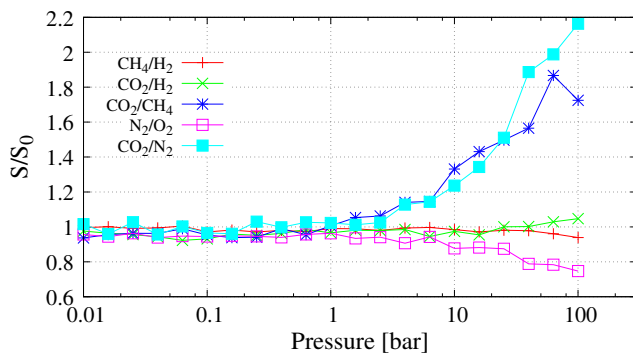
Figure 2.16: *Selectivity for gas mixtures at T= 298 K, normalized with respect to the zero-pressure limit value of selectivity (S_0), for the sample with pillar type 4 and pillar density* 0.68 *pillars nm* $^{-2}$.

code were generated according to the bonded part of UFF using a modified version of OBGMX [Garberoglio, 2012]. We started from representative configuration of pure gas adsorption at two different pressures for which the adsorption uptake was maximum and half maximum. For H_2 at 298 K we take as maximum the 100 bar point.

The isothermal simulations started with a 500 ps equilibration at T = 298 K driven by a Nosé–Hoover thermostat with a time constant $\tau = 1$ ps. The x, y and z components of the mean-squared displacement were computed and averaged over 10 consecutive 500 ps MD trajectories, in which the thermostat coupling time was reduced to $\tau = 50$ ps.

The diffusion coefficients were calculated by means of a weighted least square fit of 100 ps separated points of the averaged mean-squared displacement curve. Indeed the diffusion coefficient can be computed from the mean-squared displacement curve as

$$D_x = \lim_{t \to +\infty} \frac{1}{2} \frac{d\Delta x^2(t)}{dt},$$ (2.4)

with an analogous definition for the y and z directions. Due to the fact that all the samples present no gas diffusion in the direction perpendicular to the graphene planes, the overall diffusion coefficient can be assessed as the average between the x and the y directions,

$$D = \frac{1}{2}(D_x + D_y).$$ (2.5)

As a first test, we checked the effect of framework flexibility on the values of the self-diffusion coefficient in Eq. (2.5), considering the case of CH_4 and CO_2 moving in PGFs with pillar density 0.09 and 1.37 pillars nm^{-2}, pillar type 1 and 4, at maximum and half maximum gravimetric uptake. We found a relative difference in D between mobile and fixed framework of $5 - 15$ % and $30 - 40$ % for pillar density 0.09 and 1.374 pillars nm^{-2}, respectively. Given these results, we decided to use a flexible model of the framework in the calculation of self-diffusion.

The results for diffusion coefficient for pillar types number 1 and 4 with pillar density 0.09, 0.68 and 1.37 pillars nm^{-2} are reported in Tab. 2.5. The general trend is a decrease of the self-diffusion coefficient with increasing pillar density.

Furthermore, H_2 is the gas with higher diffusion values followed by CH_4, N_2 and O_2 with similar values, and finally CO_2 with the lower diffusion coefficients. This sorting is largely independent of the pillar type or density.

The diffusion coefficients reported in Tab. 2.5 are all higher than 10^{-9} m^2 s^{-1}, the order of magnitude of self-diffusion coefficient in liquid such as H_2O, so that none of the considered structures inhibits gas diffusion. However, for pillar density higher than 1.37 pillars nm^{-2}, the gas diffusion could be hindered. Differently

Type		1			4		
Density (nm^{-2})		0.09	0.68	1.37	0.09	0.68	1.37
CH_4	H	30.3	12.9	3.32	35.9	7.84	0.617
	M	14.3	6.96	2.34	10.6	4.09	0.538
CO_2	H	4.04	2.85	1.27	9.56	1.60	0.270
	M	0.941	0.696	0.360	0.825	1.34	0.113
H_2	H	219	74.3	23.6	170	38.4	4.07
	M	129	49.5	20.0	105	27.8	2.79
N_2	H	23.3	10.6	4.55	15.4	5.26	0.870
	M	6.30	3.69	1.89	4.53	2.22	0.531
O_2	H	28.5	11.7	5.48	23.1	5.88	1.13
	M	8.49	4.27	2.67	5.97	2.81	0.58

Table 2.5: *Diffusion coefficients (in units of 10^{-8} m^2 s^{-1}) for the Pillared Graphene Frameworks with pillar types 1 and 4 for different pillar density at half maximum (H) and maximum (M) gravimetric uptake.*

from ZIFs and MOFs, in which the structures with small windows connecting the pores, such ase, for example, ZIF-5 and ZIF-9 [Battisti et al., 2011], can easily inhibit the gas diffusion, in PGFs the diffusion is not hindered even at high pillar density because the pore are constituted by the free volume between mobile moieties and there are no definite windows to be crossed.

Type	1			4		
Density (nm^{-2})	0.09	0.68	1.37	0.09	0.68	1.37
CO_2/H_2	0.48	1.97	6.30	2.01	3.76	22.6
CH_4/H_2	1.33	2.83	4.46	2.68	5.02	10.1
CO_2/CH_4	0.36	0.70	1.41	0.75	0.75	2.23
CO_2/N_2	1.09	2.44	3.89	4.38	3.75	8.39
N_2/O_2	0.81	0.92	0.87	0.67	0.91	0.78

Table 2.6: *Separation performance factor $\Sigma = \Sigma_0 \Pi$ for the Pillared Graphene Frameworks with pillar types 1 and 4 for different pillar density.*

The overall performance of PGFs for gas separation is determined by a tradeoff between high adsorption selectivity (which is enhanced by high pillar densities,

see Tab. 2.4) and molecular transport (which is hindered by high pillar densities, see Tab. 2.5). A quantity taking into account these two opposite trends is the so called permeance selectivity Σ which is defined as the product

$$\Sigma = \Sigma_0 \Pi, \qquad (2.6)$$

where Σ_0 is the low-pressure selectivity and Π is the ratio between the self-diffusion coefficients of the two gases [Krishna and van Baten, 2007, Liu and Johnson, 2009, Battisti et al., 2011].

The results for separation performance factor for pillar types number 1 and 4 with pillar density 0.09, 0.68 and 1.37 pillars nm^{-2} are reported in Tab. 2.6. To compute the separation performance factor the diffusion coefficients at half maximum of gravimetric uptake were used.

As general trend the separation performance factor for a given mixture increases as the pillar density increases. We found good performances for the high pillar density samples for CO_2/H_2 and CH_4/H_2 with maximum values of 22.6 and 10.1, respectively. These values are significantly larger than the ones found in the analysis of gas separation in ZIFs [Battisti et al., 2011] where values of 3.42 and 1.42 where observed. Inspection of the values of S_0 and Π show that the origin of the higher performance of PGFs is mainly due to their larger value of S_0, since the ratio of the diffusion coefficient leading to Π is roughly the same for PGFs and ZIFs.

A value of $\Sigma = 8.39$ was also found for CO_2/N_2 separation. For this mixture, ZIFs were found to have a maximum value $\Sigma = 10.4$, in the case of ZIF-4 [Battisti et al., 2011]. For this particular mixture, PGFs have a slightly less performing separation behavior, despite having a larger value of S_0 (27.1 versus 8.2) due to the fact that the self-diffusion coefficient of N_2 is three times higher than that of CO_2 in PGFs. In the case of ZIF-4, the value of Π turns out to be ~ 1 [Battisti et al., 2011].

2.4 Conclusions

In this chapter we presented an extensive analysis of gas adsorption and separation for nitrogen-containing Pillared Graphene Frameworks using computer simulations. In particular, we focused on the influence of the pillar type and the pillar density on the performance for gas storage and separation. We took into account the quadrupole moment of CO_2, H_2 and O_2 molecules. Furthermore, we used the self consistent point charges extracted by ReaxFF simulations to model the Coulomb interactions between the gases and the frameworks.

Our results show that the density of pillars has a greater influence on adsorption than the pillar type. Under saturation conditions, the increase of pillar density results in a sensible decrease of the amount of gas adsorbed. Despite this shortcoming, the absolute value of the amount adsorbed is comparable to what is observed in organic frameworks (MOFs, ZIFs or COFs), although it falls short to achieving the performance of the best of them.

In the case of adsorption selectivity, we found that one can have a lot of control on the performance by varying both the pillar type and density. The actual range of variability, though, depends on the specific mixture under consideration. In the case of CO_2/H_2, the ratio between the maximum and minimum adsorption selectivity at zero-pressure (see Tab. 2.4) is more than factor of ten. Conversely, the selectivity of the N_2/O_2 mixture is always close to one, irrespectively on the nature of the pillar considered or its density. However, selectivity is in general an increasing function of the pillar density.

When dynamical properties are considered, the effect of pillar density is very pronounced. In general we found roughly an inverse proportionality between the pillar density and the self-diffusion coefficient. This finding paves the way to the possibility of tailoring transport properties to a high degree of precision, possibly up to the ballistic regime. However, there might be issues of stability of the Pillared Graphene Structure at very low pillar densities that will have to be addressed.

Finally, when the overall separation performance Σ – which includes both adsorption and diffusion – is considered, PGFs show quite a good performance when compared with other microporous materials, especially in the case of the

CO_2/H_2 and CH_4/H_2 mixtures.

## 2.5   Open research lines on Pillared Graphene Frameworks

In this chapter we have seen how hybrid structure such as PGFs result to be promising for gas adsorption and separation. However, some issues can arise in pratical application, for example automotive gas storage, or when we use these structures under high temperature or stress conditions. In this prospective, some further studies can be carried on. In particular, the evaluation of mechanical and thermal stability of PGFs under high temperature and/or loads, could drive the design of new generation of nanostructured materials in which, for example, the organic pillars do not have a structural function. A way could use as spacers both organic pillar and carbon nanotubes, allowing in this way not only increasing of the mechanical properties but also the gas diffusion in direction perpendicular to the graphene layers. Furthermore, some fine details could be assessed, for example variation of the gas adsorption when the mobility of the framework is included.

Modeling and X-ray spectra calculation for SiC/SiO$_x$ core/shell nanowire

3.1 Introduction

In this chapter we focus on the modeling and X-ray spectra calculation for SiC/SiO$_x$ core/shell nanowires, that play a fundamental role in a new promising method for cancer treatment. Recently [Tatti et al., 2017] proposed a method in which hybrid nanosystems comprised of X-ray absorbing nanostructures (SiC/SiO$_x$ core/shell nanowire) and light-sensitive material (porphyrin) are used for the singlet oxygen production (Fig. 3.1). This approach allows overcoming the limitations of visible light penetration in matter, the major limitation for the use of light-sensitive materials in singlet oxygen production. Indeed, coupling porphyrin with SiC/SiO$_x$ core/shell nanowires allows to fully exploit the penetration power of X-rays and the local action of light-sensitive materials. The singlet oxygen is an excited state of molecular oxygen that can be generated via energy transfer from a photosensitizer. The aim of the work reported in this chapter is to propose and

validate a realistic model for SiC/SiO$_x$ core/shell nanowires, that allows the simulation of X-ray absorption near edge structure (XANES) spectra. This is the first step in the simulation and optimization of this cancer treatments, that relies on an accurate study of the underling physical mechanisms.
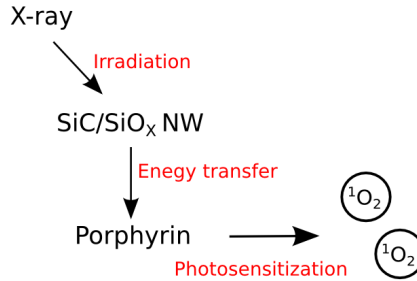
Figure 3.1: *The processes involved in the method for cancer treatment reported in Ref. [Tatti et al., 2017]. The porphyrin functionalized SiC/SiO$_x$ core/shell NW is irradiated by X-rays, the energy is mainly absorbed by the NW, the energy transfer from the NW to the porphyrin allows the singlet oxygen production.*

From the point of view of the SiC/SiO$_x$ core/shell nanowires (NWs) modeling, the current literature only partially addresses the problems encountered in the development of a SiC/SiO$_x$ nanowire computational model. In particular, a reliable and validated model for calculations of XANES spectra has not been yet proposed. The state of the art of the SiC/SiO$_x$ modeling is limited to that of the different components taken separately, or to different geometries such as slabs, nanodots or nanocrystals. Some studies report on interface models between a SiC slab and SiO$_x$ exploring its electronic properties [Li et al., 2015], some others focus on the identification of the defects at the interface of SiC/SiO$_x$ core/shell nanodots [Vörös et al., 2012], other studies focus only on SiC nanowires [Liu et al., 2010, Laref et al., 2014].

Furthermore, some studies on the band gap of SiC/SiO$_2$ nanodots due to their dimension and terminations were done only recently [Dong et al., 2013]. Liu et al. [Liu et al., 2010] report simulations and experiment of XANES spectra of bulk SiC and SiC nanowires. However, a full atomistic model of SiC/SiO$_x$ core/shell nanowires, capable of reproducing the experimental XANES spectra is

still lacking. The strong influence of sp^2 carbon defects in the absorption spectra of SiC/SiO$_x$ core/shell nanowires has been stressed by Liu et al. [Liu et al., 2010] from an evaluation of the peaks of the experimental XANES spectra.

Also in this case, a study of the influence of the accidental and/or technically unavoidable carbon contaminants on the XANES spectra, from the computational side, in a realistic SiC/SiO$_x$ core/shell nanowire model, has not yet been presented in literature.

Here, we present a step-by-step development of a realistic model of a single SiC/SiO$_x$ core/shell nanowire, and compare the theoretical XANES spectra with the experimental ones. The synergic characterization of SiC/SiO$_x$ core/shell nanowires, from a computational and experimental point of view, gives a comprehensive overview of the main features of these structures and paves the way towards the modeling and the optimization of the full porphyrin-based method for cancer therapy.

3.2 Experimental details on XANES spectra acquisition

The growth SiC/SiO$_x$ core/shell NWs and the acquisition of the experimental XANES spectra were performed by the group of M. V. Nardi (CNR section of Trento, Italy) without any contribution from the author of the present thesis, a brief overview is reported here only for sake of completeness.

The SiC/SiO$_x$ core/shell NWs were grown via a low-cost carbothermal method, based on the reaction between carbon monoxide and the native oxide on (001) Si substrates, using iron oxide as a catalyst [Fabbri et al., 2010]. The typical core/shell structure of a single NW presents a core NW radius of 10 nm and a shell thickness of 20 nm. To study the SiC NWs without shell, the SiO$_x$ was fully removed from the as-grown NWs by etching the substrates in hydrofluoric acid (HF). XANES spectra were collected at ELETTRA facility in Trieste, from as-grown SiC/SiO$_x$ core/shell and HF-etched SiC NW ensembles that were maintained on the planar substrates. The spectra have been collected in total electron yield (TEY) mode (i.e., drain current mode) at the energy corresponding to the C and O and Si K-

edge, respectively, and normalized to the incident photon flux. The synchrotron beam was elliptically polarized. Throughout the measurements, the incident angle of light with respect to the sample surface plane has been kept fixed at $54.7°$. The XANES spectra at the Si K-edge (TEY) of as-grown and HF-etched SiC/SiO_x core/shell NWs were recorded at the Spherical Grating Monochromator (SGM) beamline of the Canadian Light Source (Canada).

To correctly process the acquired data, each absorption spectrum has been first normalized to the drain current. The energy scale of each single spectrum has been re-calibrated taking into account the energy fluctuations of characteristic absorption features measured on the refocusing mirror.

3.3 Modeling SiC/SiO_x core/shell nanowire

The model we present here was strongly driven by the aim of use it to calculate and compare theoretical XANES spectra with the experimental ones. In first place we focused on the SiC core nanowires. The aim was to compute the band gap for different terminations and different NW diameters. We prepared three samples with radii 0.6, 0.9 and 1.3 nm and the main axis of the nanowires the along the [111] crystal direction. We obtained a cell with a periodicity along the main axis of the nanowire (z axis) of 0.75309 nm. The three samples are represented in Fig. 3.2.
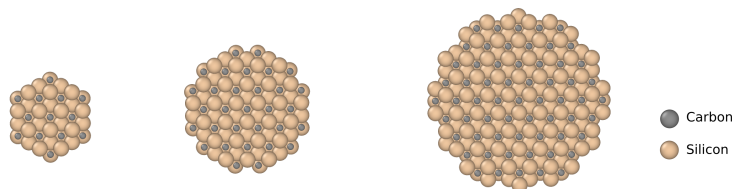
Figure 3.2: *xy-section of the three SiC core NWs as relaxed with SCC-DFTB calculation. The NW radii are 0.6, 0.9 and 1.3 nm respectively.*

The obtained structures were relaxed according to the Self-Consistent Charge Density Functional Tight Binding (SCC-DFTB) geometry optimization routines of

the DFTB+ code [Aradi et al., 2007]. We used the parameter set *matsci-0-3* [J. Fren-zel, 2009] for a proper treatment of the d states of silicon atoms, which is funda-mental for realistic band gap and band structure calculations.

As reported in the literature [Vörös et al., 2010, Beke et al., 2016], the elec-tronic properties of such nanosystems crucially depends not only on the quantum confinement effect, which turns SiC from an indirect into a direct band-gap semi-conductor, but also on the nanosystem surface terminations, which give rise to surface-related states that cannot be neglected at the nanoscale.

In this work, we studied the electronic structures of the SiC core nanowires by saturating the surface dangling bonds of C and Si atoms with hydroxyl $-$OH groups or with $-$H atoms. While $-$H termination is the usual way to saturate dangling bonds, the motivation of the $-$OH termination is that it better resembles the surface of experimental SiC/SiO$_x$ core/shell nanowire when the SiO$_x$ shell is etched by means of hydrofluoric acid (HF). In this case indeed, a thin layer of silicon oxycarbides [Fabbri et al., 2010] that is chemically inert against HF etching remains as protective layer on the SiC core. We report the values of the band gap as a function of the nanowire radius and surface termination in Tab. 3.1. With regard to the $-$H termination NWs, the band gap is a monotonically decreasing function of the NW radius. Conversely, when the $-$OH termination is considered the band gap present a minimum due to the competitive influence of quantum confinement and surface effects. In the following, for convenience, we will build up the SiC/SiO$_x$ core/shell nanowire model using the NW with diameter 0.6 nm. However, the band gap calculation help us to evaluate the influence of this choice on the spectra calculations, and suggests that to obtain a sample with a band gap resembling that of experimental sample (core diameter 20 nm) the model should be created using a large SiC core NW, with a consequent considerable increase in computational cost.

The second part of our modeling work was to add a SiO$_x$ shell to the SiC core NW. For computational reasons, we start studying and coating the small-est model SiC NW, i.e. the one with 0.6 nm radius. The SiC+SiO$_x$ NWs were built starting from the SiC core NWs. Their geometric structures were modeled in LAMMPS [Plimpton, 1995] package using molecular dynamics simulations with

	Band Gap (eV)	
Radius (nm)	$-H$ sat.	$-OH$ sat.
0.6	3.31	2.16
0.9	2.79	1.68
1.3	2.52	2.03

Table 3.1: *Band gap trend for SiC core nanowire terminated with $-OH$ radicals and $-H$ atoms.*

a reactive potential (ReaxFF [Chenoweth et al., 2008]). The parametrization we used [Kulkarni et al., 2013] is tailored to reproduce structures composed by Si-C-O atoms, and we verify that allows to reproduces realistic silica and silicon carbide structures. In some preliminary test we found that within an approach based only on molecular dynamics simulations the production of a suitable model for SiC+SiO$_x$ NWs is very difficult to obtain. Indeed, on one hand classical potentials allows to reproduce the typical structure of SiO$_2$, on the other hand the small dimensions of the core, the necessity of a relatively small periodicity along the axis of the nanowire and a proper description of the interface between the core and the shell are constraint too stringent for a molecular dynamics approach. In particular, the main problem is related to the interface modeling that needs to drive a decreasing of bond density from the SiC core to the SiO$_2$ shell. The superficial density of bonds at the surface is indeed much higher that that of silica shell and an approach based only on molecular dynamics result to be insufficient to obtain this reduction of bond density. The modeling of SiC/SiO$_2$ is largely treated in literature manly for SiC slabs (see for example [Devynck and Pasquarello, 2007]). To overcome the problems found in modeling the interface, we chose a hybrid approach, in which we manually decreased the bond density by factor three. As shown in Fig. 3.3 we saturated the SiC core surface bonds, for example those indicated with a, b and c, with oxygen atoms (indicated with 1, 2 and 3), then a silicon (4) atom was located in such a way that forms three bonds with them. Finally new oxygen (5) was attached to the silicon.

Once the interface was prepared, we added the silica shell by means of molecular dynamics. In particular we defined a square cell with 3 nm of side length around the core with the interfacial atoms imposing periodic boundary along the three dimensions (Fig. 3.4). Then a given number of non-overlapping silicon and
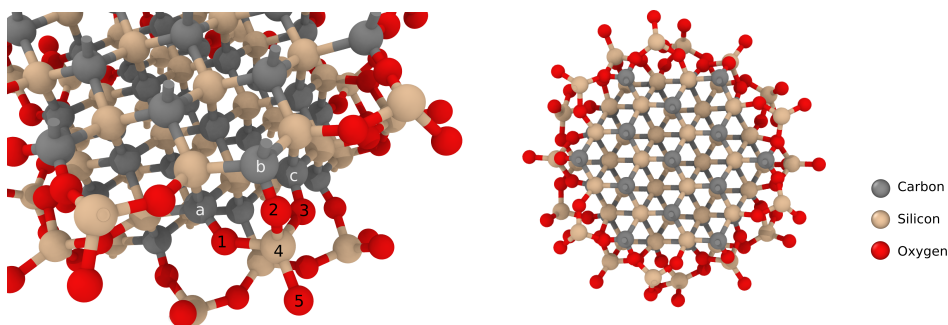
Figure 3.3: *Interfacial bond density reduction. Left panel: Our strategy to reduce the SiC core surface bonds to that of silica shell can be divided in three steps. First, we saturate all the surface bonds (for example those of atoms indicated with a, and c) with oxygen atoms (indicated with 1,2,3). Second, a Silicon atom (indicated with 4) was located in such a way that forms three bonds with oxygens. Finally a new oxygen was attached to the silicon (5). Right panel: a section view of the NW core with the interfacial bonds.*

oxygen atoms in a 1:2 stoichiometric ratio were introduced in the simulation box to reach a density of ca. $2.20\,\mathrm{g/cm^3}$. The wire and the interfacial atoms were taken frozen while an annealing of the outer shell was performed at 4000 K for 100 ps, subsequently the temperature was decreased to 10.0 K in another 100 ps (using 1 fs timestep). As last step, the core wire was released and the structure minimized.

The NW model was obtained deleting all the atoms distant from the core center more then the desired radius of the SiC+SiO$_x$ NW. All the dangling bonds were saturated with hydrogen atoms (Fig. 3.5).
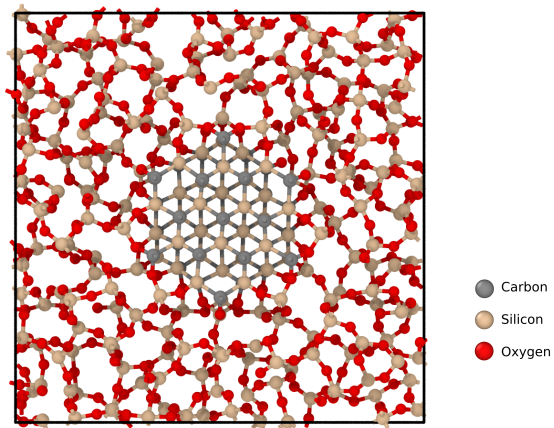
Figure 3.4: *Cell used to add the silica shell on the SiC core. A number of non-overlapping silicon and oxygen atoms was inserted in the simulation cell in order to obtain $a \sim 2.20\ g/cm^3$ mass density. The $SiC+SiO_x$ NWs unit cell was then cut out with a proper choice of shell thickness.*
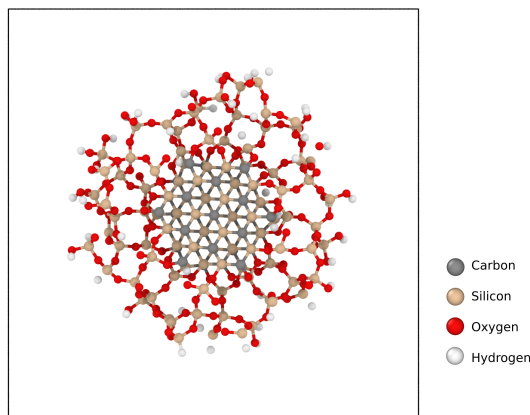
Figure 3.5: *$SiC+SiO_x$ NW final model. The free bonds were saturated with hydrogen atoms.*

3.4 Spectra calculation method

XANES spectra were computed in single-particle approximation within XSpectra [Gougoussis et al., 2009] suit of QUANTUM ESPRESSO [Giannozzi et al., 2009] code. XSpectra is a tool that relies on the charge density that we obtained from a self-consistent Density Functional Theory (DFT) calculation. To simulate core-hole effects, a pseudopotential with a hole in the 1s state was used for K-edges of the absorbing atom. The pseudopotentials we used are publicly available on the QUANTUM ESPRESSO web site *http://www.quantum-espresso.org*. We report in Tab. 3.2 pseudopotentials (PP) that were used in the calculations.

Atom	PP	1s-PP
C	*C.pbe-mt-gipaw.UPF*	*C.star1s-pbe-mt-gipaw.UPF*
Si	*Si.pbe-van-gipaw.UPF*	*Si.star1s-pbe-van-gipaw.UPF*
O	*O.pbe-van-gipaw.UPF*	*O.star1s-pbe-van-gipaw.UPF*
H	*H.pbe-rrkjus.UPF*	

Table 3.2: *List of pseudopotentials used for the calculations of the theoretical XANES spectra.*

The self-consistent calculation was then performed on a supercell including the absorbing atom in which the hole is present. The size of the supercell has been verified to be sufficient to obtain the spectrum convergence. We included two GIPAW projectors in the reconstruction of the all electron wave function. The self consistent DFT calculations were performed with a kinetic energy cutoff for wave functions equal to 410 eV and kinetic energy cutoff for density and potential equal to 1640 eV. We used a 1 1 3 k-point sampling. XSpectra calculates then the K-edge XAS using the continued fraction method and the Lanczos approach suitable for ultrasoft pseudopotentials [Gougoussis et al., 2009]. This approach does not require the explicit calculation of empty states and it is consequently very fast. For the spectra calculations we used a 1 1 4 k-point sampling and three different polarization vectors of the incident X-ray, namely one along the nanowire's main axis and two perpendicular to it. We averaged the different contributions. The position of the absorbing atoms is not actually completely equivalent, in principle, the total spectra should be obtained by a weighted average of the spectra obtained for different positions of the absorbing atoms. Here, due to the computational cost

and the intrinsic ideality of a small computational model we used only one posi-
tion of the absorbing atom for each spectrum. For the core, we chose the absorbing
atom to be along the axis of the nanowire, while in the shell we chose a random
postion. A complete weighted average of the spectra for different positions of the
absorbing atom is beyond of the scope of this work.

A good agreement of our computational model with experimental and com-
putational results obtained by Liu et al. [Liu et al., 2010] was found in the case of
bulk silicon carbide, and the SiC core nanowire with -OH terminations. Given the
good agreement of these cases with literature results, we extended our calcula-
tions to the full SiC/SiO_x core/shell nanowire model, comparing the results with
the experimental spectra.

3.5   Results and discussion

As first step we validated XANES spectra calculations for both SiC bulk crys-
tal and amorphous SiO_2. Once validated the method for the two components
of SiC/SiO_x core/shell NW, we moved to the calculation of XANES spectra of
the SiC/SiO_x core/shell nanowires. For carbon the spectra were computed also
for SiC+OH nanowires and compared with the spectra for HF etched SiC/SiO_x
core/shell nanowires.

Starting from K-edge O spectra, we report in Fig. 3.6 the comparison between
the calculated spectrum and experimental TEY as collected by Nardi group. The
main peak is correctly recovered by the calculation. A secondary peak at about
530 eV is not present in O K-edge simulations. This peak, is likely to be related to
groups such as carbonyl-type or carboxyl-type functional groups, that are not in-
cluded in the present model. The study of the influence of defects and inclusions,
we are currently preforming, should shed light on the nature this peak.

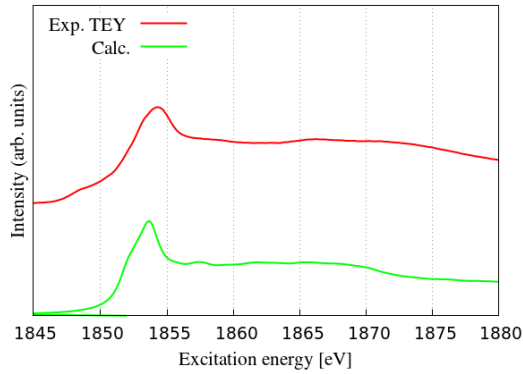In Fig. 3.7 we report the comparison between calculated Si K-edge absorption
spectrum of $SiC+SiO_x$ nanowires, in which the silicon atom with the core-hole
was located in the shell, and the experimental TEY spectrum collected by group
of Nardi. Also in this case we obtained a good agreement between measured and
calculated spectra.

Differently from the previous cases, the C K-edge absorption spectrum was
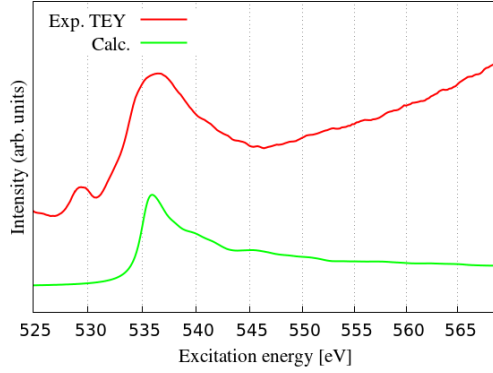
Figure 3.6: *Comparison between the calculated O K-edge absorption spectrum of SiC+SiO$_x$ nanowires and the experimental TEY spectrum collected by group of Nardi.*

Figure 3.7: *Comparison between the calculated Si K-edge absorption spectrum of SiC/SiO$_x$ nanowire, in which the silicon atom with the core-hole was located in the shell, and the experimental TEY spectrum collected by group of Nardi.*

computed for both SiC/SiO$_x$ core/shell and for SiC+OH nanowire. Indeed, SiC+OH NW represents our simplified model for the SiC/SiO$_x$ core/shell nanowire -after- the etching of the shell in HF. For both SiC/SiO$_x$ core/shell and SiC+OH nano- wires we report the X-ray fluorescence yield (FLY) spectra taken from Ref. [Liu et al., 2010]. This technique collects X-ray coming from the nanowire core, and not

mainly from the surface as the TEY technique.

In Fig. 3.8 we report the FLY C K-edge absorption spectrum taken from Ref. [Liu et al., 2010], the TEY spectrum from Nardi group for HF etched NWs and the calculated spectra for SiC+OH NW. The main features of the experimental spectra are recovered with the use of our simplified model. Indeed, the two main peaks are recovered and the general shape of the peak at lower energy is very similar to the experimental one. However, the peak that is present in both the experimental spectra at ~285 eV can not be obtained with our model.

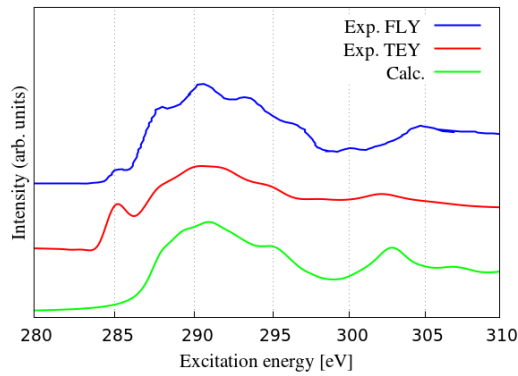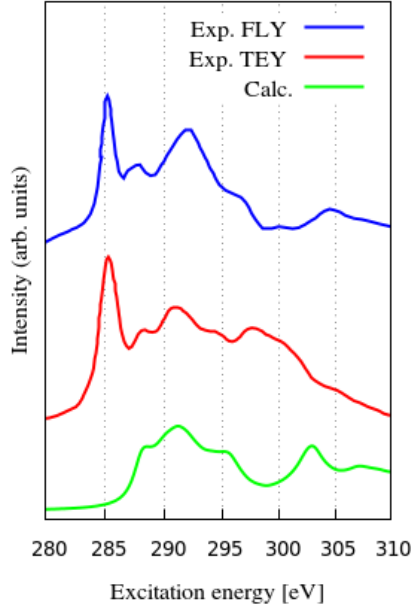**Figure 3.8:** *Comparison between the calculated C K-edge absorption spectrum of SiC+OH$_x$ nanowire, the experimental TEY spectrum collected by group of Nardi, and the experimental FLY spectrum obtained from Ref. [Liu et al., 2010].*

We can compare these results with the spectra for the full SiC/SiO$_x$ core/shell NWs. These spectra are reported in Fig. 3.9.

The FLY spectrum taken from Ref. [Liu et al., 2010] and the TEY spectrum from Nardi group for HF etched NWs show very similar features that distinguish them from the calculated spectrum. Indeed, as reported by Liu. et al. in Ref. [Liu et al., 2010] in the experimental spectra are included two large peaks one at 286 eV and the other 292 eV that can be ascribed to the π and π^* excitation energies for the $1s$ electrons of carbon atoms arranged in graphene-like structure. This kind of contamination seems to be very common as they were found in both the experimental data sets.

Figure 3.9: *Comparison between the calculated C K-edge absorption spectrum of SiC+SiO$_x$ nanowire, the experimental TEY spectrum collected by group of Nardi and the experimental FLY spectrum obtained from Ref. [Liu et al., 2010].*

3.6   Conclusions

Recently, has been proposed a promising porphyrin-based method for cancer therapy that takes advantage of SiC/SiO$_x$ core/shell NWs. To optimize this method, synergic experimental and computational studies are necessary in order to shed light on the underlying mechanisms. In this chapter, we presented the development a realistic model of SiC/SiO$_x$ core/shell NW based on experimental information and molecular dynamics simulations for the calculation of XANES spectra.

The NW's model was validated against the data reported in literature and allows to reproduce the main features of XANES spectra of these structures. Fur-

thermore, SiC/SiO$_x$ core/shell NWs were experimentally produced via a low-cost carbothermal method. The XANES spectra of SiC/SiO$_x$ core/shell NWs were then collected using the TEY mode and were compared to calculated spectra.

A overall good agreement was found between calculated and experimental spectra. The NW model allows to reproduce the oxygen and the silicon XANES spectra. In these cases there are no strong contamination effects, and the agreement of simulated and computed spectra is overall good. With regard to carbon XANES spectra, in the comparison between calculated and experimental spectra shows the effectiveness of the SiC+OH model in reproducing the experimental spectra of the HF etched SiC/SiO$_x$ core/shell NWs. In the case of the SiC/SiO$_x$ core/shell NWs the experimental spectra present similar features that are very different from those of calculated spectrum.

As pointed out in the literature the two main peaks at 286 and 292 eV in the experimental XANES spectra obtained for carbon K-edge can not derive from the bare SiC/SiO$_x$ core/shell NW, and are not reproduced by the model. These two peaks can be associated to carbon impurities contained in the NW silica shell or attached to the surface.

If the most probable carbonaceous form of inclusion is amorphous carbon or graphitized carbon layers that give reason of the two peaks, the modeling of a realistic distribution of is not possible without modeling the whole experimental growth process.

In summary, we developed a realistic model of SiC/SiO$_x$ core/shell that we profitably used to calculate XANES spectra. The comparison with the experimental spectra show that our model captures the main features of the experimental systems. The model we developed in this study represents a significant step towards the modeling and the optimization of the full porphyrin-based method for cancer therapy.

3.7 Open research lines on core/shell nanowire modeling

As we have seen in this chapter the main features of the experimental XANES spectra were reproduced using the SiC/SiO$_x$ core/shell model we developed. However, some improvements could be carried on. The first one is the study of the contribution to the XANES spectra of specific defects or inclusions, for example carbon-based inclusions. A second research line could be the development of a SiC/SiO$_x$ core/shell model by means of the modeling of growth process.

Chapter 4

Modeling of electron holography in folded graphene sheets

In the first part of this chapter we present some results about the modeling of electron holography response for graphene-based structures. In particular, we will focus on graphene folded edges. In the second part we discuss the results of some preliminary GW calculations that aim to estimate the self-energy contribution to the quasi-particle energies of graphene up to 50 eV.

4.1 Introduction to electron holography modeling

We start introducing electron holography that is one of the many techniques that can be used in the framework of Transmission Electron Microscopy (TEM).

The electron holography response is related to the electrostatic potential so that a proper interpretation of the experimental results needs information about this quantity. The electron holography response can be also dependent from magnetic fields, but these effects are not considered in this work.

The dependence of electron holography response on electric and magnetic fields makes this technique applicable to a broad range of problems. It has been used for experimental exploration of the Aharonov-Bohm effect reported in [Osakabe et al., 1986] as well as for nanoscale magnetic and electric field mapping [McCartney et al., 2010]. In some review articles can be found further applications, see for example Ref. [McCartney and Smith, 2007]. Surface electrostatic potentials in carbon nanotubes and graphene membranes were also studied [Ortolani et al., 2011]. Recently, electron holography was used in the study of ultra-thin layered WSe$_2$ [Winkler et al., 2017].

The experimental response in electron holography is essentially a phase shift between a part of electron beam that interacts with the sample and a part that does not interact with it. A sketch of the experimental setup is reported in Fig. 4.1. High-energy electrons ($80 - 200$ keV) are accelerated in a TEM in an off-axis scheme. The electron beam is split into two parts. One of the two parts of the electron beam goes through the sample, the other proceeds in the vacuum. The two parts of the beam are then deflected to produce an interference pattern on the screen.

The intesity of the interference fringes is given by

$$I(x,y) = A_1^2 + A_2^2 + 2A_1 A_2 \cos(\Delta\varphi) \tag{4.1}$$

where A_1 and A_2 are the amplitudes of the between the reference and the object wave, respectively, and $\Delta\varphi$ the difference in their phases.

The electron holography phase shift is given by

$$\Delta\varphi = \frac{\pi}{\lambda\tilde{U}}\frac{\tilde{m}}{m_0}\bar{V}(x,y) \tag{4.2}$$

where λ is the electron wavelength and m_0 its rest mass. The phase shift is proportional to the integral of the electric potential $V(\vec{r})$ along the beam axis z:

$$\bar{V}(x,y) = \int V(\vec{r})\mathrm{d}z \tag{4.3}$$

where x and y are spatial coordinates on the plane perpendicular to the beam axis. The relativistic effects are taken into account at the first order in the two quantities
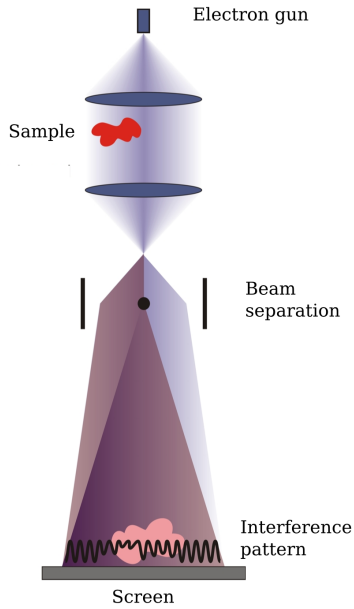
Figure 4.1: *High-energy electrons (80 − 200 keV) are accelerated in a TEM in an off-axis scheme. The electron beam is split into two parts. One of the two parts of the electron beam goes through the sample, the other proceeds in the vacuum. The two parts of the beam are then deflected to produce an interference pattern the screen.*

$\tilde{m}$ and $\tilde{U}$

$$\tilde{m} = m_0(1 + \epsilon), \ \tilde{U} = U(1 + \epsilon/2)$$

where $\epsilon = eU/m_0c^2$ quantifies the energy due to the accelerating potential.

For example when $U = 100$ kV one has $\epsilon \simeq 0.2$ indicating that relativistic effects are not negligible in this regime. Differently from relativistic effects that are more and more relevant with the increase of beam energy, all the non-classical effects, such as for example self-energy, become negligible with energy increase [Saldin and Spence, 1994].

Because the non-classical effects shoud be in general negligible in the calculation of the interaction between the electron beam and the sample, a Density Functional Theory (DFT) approach can be profitably used. Indeed, the only thing that is necessary for the electrostatic potential calculation is the charge density

distribution, that is accurately computed by means of DFT.

In the following we present the calculation at DFT level of the integrated potential for various graphene based nanostructure, starting by modeling their structure. Due to computational demand of DFT, some structures were relaxed by means of Molecular Mechanics (MD) methods, limiting the DFT calculation to the single point charge density calculation.

4.2 Computational methods

Among the simplest structures that can be found at experimental level, different from flat graphene sheets, nanotubes and fullerenes, there are the folded graphene edges. This kinds of structures present stacked graphene layers in the flat part as well as graphene sheets with various distances and slope near the folded edge. Due to these characteristics their represent an optimal test for electron holography modeling. The first step for electron holography modeling was the realization of the structures that we want to use for DFT calculations. We chose to mimic the folded edges with squeezed carbon nanotubes, that permit to obtain symmetric structures without the necessity of saturating eventual free bonds of the carbon atoms of the free edges. This allows to avoid the spurious electrostatic potential given by the hydrogen termination. Similar structures were studied in Ref. [Feng et al., 2009] finding a dipole moment for a folded graphene edge. With respect to this work we added the study of the turbostatic and double layer cases.

Using this approach the single layer folded edge results to be very simple to model, indeed we have to prepare a nanotube with a reasonable diameter, then we can squeeze it by means of a MD run, by applying a force at two diametral opposite lines. The only need is that the collapsed structure should be stable once minimized. In this case we can then proceed with a DFT self consistent relaxation of the atomic positions and finally with the calculation of the charge density, from which we extract the electrostatic potential.

In this work we used an MD approach to model the larger structures, however other intermediate approaches can be used, for example Density Functional Tight Binding (DFTB) method within DFTB+ code [Aradi et al., 2007].

The molecular dynamics simulations were performed within LAMMPS soft-
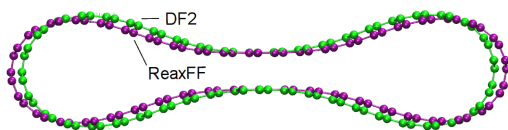
Figure 4.2: *Comparison of the atomic positions of a squeezed nanotube at MD level with ReaxFF potential [Chenoweth et al., 2008, Budzien et al., 2009] and those at DFT level with* `C.pbe-mt_fhi.UPF` *pseudopotential and* VDW-DF2-C09 *scheme for van der Waals interaction.*

ware [Plimpton, 1995], using ReaxFF potential [Chenoweth et al., 2008] with parametrization from Budzien et al. [Budzien et al., 2009], that we found sufficiently good in reproducing the geometry of squeezed nanotubes in the case in which we relaxed the structures also within a full DFT approach. We also found this potential to work better than, for example, AIREBO [Stuart et al., 2000] potential for smaller structures. However, increasing the dimensions of the squeezed carbon nanotube, AIREBO potential starts to outperform ReaxFF. Anyway, for all the structures we relaxed with MD we used ReaxFF, because for our small systems the overall agreement with DFT was good.

We report in Fig. 4.2, as example, the comparison of the atomic positions of a squeezed nanotube at MD level with ReaxFF potential [Chenoweth et al., 2008, Budzien et al., 2009] and the same structure at DFT level with `C.pbe-mt_fhi.UPF` pseudopotential and VDW-DF2-C09 scheme for van der Waals interaction. Due to the average difference in bond length between ReaxFF model and DFT one, we proportionally rescaled all the atomic coordinates to match the typical DFT average bond length for carbon structures (rescaling factor $1.418/1.447$). In this way we avoided to do single point DFT calculations on structures with too long bonds length.

A different approach was used in the case of the simulation of double layer folded edges. Indeed, in this case using the same approach as before, i.e. taking a double wall carbon nanotube and squeezing it, produces a stressed structure, and the inner nanotube could have a too large circonference to be easily accomodate within the squeezed structure. In this case, a possibility to solve this problem is
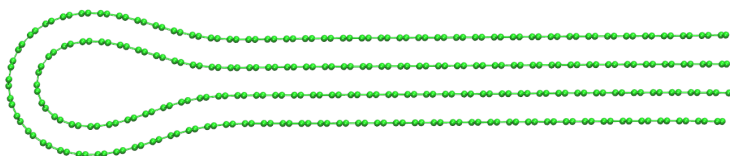
Figure 4.3: *A folded bilayer edge, relaxed at MD level. The structure during the relaxation was described by means of ReaxFF potential [Chenoweth et al., 2008, Budzien et al., 2009].*

producing various samples with different diameter of inner carbon nanotube and taking that, once squeezed, present the lower energy per atom.

However, we used a different approach that avoids the dynamical squeezing of the sample. In particular we started form folded double layer of graphene, that we relaxed by means of MD run in Fig. 4.3. It could be more accurate to saturate the bonds at the end of the layers with hydrogen atoms but due to the dimension of the sample the minimum energy geometry is essentially driven by the elasticity of the folded parte and the interlayer interaction in the flat part. A sketch of the used procedure is reported in Fig. 4.4. As first step we cut the atoms at the edge. Subsequently we used a centrosymmetryc reflection in two dimension of the coordinates to built up the other half of the structure. Finally, after a small shift of the coordinates of the atoms at the joint to close the gap in the outer layer, we relaxed the structure by means of a MD run.

We show the bilayer folded edge closed model in Fig. 4.5. In this figure we report the comparison of the atomic positions of a folded bilayer edge, green points, and the optimized collapsed nanotube as model of the folded edge, both at MD level.

For DFT calculations we used the Generalized Gradient Approximation (GGA) pseudopotentials, it seems indeed safer to reproduce at least the total charge inside core regions, and we included the van der Waals term.
We chose the `C.pbe-mt_fhi.UPF` pseudopotential with 1s electrons in the core, Martins-Trouiller pseudization because, unlike other choices that we have examined, it gives a pretty flat value of vacuum potential far from regions occupied by atoms. The numerical noise in vacuum regions may indeed modify the re-
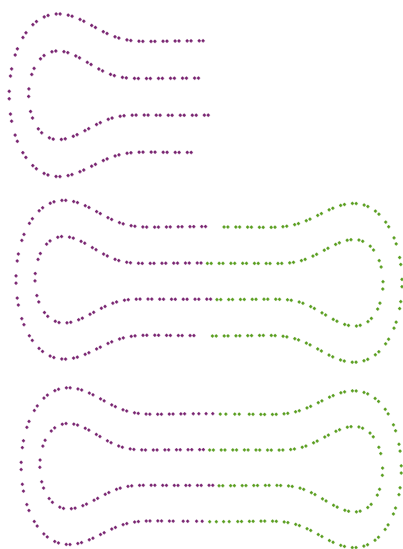
Figure 4.4: *A sketch of the procedure steps used for the construction of the model for the double layer folded edge. The first tep was to cut a part of the relaxed structure presented in Fig. 4.3, the second step a centrosymmetryc reflection in two dimension of the coordinates, the last step a small shift of the atomic coordinates of the outer layer to close the gap at the junction.*
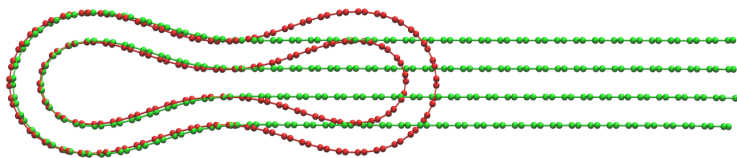
Figure 4.5: *Comparison of the atomic positions of a folded bilayer edge, green points, and the optimized collapsed nanotube as model of the folded edge at MD level. The inner nanotube circonference was chosen to produce the lower stressed structure. The structures during the relaxation were described by means of ReaxFF potential [Chenoweth et al., 2008,Budzien et al., 2009].*

sults due to the numerical integration along the beam axis. The van der Waals interaction was included by means of the VDW-DF2-C09 scheme (with Cooper's exchange functional [Cooper, 2010] and improved Chalmers-Rutgers VDW [Lee

et al., 2010]).

Due to the finite size of the supercell the periodicity influences the vacuum potential $v_{\mathrm{vac}}(D)$. This is indeed dependent on the supercell relevant size D, in particular inversely proportional to D, vanishing only when $D \to \infty$. As detailed in the following sections, the electrostatic potential to be integrated to phase shift evaluation needs to be shifted by the corresponding zero point value: $V = v - v_{\mathrm{vac}}(D)$.

In the calculation of the phase shift we used to simulate the typical regime for holography $U = 100$ kV, a value 0.00922 (V nm)$^{-1} = 9.22 \times 10^6$ (V m)$^{-1}$ was used for the prefactor that relates $\Delta\varphi$ (in radians) and $\bar{V}$ in eq. (4.2).

4.3   Results and discussion

We performed the calculation of the integrated potential along the z direction for the follwing structures:

- a $(22, 22)$ carbon nanotube

- a squeezed $(22, 22)$ carbon nanotube

- a squeezed $(36, 0)$ carbon nanotube

- a squeezed $(11, 44)$ carbon nanotube

- a double layer built up on a $(22, 22)$ carbon nanotube

The first three samples were self-consistently relaxed at full DFT level. The last two were instead first relaxed by means of MD, then their coordinates were rescaled and a single point DFT calculation was done. We chose to study the squeezed $(11, 44)$ carbon nanotube as model for a chiral folded edge for which we have some experimental results, that will be published in the next future. The double layer structure was built up as described before. The final structure is equivalent to covering a $(22, 22)$ carbon nanotube with a $(27, 27)$ carbon nanotube, in this way the stress on the structure was minimized. Similar structures were analized in Ref. [Feng et al., 2009], in our work however we considered a GGA XC functional with van der Waals terms instead of an LDA approximation, furthermore we extend the analysis to a chiral and a bilayer model.

System	D_x (nm)	D_z (nm)	# of atoms	v_{vac} (eV)
nanotube (22,22)	5	5	88	-0.725
squeezed (22,22)	6	2	88	-3.02
squeezed (36,0)	6	2	144	-2.87
squeezed (11,44)	8	4	308	-1.50
squeezed double (22,22)	7	4	196	-2.87

Table 4.1: *We report in the first column the denomination of the considered structures, in the second and the third columns the dimensions of the supercell perpendicular to the structures axis, in the fourth column is reported the nuber of atoms. In the last one the vacuum coulombic potential for the given supercell.*

We report in the first column of Tab. 4.1 the denomination of the considered structures, in the second and the third columns the dimensions of the supercell perpendicular to the structures axis, in the fourth column is reported the nuber of atoms. In the last one the vacuum potential for the given supercell. The vacuum potential was subtracted from the electrostatic potential data before the numerical integration along the beam direction.

In Fig. 4.6 we report a linescan along x (across the folded edge) of the potential profile integrated along z and averaged along the edge direction. In order to compare with an experimental signal we report also the same plot but with a running average along x with a resolution spot of 0.5 nm (fig. 4.7). The values of the integrated potential in the planar region settle to the value for two flat graphene planes at equilibrium distance as expected. While the experimental data show a sharp step, the averaged numerical data exhibit a gradual increase of the integrated potential where the two layer start to separate each other. Further increasing the resolution spot to 1 nm, and cosidering for example the squeezed (11,44) chiral nanotube, the offset from the planar region to the plateau can be estimated in 0.3 Vnm (that is 0.003 rad, that is rather smaller than the experimental measurement for the same geometry of about 0.02 rad).
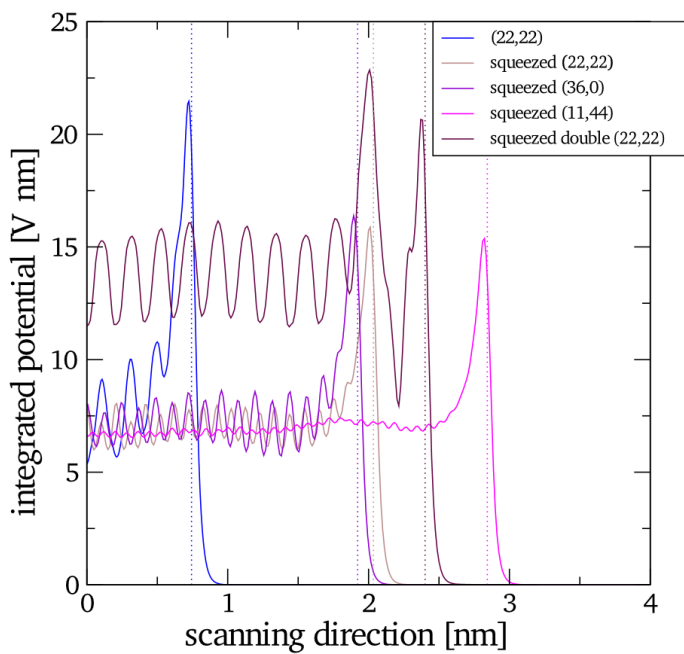
Figure 4.6: *Integrated potential (units Vnm) of the structures studied in this work. Dotted vertical lines mark the position of the outermost atom along the scanning direction.*
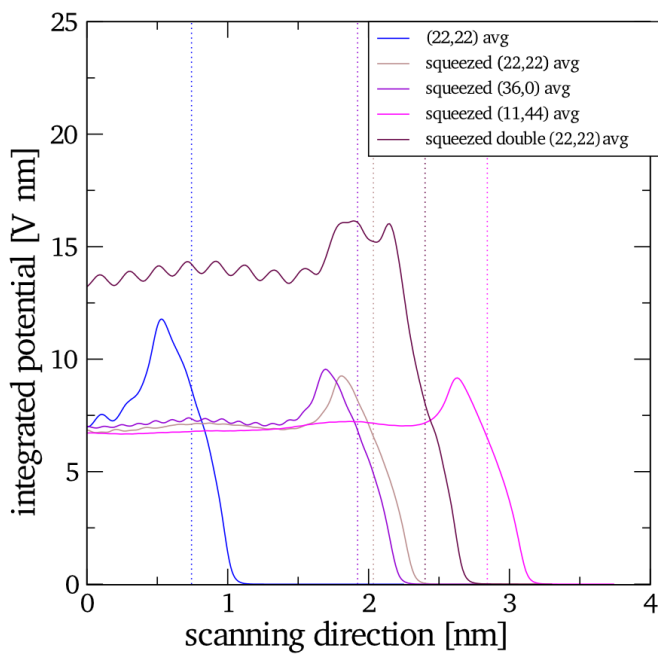
Figure 4.7: *The same as in fig. 4.6 using a running average filter over a box of lateral size 0.5 nm.*

4.4 Conclusions

One of the possible reasons for the discrepancy between theoretical results and experiments may be the approximate nature of DFT. In this chapter we present some calculations of electrostatic potential based on a more realistic approach to the electronic structure, but also more difficult to calculate. In this part of the chapter we presented various results on the modeling of graphene folded edges. The modeling of the structures was performed by means of MD and DFT calculations. We computed the integrated potential along the beam direction for a series of stuctures of folded edges, among these the most interesting were the chiral and the double layer structures. From a computational point of view the calculations were performed at high level of accuracy. However, the comparison of the values for for the integrated potential with those obtained from experimental data presents some discrepancies. On one hand the values of the integrated potential is in agreement with experimental data for the part in which the two graphene layers are completely stacked each other, on the other hand the plateau found in the experimental data, corrisponding to the separation of the two layers near the folded edge is strongly underestimated. This point remains to be further investigated to find the experimental reason of this high value for the integrated potential.

4.5 Introduction GW calculations

A more general approach could be used in evaluating the interaction between electrons and graphene, in which the many-body contribution are included. As anticipated above, some preliminary GW calculations are presented in this part of the chapter showing how at the computational level we found a relatively small contribution of the self-energy to the total interaction between the impinging electrons and graphene.

In the GW approximation [Hedin, 1965] the self-energy is

$$\Sigma^{GW}(r, r', \omega) = \frac{i}{2\pi} \int_{-\infty}^{+\infty} d\omega' G(r, r', \omega - \omega') W(r, r', \omega) \qquad (4.4)$$

that is the product of the Green's function G and the dynamically screened interaction defined as the bare Coulombian interaction v screened by the dynamical dielectric function. Vertex corrections are neglected both in the self-energy and in the polarizability (hence in W).

In the standard ab initio GW resolution procedure one builds G and W using the DFT KS electronic structure. The integral over the frequency is performed by a contour deformation (CD) method [Fleszar and Hanke, 1997] which consists in a deformation of the real axis contour such as to calculate the self-energy as an integral along the imaginary axis minus a contribution arising from the residual of the contour included poles of G. We avoided to use the plasmon-pole model (PPM) that is computionally cheaper, but is known only to be valid near the Fermi level. High bands should be better described by the numerical integration.

4.6 Computational methods

A GW calculation can be divided in three parts. The first is the calculation of the DFT-KS wavefunctions and eigenvalues, the second the calculation of the Dielectric Matrix ϵ and Screening W the third the calculation of the Self-Energy Σ and GW corrections. All the calculation reported here were performed by means of the code ABINIT code [Gonze et al., 2016].

For DFT-KS wavefunctions and eigenvalues we performed a standard ground-state DFT LDA calculation on a graphene cell with periodic boundary condition. The unit cell was hexagonal containing two carbon atoms (a = 0.24 nm). As used in Ref. [Trevisanutto et al., 2008] we used a plane waves basis set (62 Ry cutoff) and 38 Bohr of vacuum along the z direction. This distance should be sufficient to isolate the graphene layer from its periodic images. Again, as in Ref. [Trevisanutto et al., 2008] the Martins-Trouiller norm-conserving pseudopotentials with s and p electrons in the valence was used. This to validate our result against in those reported in that paper. The use of DFT-LDA for standard ground-state calculations was again motivated by the comparison of our results and those of Ref. [Trevisanutto et al., 2008].

The self-consistent quasiparticle method was performed on energies only. We used 62 Ry cutoff for the wavefunctions and the exchange part Σ_x of the self-

energy, 400 bands to calculate W and Σ. To fix the dimension of W and of the correlation part Σ_c as reciprocal space matrices we used 10 Ry. W was sampled over 10 frequencies on the real axis and 4 along the imaginary axis. The Brillouin zone was sampled with a (16 16 1) Monkhorst-Pack k-point grid. The calculation of the quasiparticle GW energies was performed for Γ point only.

## 4.7   Results and discussion

In Fig. 4.8 we compare the KS DFT-LDA (circles) energies from Ref. [Trevisanutto et al., 2008] energies with the values calculated in this work (dots), as function of the band number. As espected the overall agreement is good validating our DFT-LDA calculation.

In Fig. 4.9 we report the comparison between quasiparticle GW energies (circles) from Ref. [Trevisanutto et al., 2008] and our results. Again, the agreement is good, considering that the literature data were extracted from the graph reported in Ref. [Trevisanutto et al., 2008].

Because the aim of this part of the chapter was to evaluate the contribution of the self energy to the LDA energies, we report in Fig. 4.10 the absolute value of its
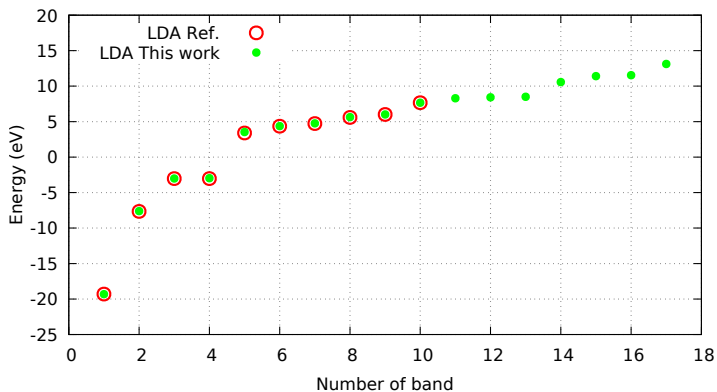
Figure 4.8: *Comparison between LDA energies (circles) from Ref. [Trevisanutto et al., 2008] and our results.*
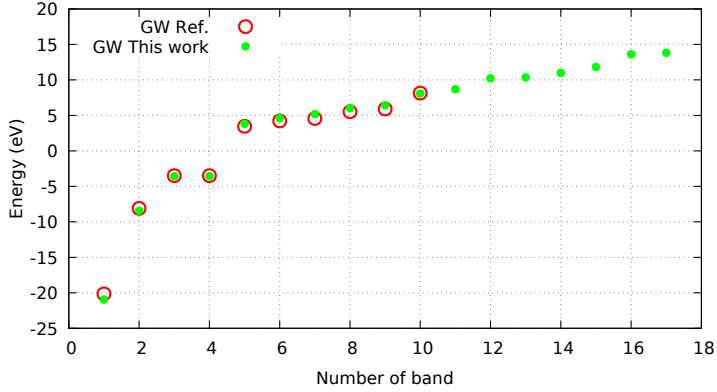
Figure 4.9: *Comparison between quasiparticle GW energies (circles) from Ref. [Trevisanutto et al., 2008] and our results.*

percentual contribution

$$F = abs[(GW - LDA)/LDA] \tag{4.5}$$

as function of the band number. abs indicates the absolute value, GW the quasiparticle energy and LDA the DFT energy. As reported in Fig. 4.10 F presents various peaks in the levels near the fermi energy, that is beetween the bands number 4 and 5. As the band number increases the general trend is a decreasing of the GW contribution. We find plateau starting from the band number 40, that has LDA energy 37.8 eV. The plateau presents an average value of 1.24 % that could be considered negligible.

The same data are reported in Fig. 4.11 as function of the LDA energies. The band structure becomes more compact when the band number increases, making more and more difficult to increase the energy by increasing the number of considered bands.
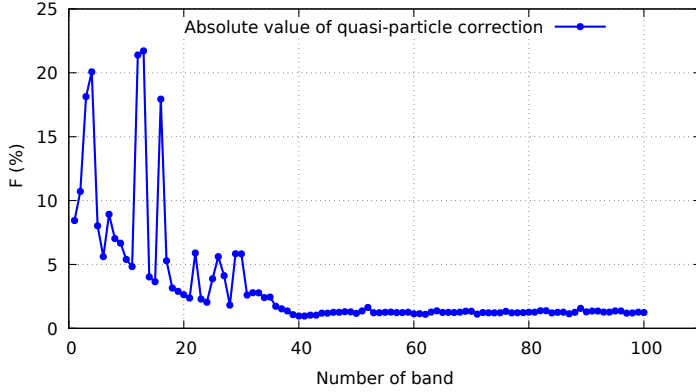
Figure 4.10: *Absolute value of self-energy correction F as function of band number.*
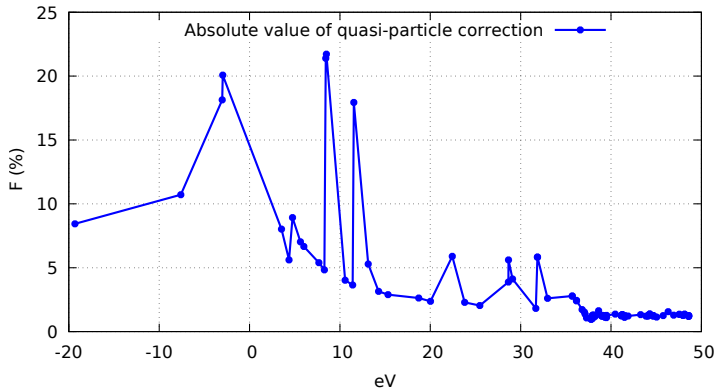
Figure 4.11: *Absolute value of self-energy correction F as function of LDA energy.*

4.8 Conclusions

We presented some preliminary calculations that aims to evaluate the self-energy correction F in the case of graphene. This contribution, that has to be considered in the case of different techniques such as Low Energy Electron Diffraction (LEED), can be in general neglected for electron holography. However, given the

peculiarity of graphene, we tried to give a computational evidence of this possibility, showing that for electrons with energies of the order of $40\,\mathrm{eV}$ the percentual self-energy contribution becomes stable. We found a value of approximatively $1.24\,\%$ that could be yet considered negligible. The approach used here, in which a large set of empty bands has to be considered in the calculation, it is not likely to be extended to high-energy regimes, however the indications obtained for low energy electrons seems sufficient to justify the neglecting of the self-energy contribution in electron holography simulations.

4.9 Open research lines on Electron Holography modeling of graphene

Further studies could be focused on folded edges with defective sites and inclusions. Indeed, the Electron Holography response is very sensitive to surface potential modification. The general approach can be extended to different 2D materials, for which Electron Holography is a valuable investigation technique.

Conclusions

In this thesis we presented various computational investigations with the focus on graphene-based systems for which the main properties emerges at the nanoscale. The results presented here are based on a broad range of computational techniques ranging from Molecular Dynamics and GCMC to Density Functional Theory.

We investigated novel materials promising for structural and impact absorption applications, graphene foams, showing the differences between random and regular ones. We developed a procedure to realize realistic computational models of these structures that can be further improved for an efficient modeling of graphene foams at larger scale, including multilayer walls. The modeling of these structures opens the possibility of study their interaction with different fillers, further enhancing their mechanical and thermal properties.

Graphene layers are also the main components of Pillared Graphene Frameworks, in which they are intercalated by organic moieties that act as spacers. The large specific surface of these structures and the possibility of tailor their properties by changing the pillar density and type, make these structure suitable for gas adsorption and separation. We explored these properties from a computational point of view, that enables a simple screening of the influence of the various parameters.

Some phenomena can not be assessed by means of classical methods such as Molecular Dynamics and GCMC only. XANES spectra for example, can be only calculated using higher level computational methods, in which the electronic structure of the system is explicitly considered. We presented a realistic model of a SiC/SiO_2 core/shell nanowire, a structure with promising application in cancer

treatment, and the calculation of XANES spectra. The comparison of the computational spectra with experimental data validated our model, and paves the way towards the inclusion in the model of the light-sensitive component.

We concluded this thesis focusing again on graphene, and in particular the electron holography response for folded sheets. Also in this case a Density Functional Theory approach was fundamental, due to the fact that the electrostatic potential is dependent from local charge distribution, that can not be assessed in a classical framework. We computed the integrated potential that is proportional to the phase shift of the impinging electrons. We further expanded this work evaluating the terms that are generally negelected in electron holography simulations, mainly the self-energy. We computed the self-energy correction in low-energy regimes using GW calculations. We presented some preliminary results that indicate a negligible contribution of self-energy starting from few tens of eV.

In this thesis we investigated a set of systems that can be profitabily studied by means of computer simulations. The modeling of these novel systems, as well as the choice of the adeguate computational methods has played a central role during all the thesis work. The structures and the validation presented here can be used to further improving the knowledge on nanoscopic systems that are more and more crucial in a broad range of research field, from biochemistry to materials science.

Bibliography

[Alonso, 2012] Alonso, J. A. C. (2012). The Storage of Hydrogen in Nanoporous Carbons. *Journal of the Mexican Chemical Society*, 56:261 – 269.

[Amirjalayer et al., 2007] Amirjalayer, S., Tafipolsky, M., and Schmid, R. (2007). Molecular dynamics simulation of benzene diffusion in mof-5: Importance of lattice dynamics. *Angewandte Chemie International Edition*, 46(3):463–466.

[Aradi et al., 2007] Aradi, B., Hourahine, B., and Frauenheim, T. (2007). Dftb+, a sparse matrix-based implementation of the dftb method. *Journal of Physical Chemestry*, 111.

[Ashby, 2006] Ashby, M. (2006). The properties of foams and lattices. *Philosophical Transactions of the Royal Society A: Mathematical, Physical and Engineering Sciences*, 364(1838):15–30.

[Avalle et al., 2001] Avalle, M., Belingardi, G., and Montanini, R. (2001). Characterization of polymeric structural foams under compressive impact loading by means of energy-absorption diagram. *International Journal of Impact Engineering*, 25(5):455–472.

[Avouris and Dimitrakopoulos, 2012] Avouris, P. and Dimitrakopoulos, C. (2012). Graphene: synthesis and applications. *Materials Today*, 15(3):86 – 97.

[Babarao et al., 2007] Babarao, R., Hu, Z., Jiang, J., Chempath, S., and Sandler, S. I. (2007). Storage and separation of co2 and ch4 in silicalite, c168 schwarzite, and irmof-1:a comparative study from monte carlo simulation. *Langmuir*, 23(2):659–666.

[Bae et al., 2008] Bae, Y.-S., Mulfort, K. L., Frost, H., Ryan, P., Punnathanam, S., Broadbelt, L. J., Hupp, J. T., and Snurr, R. Q. (2008). Separation of co2 from ch4 using mixed-ligand metal−organic frameworks. *Langmuir*, 24(16):8592–8598. PMID: 18616225.

[Banerjee et al., 2009] Banerjee, R., Furukawa, H., Britt, D., Knobler, C., O'Keeffe, M., and Yaghi, O. M. (2009). Control of pore size and functionality in isoreticular zeolitic imidazolate frameworks and their carbon dioxide selective capture properties. *Journal of the American Chemical Society*, 131(11):3875–3877. PMID: 19292488.

[Battisti et al., 2011] Battisti, A., Taioli, S., and Garberoglio, G. (2011). Zeolitic imidazolate frameworks for separation of binary mixtures of co2, ch4, n2 and h2: A computer simulation investigation. *Microporous and Mesoporous Materials*, 143(1):46 – 53.

[Baughman and Galvao, 1993] Baughman, R. H. and Galvao, D. S. (1993). Crystalline networks with unusual predicted mechanical and thermal properties. *Nature*, 365(6448):735–737.

[Becton et al., 2015] Becton, M., Zeng, X., and Wang, X. (2015). Computational study on the effects of annealing on the mechanical properties of polycrystalline graphene. *Carbon*, 86:338–349.

[Beke et al., 2016] Beke, D., Jánosi, T. Z., Somogyi, B., Major, D. A., Szekrényes, Z., Erostyák, J., Kamarás, K., and Gali, A. (2016). Identification of luminescence centers in molecular-sized silicon carbide nanocrystals. *The Journal Of Physical Chemistry (c)*, 120(1):685–691.

[Bonatti and Mohr, 2017] Bonatti, C. and Mohr, D. (2017). Large deformation response of additively-manufactured fcc metamaterials: From octet truss lat-

tices towards continuous shell mesostructures. *International Journal of Plasticity*, 92(Supplement C):122 – 147.

[Buch, 1994] Buch, V. (1994). Path integral simulations of mixed para-d2 and ortho-d2 clusters: The orientational effects. *The Journal of Chemical Physics*, 100(10):7610–7629.

[Budzien et al., 2009] Budzien, J., Thompson, A. P., and Zybin, S. V. (2009). Reactive molecular dynamics simulations of shock through a single crystal of pentaerythritol tetranitrate. *The Journal of Physical Chemistry B*, 113(40):13142–13151. PMID: 19791817.

[Burress et al., 2010] Burress, J. W., Gadipelli, S., Ford, J., Simmons, J. M., Zhou, W., and Yildirim, T. (2010). Graphene oxide framework materials: Theoretical predictions and experimental results. *Angewandte Chemie International Edition*, 49(47):8902–8904.

[Cao, 2005] Cao, A. (2005). Super-compressible foamlike carbon nanotube films. *Science*, 310(5752):1307–1310.

[Celzard et al., 2010] Celzard, A., Zhao, W., Pizzi, A., and Fierro, V. (2010). Mechanical properties of tannin-based rigid foams undergoing compression. *Materials Science and Engineering: A*, 527(16–17):4438 – 4446.

[Challa et al., 2002] Challa, S. R., Sholl, D. S., and Johnson, J. K. (2002). Adsorption and separation of hydrogen isotopes in carbon nanotubes: Multicomponent grand canonical monte carlo simulations. *The Journal of Chemical Physics*, 116(2):814–824.

[Chenoweth et al., 2008] Chenoweth, K., van Duin, A. C. T., and Goddard, W. A. (2008). Reaxff reactive force field for molecular dynamics simulations of hydrocarbon oxidation. *The Journal of Physical Chemistry A*, 112(5):1040–1053.

[Colon and Snurr, 2014] Colon, Y. J. and Snurr, R. Q. (2014). High-throughput computational screening of metal-organic frameworks. *Chem. Soc. Rev.*, 43:5735–5749.

[Coluci et al., 2007] Coluci, V. R., Braga, S. F., Baughman, R. H., and Galvão, D. S. (2007). Prediction of the hydrogen storage capacity of carbon nanoscrolls. *Phys. Rev. B*, 75:125404.

[Coluci and Pugno, 2010] Coluci, V. R. and Pugno, N. M. (2010). Molecular dynamics simulations of stretching, twisting and fracture of super carbon nanotubes with different chiralities: Towards smart porous and flexible scaffolds. *Jnl of Comp & Theo Nano*, 7(7):1294–1298.

[Cooper, 2010] Cooper, V. R. (2010). Van der waals density functional: An appropriate exchange functional. *Phys. Rev. B*, 81:161104.

[Deshpande et al., 2001] Deshpande, V., Fleck, N., and Ashby, M. (2001). Effective properties of the octet-truss lattice material. *Journal of the Mechanics and Physics of Solids*, 49(8):1747–1769.

[Devynck and Pasquarello, 2007] Devynck, F. and Pasquarello, A. (2007). Semiconductor defects at the 4h-sic(0001)/sio2 interface. *Physica B: Condensed Matter*, 401-402(Supplement C):556 – 559.

[Ding et al., 2007] Ding, F., Lin, Y., Krasnov, P. O., and Yakobson, B. I. (2007). Nanotube-derived carbon foam for hydrogen sorption. *J. Chem. Phys.*, 127(16):164703.

[Dong et al., 2013] Dong, H., Hou, T., Sun, X., Li, Y., and Lee, S. (2013). The structures and properties of si/sio$_2$ core/shell quantum dots studied by density-functional tight-binding calculations. *Applied physics letters*, 103.

[Duren et al., 2009] Duren, T., Bae, Y.-S., and Snurr, R. Q. (2009). Using molecular simulation to characterise metal-organic frameworks for adsorption applications. *Chem. Soc. Rev.*, 38:1237–1247.

[Duren et al., 2004] Duren, T., Sarkisov, L., Yaghi, O. M., and Snurr, R. Q. (2004). Design of new materials for methane storage. *Langmuir*, 20(7):2683–2689.

[Fabbri et al., 2010] Fabbri, F., Rossi, F., Attolini, G., Salviati, G., Iannotta, S., Aversa, L., Verucchi, R., Nardi, M., Fukata, N., Dierre, B., and Sekiguchi, T. (2010). Enhancement of the core near-band-edge emission induced by an

amorphous shell in coaxial one-dimensional nanostructure: the case of sic/sio$_2$ core/shell self-organized nanowires. *Nanotechnology*, 21.

[Feng et al., 2009] Feng, J., Qi, L., Huang, J. Y., and Li, J. (2009). Geometric and electronic structure of graphene bilayer edges. *Phys. Rev. B*, 80:165407.

[Fleck et al., 2010] Fleck, N. A., Deshpande, V. S., and Ashby, M. F. (2010). Micro-architectured materials: past, present and future. *Proceedings of the Royal Society of London A: Mathematical, Physical and Engineering Sciences*, 466(2121):2495–2516.

[Fleszar and Hanke, 1997] Fleszar, A. and Hanke, W. (1997). Spectral properties of quasiparticles in a semiconductor. *Phys. Rev. B*, 56:10228–10232.

[Frank et al., 2007] Frank, I., Tanenbaum, D. M., Van der Zande, A., and McEuen, P. L. (2007). Mechanical properties of suspended graphene sheets. *Journal of Vacuum Science & Technology B*, 25(6):2558–2561.

[Garberoglio, 2012] Garberoglio, G. (2012). Obgmx: A web-based generator of gromacs topologies for molecular and periodic systems using the universal force field. *Journal of Computational Chemistry*, 33(27):2204–2208.

[Garberoglio et al., 2015] Garberoglio, G., Pugno, N. M., and Taioli, S. (2015). Gas adsorption and separation in realistic and idealized frameworks of organic pillared graphene: A comparative study. *The Journal of Physical Chemistry C*, 119(4):1980–1987.

[Garberoglio et al., 2005] Garberoglio, G., Skoulidas, A. I., and Johnson, J. K. (2005). Adsorption of gases in metal organic materials: comparison of simulations and experiments. *The Journal of Physical Chemistry B*, 109(27):13094–13103.

[Garberoglio and Taioli, 2012] Garberoglio, G. and Taioli, S. (2012). Modeling flexibility in metal–organic frameworks: Comparison between density-functional tight-binding and universal force field approaches for bonded interactions. *Microporous and Mesoporous Materials*, 163:215 – 220.

[Getman et al., 2012] Getman, R. B., Bae, Y.-S., Wilmer, C. E., and Snurr, R. Q. (2012). Review and analysis of molecular simulations of methane, hydrogen, and acetylene storage in metal–organic frameworks. *Chemical Reviews*, 112(2):703–723.

[Giannozzi et al., 2009] Giannozzi, P., Baroni, S., Bonini, N., Calandra, M., Car, R., Cavazzoni, C., Ceresoli, D., Chiarotti, G. L., Cococcioni, M., Dabo, I., Corso, A. D., de Gironcoli, S., Fabris, S., Fratesi, G., Gebauer, R., Gerstmann, U., Gougoussis, C., Kokalj, A., Lazzeri, M., Martin-Samos, L., Marzari, N., Mauri, F., Mazzarello, R., Paolini, S., Pasquarello, A., Paulatto, L., Sbraccia, C., Scandolo, S., Sclauzero, G., Seitsonen, A. P., Smogunov, A., Umari, P., and Wentzcovitch, R. M. (2009). Quantum espresso: a modular and open-source software project for quantum simulations of materials. *Journal of Physics: Condensed Matter*, 21(39):395502.

[Gonze et al., 2016] Gonze, X., Jollet, F., Araujo, F. A., Adams, D., Amadon, B., Applencourt, T., Audouze, C., Beuken, J.-M., Bieder, J., Bokhanchuk, A., Bousquet, E., Bruneval, F., Caliste, D., Côté, M., Dahm, F., Pieve, F. D., Delaveau, M., Gennaro, M. D., Dorado, B., Espejo, C., Geneste, G., Genovese, L., Gerossier, A., Giantomassi, M., Gillet, Y., Hamann, D., He, L., Jomard, G., Janssen, J. L., Roux, S. L., Levitt, A., Lherbier, A., Liu, F., Lukacevic, I., Martin, A., Martins, C., Oliveira, M., Poncé, S., Pouillon, Y., Rangel, T., Rignanese, G.-M., Romero, A., Rousseau, B., Rubel, O., Shukri, A., Stankovski, M., Torrent, M., Setten, M. V., troeye, B. V., Verstraete, M., Waroquier, D., Wiktor, J., Xue, B., Zhou, A., and Zwanziger, J. (2016). Recent developments in the ABINIT software package. *Computer Physics Communications*, 205:106.

[Goodbody et al., 1991] Goodbody, S. J., Watanabe, K., MacGowan, D., Walton, J. P. R. B., and Quirke, N. (1991). Molecular simulation of methane and butane in silicalite. *J. Chem. Soc., Faraday Trans.*, 87:1951–1958.

[Gougoussis et al., 2009] Gougoussis, C., Calandra, M., Seitsonen, A. P., and Mauri, F. (2009). First-principles calculations of x-ray absorption in a scheme based on ultrasoft pseudopotentials: From α-quartz to high-T_c compounds. *Phys. Rev. B*, 80:075102.

[Green, 1954] Green, M. S. (1954). Markoff random processes and the statistical mechanics of time dependent phenomena. ii. irreversible processes in fluids. *The Journal of Chemical Physics*, 22(3):398–413.

[Gross and Fricke, 1995] Gross, J. and Fricke, J. (1995). Proceedings of the second international conference on nanostructured materials scaling of elastic properties in highly porous nanostructured aerogels. *Nanostructured Materials*, 6(5):905 – 908.

[Haberer et al., 2010] Haberer, D., Vyalikh, D. V., Taioli, S., Dora, B., Farjam, M., Fink, J., Marchenko, D., Pichler, T., Ziegler, K., Simonucci, S., Dresselhaus, M. S., Knupfer, M., Büchner, B., and Grüneis, A. (2010). Tunable band gap in hydrogenated quasi-free-standing graphene. *Nano Letters*, 10(9):3360–3366. PMID: 20695447.

[Haldoupis et al., 2010] Haldoupis, E., Nair, S., and Sholl, D. S. (2010). Efficient calculation of diffusion limitations in metal organic framework materials: A tool for identifying materials for kinetic separations. *Journal of the American Chemical Society*, 132(21):7528–7539. PMID: 20450176.

[Hall et al., 2008] Hall, L. J., Coluci, V. R., Galvão, D. S., Kozlov, M. E., Zhang, M., Dantas, S. O., and Baughman, R. H. (2008). Sign change of Poisson's ratio for carbon nanotube sheets. *Science*, 320(5875):504–507.

[Harris and Yung, 1995] Harris, J. G. and Yung, K. H. (1995). Carbon dioxide's liquid-vapor coexistence curve and critical properties as predicted by a simple molecular model. *The Journal of Physical Chemistry*, 99(31):12021–12024.

[Hedin, 1965] Hedin, L. (1965). New method for calculating the one-particle green's function with application to the electron-gas problem. *Phys. Rev.*, 139:A796–A823.

[Hertag et al., 2011] Hertag, L., Bux, H., Caro, J., Chmelik, C., Remsungnen, T., Knauth, M., and Fritzsche, S. (2011). Diffusion of ch4 and h2 in zif-8. *Journal of Membrane Science*, 377(1–2):36 – 41.

[Hirschfelder and Curtiss, 1954] Hirschfelder, J. and Curtiss, C. (1954). Rb bird molecular theory of liquids and gases.

[Hodge et al., 2005] Hodge, A., Biener, J., Hsiung, L., Wang, Y., Hamza, A., and Satcher, J. (2005). Monolithic nanocrystalline Au fabricated by the compaction of nanoscale foam. *Journal of Materials Research*, 20:554–557.

[Humphrey et al., 1996] Humphrey, W., Dalke, A., and Schulten, K. (1996). VMD – Visual Molecular Dynamics. *Journal of Molecular Graphics*, 14:33–38.

[J. Frenzel, 2009] J. Frenzel, A. F. Oliveira N. Jardillier, T. . G. S. (2004-2009). Semi-relativistic, self-consistent charge slater-koster tables for density-functional based tight-binding (dftb) for materials science simulations. *TU-Dresden*.

[Jung et al., 2015] Jung, G., Qin, Z., and Buehler, M. J. (2015). Molecular mechanics of polycrystalline graphene with enhanced fracture toughness. *Extreme Mechanics Letters*, 2:52–59.

[Krishna and van Baten, 2007] Krishna, R. and van Baten, J. (2007). Using molecular simulations for screening of zeolites for separation of co2/ch4 mixtures. *Chemical Engineering Journal*, 133(1):121 – 131.

[Kubo, 1957] Kubo, R. (1957). Statistical-mechanical theory of irreversible processes. i. general theory and simple applications to magnetic and conduction problems. *Journal of the Physical Society of Japan*, 12(6):570–586.

[Kulkarni et al., 2013] Kulkarni, A. D., Truhlar, D. G., Goverapet Srinivasan, S., van Duin, A. C. T., Norman, P., and Schwartzentruber, T. E. (2013). Oxygen interactions with silica surfaces: Coupled cluster and density functional investigation and the development of a new reaxff potential. *The Journal of Physical Chemistry C*, 117(1):258–269.

[Kumar et al., 2014] Kumar, R., Suresh, V. M., Maji, T. K., and Rao, C. N. R. (2014). Porous graphene frameworks pillared by organic linkers with tunable surface area and gas storage properties. *Chem. Commun.*, 50:2015–2017.

[Laref et al., 2014] Laref, A., Alshammari, N., Laref, S., and Luo, S. J. (2014). A theoretical study of electronic and optical properties of sic nanowires and their quantum confinement effects. *Dalton Trans.*, 43:5505–5515.

[Lee et al., 2010] Lee, K., Murray, E. D., Kong, L., Lundqvist, B. I., and Langreth, D. C. (2010). Higher-accuracy van der waals density functional. *Phys. Rev. B*, 82:081101.

[Lenosky et al., 1992] Lenosky, T., Gonze, X., Teter, M., and Elser, V. (1992). Energetics of negatively curved graphitic carbon. *Nature*, 355(6358):333–335.

[Li, 2006] Li, Q. M. (2006). Compressive strain at the onset of densification of cellular solids. *Journal of Cellular Plastics*, 42(5):371–392.

[Li et al., 2015] Li, W., Zhao, J., and Wang, D. (2015). An amorphous sio2/4h-sic(0001) interface: Band offsets and accurate charge transition levels of typical defects. *Solid State Communications*, 205(Supplement C):28 – 32.

[Lindsay and Broido, 2010] Lindsay, L. and Broido, D. A. (2010). Optimized tersoff and brenner empirical potential parameters for lattice dynamics and phonon thermal transport in carbon nanotubes and graphene. *Phys. Rev. B*, 81:205441.

[Liu and Johnson, 2009] Liu, J. and Johnson, J. K. (2009). Prediction of ch4/h2 mixture selectivity in zn(tbip) from computer simulations. *Journal of Low Temperature Physics*, 157(3):268–276.

[Liu et al., 2010] Liu, L., Yiu, Y. M., Sham, T. K., Zhang, L., and Zhang, Y. (2010). Electronic structures and optical properties of 6h- and 3c-sic microstructures and nanostructures from x-ray absorption fine structures, x-ray excited optical luminescence, and theoretical studies. *The Journal of Physical Chemistry C*, 114(15):6966–6975.

[Mason et al., 2014] Mason, J. A., Veenstra, M., and Long, J. R. (2014). Evaluating metal-organic frameworks for natural gas storage. *Chem. Sci.*, 5:32–51.

[Mattsson et al., 2010] Mattsson, T. R., Lane, J. M. D., Cochrane, K. R., Desjarlais, M. P., Thompson, A. P., Pierce, F., and Grest, G. S. (2010). First-principles and classical molecular dynamics simulation of shocked polymers. *Phys. Rev. B*, 81:054103.

[Mayo et al., 1990] Mayo, S. L., Olafson, B. D., and Goddard, W. A. (1990). Dreiding: a generic force field for molecular simulations. *The Journal of Physical Chemistry*, 94(26):8897–8909.

[McCartney et al., 2010] McCartney, M. R., Agarwal, N., Chung, S., Cullen, D. A., Han, M.-G., He, K., Li, L., Wang, H., Zhou, L., and Smith, D. J. (2010). Quantitative phase imaging of nanoscale electrostatic and magnetic fields using off-axis electron holography. *Ultramicroscopy*, 110(5):375 – 382. Hannes Lichte 65th Birthday.

[McCartney and Smith, 2007] McCartney, M. R. and Smith, D. J. (2007). Electron holography: Phase imaging with nanometer resolution. *Annual Review of Materials Research*, 37(1):729–767.

[Mpourmpakis et al., 2007] Mpourmpakis, G., Tylianakis, E., and Froudakis, G. E. (2007). Carbon nanoscrolls: a promising material for hydrogen storage. *Nano Letters*, 7(7):1893–1897.

[Murthy et al., 1980] Murthy, C., Singer, K., Klein, M., and McDonald, I. (1980). Pairwise additive effective potentials for nitrogen. *Molecular Physics*, 41(6):1387–1399.

[Nakano, 1997] Nakano, A. (1997). Parallel multilevel preconditioned conjugate-gradient approach to variable-charge molecular dynamics. *Computer Physics Communications*, 104(1):59 – 69.

[Ortolani et al., 2011] Ortolani, L., Houdellier, F., Monthioux, M., Snoeck, E., and Morandi, V. (2011). Surface electrostatic potentials in carbon nanotubes and graphene membranes investigated with electron holography. *Carbon*, 49(4):1423 – 1429.

[Osakabe et al., 1986] Osakabe, N., Matsuda, T., Kawasaki, T., Endo, J., Tonomura, A., Yano, S., and Yamada, H. (1986). Experimental confirmation of aharonov-bohm effect using a toroidal magnetic field confined by a superconductor. *Phys. Rev. A*, 34:815–822.

[Pantatosaki et al., 2012] Pantatosaki, E., Megariotis, G., Pusch, A.-K., Chmelik, C., Stallmach, F., and Papadopoulos, G. K. (2012). On the impact of sorbent

mobility on the sorbed phase equilibria and dynamics: A study of methane and carbon dioxide within the zeolite imidazolate framework-8. *The Journal of Physical Chemistry C*, 116(1):201–207.

[Park et al., 2010] Park, S., Kittimanapun, K., Ahn, J. S., Kwon, Y.-K., and Tománek, D. (2010). Designing rigid carbon foams. *Journal of Physics: Condensed Matter*, 22(33):334220.

[Pedrielli et al., 2017a] Pedrielli, A., Taioli, S., Garberoglio, G., and Pugno, N. M. (2017a). Designing graphene based nanofoams with nonlinear auxetic and anisotropic mechanical properties under tension or compression. *Carbon*, 111:796 – 806.

[Pedrielli et al., 2017b] Pedrielli, A., Taioli, S., Garberoglio, G., and Pugno, N. M. (2017b). Gas adsorption and dynamics in pillared graphene frameworks. *Microporous and Mesoporous Materials*.

[Plimpton, 1995] Plimpton, S. (1995). Fast parallel algorithms for short-range molecular dynamics. *Journal of Computational Physics*, 117(1):1–19.

[Prakash et al., 2013] Prakash, M., Sakhavand, N., and Shahsavari, R. (2013). H2, n2, and ch4 gas adsorption in zeolitic imidazolate framework-95 and -100: Ab initio based grand canonical monte carlo simulations. *The Journal of Physical Chemistry C*, 117(46):24407–24416.

[Qin et al., 2017] Qin, Z., Jung, G. S., Kang, M. J., and Buehler, M. J. (2017). The mechanics and design of a lightweight three-dimensional graphene assembly. *Science Advances*, 3(1).

[Rappe et al., 1992] Rappe, A. K., Casewit, C. J., Colwell, K. S., Goddard, W. A., and Skiff, W. M. (1992). Uff, a full periodic table force field for molecular mechanics and molecular dynamics simulations. *Journal of the American Chemical Society*, 114(25):10024–10035.

[Rappé and Goddard, 1991] Rappé, A. K. and Goddard, W. A. (1991). Charge equilibration for molecular dynamics simulations. *The Journal of Physical Chemistry*, 95(8):3358–3363.

[Saldin and Spence, 1994] Saldin, D. and Spence, J. (1994). On the mean inner potential in high- and low-energy electron diffraction. *Ultramicroscopy*, 55(4):397–406.

[Schaedler et al., 2011] Schaedler, T. A., Jacobsen, A. J., Torrents, A., Sorensen, A. E., Lian, J., Greer, J. R., Valdevit, L., and Carter, W. B. (2011). Ultralight metallic microlattices. *Science*, 334(6058):962–965.

[Sellan et al., 2010] Sellan, D. P., Landry, E. S., Turney, J. E., McGaughey, A. J. H., and Amon, C. H. (2010). Size effects in molecular dynamics thermal conductivity predictions. *Phys. Rev. B*, 81:214305.

[Shenderova et al., 2000] Shenderova, O. A., Brenner, D. W., Omeltchenko, A., Su, X., and Yang, L. H. (2000). Atomistic modeling of the fracture of polycrystalline diamond. *Phys. Rev. B*, 61:3877–3888.

[Srinivas et al., 2011] Srinivas, G., Burress, J. W., Ford, J., and Yildirim, T. (2011). Porous graphene oxide frameworks: Synthesis and gas sorption properties. *J. Mater. Chem.*, 21:11323–11329.

[Stuart et al., 2000] Stuart, S. J., Tutein, A. B., and Harrison, J. A. (2000). A reactive potential for hydrocarbons with intermolecular interactions. *J. Chem. Phys.*, 112(14):6472.

[Stukowski, 2010] Stukowski, A. (2010). Visualization and analysis of atomistic simulation data with OVITO–the Open Visualization Tool. *Modelling and Simulation in Materials Science and Engineering*, 18(1):015012.

[Sumida et al., 2012] Sumida, K., Rogow, D. L., Mason, J. A., McDonald, T. M., Bloch, E. D., Herm, Z. R., Bae, T.-H., and Long, J. R. (2012). Carbon dioxide capture in metal–organic frameworks. *Chemical Reviews*, 112(2):724–781.

[Tagami et al., 2014] Tagami, M., Liang, Y., Naito, H., Kawazoe, Y., and Kotani, M. (2014). Negatively curved cubic carbon crystals with octahedral symmetry. *Carbon*, 76:266–274.

[Taioli et al., 2016] Taioli, S., Gabbrielli, R., Simonucci, S., Pugno, N. M., and Io-rio, A. (2016). Lobachevsky crystallography made real through carbon pseudo-spheres. *J. Phys.: Condens. Matter*, 28(13):13LT01.

[Tan and Gubbins, 1992] Tan, Z. and Gubbins, K. E. (1992). Selective adsorption of simple mixtures in slit pores: a model of methane-ethane mixtures in carbon. *The Journal of Physical Chemistry*, 96(2):845–854.

[Tang et al., 2013] Tang, Q., Zhou, Z., and Chen, Z. (2013). Graphene-related nanomaterials: tuning properties by functionalization. *Nanoscale*, 5:4541–4583.

[Tatti et al., 2016] Tatti, R., Aversa, L., Verucchi, R., Cavaliere, E., Garberoglio, G., Pugno, N. M., Speranza, G., and Taioli, S. (2016). Synthesis of single layer graphene on Cu(111) by C60 supersonic molecular beam epitaxy. *RSC Adv.*, 6(44):37982–37993.

[Tatti et al., 2017] Tatti, R., Timpel, M., Nardi, M. V., Fabbri, F., Rossi, R., Pasquardini, L., Chiasera, A., Aversa, L., Koshmak, K., Giglia, A., Pasquali, L., Rimoldi, T., Cristofolini, L., Attolini, G., Varas, S., Iannotta, S., Verucchi, R., and Salviati, G. (2017). Functionalization of sic/siox nanowires with a porphyrin derivative: a hybrid nanosystem for x-ray induced singlet oxygen generation. *Mol. Syst. Des. Eng.*, 2:165–172.

[Terrones and Mackay, 1993] Terrones, H. and Mackay, A. L. (1993). Triply periodic minimal surfaces decorated with curved graphite. *Chemical Physics Letters*, 207(1):45 – 50.

[Terrones et al., 1995] Terrones, H., Terrones, M., and Hsu, W. K. (1995). Beyond c60: graphite structures for the future. *Chem. Soc. Rev.*, 24(5):341.

[Thompson et al., 2009] Thompson, A. P., Plimpton, S. J., and Mattson, W. (2009). General formulation of pressure and stress tensor for arbitrary many-body interaction potentials under periodic boundary conditions. *J. Chem. Phys.*, 131(15):154107.

[Townsend et al., 1992] Townsend, S. J., Lenosky, T. J., Muller, D. A., Nichols, C. S., and Elser, V. (1992). Negatively curved graphitic sheet model of amorphous carbon. *Physical Review Letters*, 69(6):921–924.

[Trevisanutto et al., 2008] Trevisanutto, P. E., Giorgetti, C., Reining, L., Ladisa, M., and Olevano, V. (2008). Ab initio. *Phys. Rev. Lett.*, 101:226405.

[Tylianakis et al., 2011] Tylianakis, E., Dimitrakakis, G. K., Melchor, S., Dobado, J. A., and Froudakis, G. E. (2011). Porous nanotube network: a novel 3-D nanostructured material with enhanced hydrogen storage capacity. *Chem. Commun.*, 47(8):2303–2305.

[Valdevit et al., 2013] Valdevit, L., Godfrey, S. W., Schaedler, T. A., Jacobsen, A. J., and Carter, W. B. (2013). Compressive strength of hollow microlattices: Experimental characterization, modeling, and optimal design. *J. Mater. Res.*, 28(17):2461–2473.

[van Duin et al., 2001] van Duin, A. C. T., Dasgupta, S., Lorant, F., and Goddard, W. A. (2001). Reaxff: a reactive force field for hydrocarbons. *The Journal of Physical Chemistry A*, 105(41):9396–9409.

[Vörös et al., 2010] Vörös, M., Deak, P., Frauenheim, T., and Gali, A. (2010). The absorption spectrum of hydrogenated silicon carbide nanocrystals from ab initio calculations. *Applied Physics Letters*, 96(5):051909.

[Vörös et al., 2012] Vörös, M., Gali, A., Kaxiras, E., Frauenheim, T., and Knaup, J. M. (2012). Identification of defects at the interface between 3c-sic quantum dots and a sio2 embedding matrix. *Physica Status Solidi (b)*, 249(2):360–367.

[Wang et al., 2014] Wang, X., Sun, G., and Chen, P. (2014). Three-dimensional porous architectures of carbon nanotubes and graphene sheets for energy applications. *Frontiers in Energy Research*, 2(33).

[Willems et al., 2012] Willems, T. F., Rycroft, C. H., Kazi, M., Meza, J. C., and Haranczyk, M. (2012). Algorithms and tools for high-throughput geometry-based analysis of crystalline porous materials. *Microporous and Mesoporous Materials*, 149(1):134 – 141.

[Winkler et al., 2017] Winkler, F., Tavabi, A. H., Barthel, J., Duchamp, M., Yucelen, E., Borghardt, S., Kardynal, B. E., and Dunin-Borkowski, R. E. (2017). Quantitative measurement of mean inner potential and specimen thickness from

high-resolution off-axis electron holograms of ultra-thin layered wse2. *Ultramicroscopy*, 178:38 – 47. FEMMS 2015.

[Wu et al., 2013] Wu, J., He, J., and Zhang, Z. (2013). Fracture and negative Poisson's ratio of novel spanned-fullerenes nanotube networks under tension. *Computational Materials Science*, 80:15–26.

[Xiao et al., 2012] Xiao, X., Beechem, T. E., Brumbach, M. T., Lambert, T. N., Davis, D. J., Michael, J. R., Washburn, C. M., Wang, J., Brozik, S. M., Wheeler, D. R., Burckel, D. B., and Polsky, R. (2012). Lithographically defined three-dimensional graphene structures. *ACS Nano*, 6(4):3573–3579. PMID: 22404283.

[Yang and Zhong, 2006] Yang, Q. and Zhong, C. (2006). Molecular simulation of carbon dioxide/methane/hydrogen mixture adsorption in metal−organic frameworks. *The Journal of Physical Chemistry B*, 110(36):17776–17783. PMID: 16956262.

[Yin et al., 2013] Yin, J., Li, X., Zhou, J., and Guo, W. (2013). Ultralight three-dimensional boron nitride foam with ultralow permittivity and superelasticity. *Nano Lett.*, 13(7):3232–3236.

[Yoon et al., 2013] Yoon, J.-C., Lee, J.-S., Kim, S.-I., Kim, K.-H., and Jang, J.-H. (2013). Three-dimensional graphene nano-networks with high quality and mass production capability via precursor-assisted chemical vapor deposition. *Scientific Reports*, 3.

[Zhang et al., 2013] Zhang, L., Hu, Z., and Jiang, J. (2013). Sorption-induced structural transition of zeolitic imidazolate framework-8: A hybrid molecular simulation study. *Journal of the American Chemical Society*, 135(9):3722–3728.

[Zhang and Siepmann, 2006] Zhang, L. and Siepmann, J. I. (2006). Direct calculation of henry's law constants from gibbs ensemble monte carlo simulations: nitrogen, oxygen, carbon dioxide and methane in ethanol. *Theoretical Chemistry Accounts*, 115(5):391–397.

[Zhang et al., 2014] Zhang, L., Wu, G., and Jiang, J. (2014). Adsorption and diffusion of co2 and ch4 in zeolitic imidazolate framework-8: Effect of structural flexibility. *The Journal of Physical Chemistry C*, 118(17):8788–8794.

[Zhao et al., 2009] Zhao, H., Min, K., and Aluru, N. R. (2009). Size and chirality dependent elastic properties of graphene nanoribbons under uniaxial tension. *Nano Lett.*, 9(8):3012–3015.

Acknowledgement